REGULATION OF P GRANULE PHASE SEPARATION AND DYNAMICS

by
Jarrett V Smith

A dissertation submitted to The Johns Hopkins University in conformity with the requirements of the degree of Doctor of Philosophy

Baltimore MD
October 2017

Abstract

RNA granules are assemblies of RNA and RNA-binding proteins concentrated in cells without a surrounding membrane. Many RNA granules exhibit dynamic behavior *in vivo* and are able to go through cycles of controlled assembly and disassembly. In the worm *Caenorhabditis elegans* (*C. elegans*), a particular type of RNA granule known as a P granule goes through a series of temporally and spatially controlled disassembly and reassembly reactions resulting in proper localization to the germline.

Here we use P granules to study the mechanisms underlying these highly regulated dynamics. We provide evidence for a model in which MEX-5, an RNA binding protein, inhibits P granule assembly by binding to and sequestering available RNA from critical P granule components. We identify the intrinsically disordered domain containing protein MEG-3 as a critical component of P granules and provide evidence that the interaction between MEG-3 and RNA drives P granule assembly in the cell and that this interaction is antagonized by MEX-5.

We go on to show that the dynamic nature of these granules is, at least in part, due to active, energy-dependent disassembly. This work provides several key insights into the regulation of P granule dynamics that may prove to be generalizable for many types of RNA granules.

PhD Dissertation Referees for Jarrett Smith

Thesis Advisor: Geraldine Seydoux, PhD, Professor of Molecular Biology and Genetics, Johns Hopkins University School of Medicine

Thesis Reader: Andrew Holland, PhD, Professor of Molecular Biology and Genetics, Johns Hopkins University School of Medicine

Note to readers: In this text, all gene names and species names are italicized and all proteins are in capital letters in accordance with *C. elegans* conventions.

Preface

There are many people to whom I feel I owe my graduate school career. Foremost, Geraldine has proved to be an ideal mentor. The energy, attitude, and consistently high level of thought that she brings to the lab have been critical to my growth as a scientist. I joined the lab hoping to 'borrow' her way of thinking – a way of thinking that has lead to her successful career. I feel that I have been able to do that to some small, but invaluable degree. By creating a lab environment filled with phenomenal scientist Geraldine has given me the opportunity to be inspired by more than just her. Second to Geraldine, Jennifer Wang, my friend and rotation mentor was potentially the most influential presence on my graduate career. Jenn was incredibly supportive and allowed me to do what otherwise felt impossible. Outside of the lab I have felt constant support from both my program (BCMB) and my department (MBG). Thank you to Andrew Holland, Douglas Robinson, and Phillip Cole for serving on my thesis committee and offering helpful advice, both about scientific questions and about being successful in the word of science. In addition to my official mentors, I want to thank Peter Espenshade, Seth Margolis, and Rachel Green – faculty, who, despite not having any official tie to me (neither as thesis readers nor committee members), have helped me tremendously during my time here. Lastly, I want to thank my friends and family. My friends from the BCMB program - especially Mark Zbinden and Risa Burr – have been incredibly supportive, likely without realizing it. They have been my Baltimore family for the past 6 years. Lastly, my Family family, even with only a tenuous understanding of how I spend my time in lab, has provided me with their unflinching confidence in my endeavors at Hopkins and in life in general. Thank you all.

Table of Contents

List of Figures

Chapter 1

Chapter 2

Chapter A

Chapter B

Introduction

Cellular compartmentalization

It is not beneficial for every part of the cell to interact with every other part of the cell. Chemical reactions occurring in the mitochondria must be kept separate from the gradually acidifying environment of the lysosome and all of these must also be kept separate from the fragile contents of the nucleus. In order to keep all of these critical processes from interfering with each other, evolution has provided eukaryotic cells with membranes. These membranes not only hold the cell together, but inside the cell they allow separation between organelles contained in a common cytoplasm.

RNA granules and membraneless organelles

In addition to these many membrane-encompassed organelles, there is also a class of organelles that are not surrounded by a membrane. There are numerous organelles that fit into this category, the most well known of which is the nucleoli, a non-membrane bound space within the nucleus into which components important to ribosome biogenesis are concentrated. A less well-known class of non-membrane bound organelles are RNA granules. RNA granules are concentrated assemblies of RNA and RNA-binding proteins that form without a limiting membrane in the cytoplasm or nucleoplasm of cells (Courchaine, Lu et al. 2016). RNA granules are ubiquitous cellular structures and several classes of cytoplasmic RNA granules have been described, including stress granules, P bodies, neuronal granules and germ granules (Anderson and Kedersha 2006).

A fascinating aspect of RNA granules and indeed many membraneless organelles, is that by virtue of not being confined by a membrane, RNA granule components typically exchange rapidly between a highly concentrated pool in the granule and a more diffuse, less concentrated pool in the cytoplasm (Weber and Brangwynne 2012). When

considering the idea that membranes are used as a strategy to contain the contents and biochemistry inside to a defined location in the cell, and that these membraneless organelles constantly exchange with the surrounding cytoplasm, the most immediate question concerning RNA granules and other membraneless organelles is – what is the purpose of having an organelle that lacks a membrane? One class of RNA granules, called stress granules, form in response to various kinds of cellular stress including heat shock, osmotic shock, and nutrient deprivation and are thought to be involved in protecting the contents of the cell from the effects of harmful stressors (Kedersha, Gupta et al. 1999, Buchan, Yoon et al. 2011). Another class of RNA granules known as neuronal granules are thought to function in shuttling mRNAs down axons of neurons to be locally deposited and translated (Knowles, Sabry et al. 1996). A third class of RNA granules, referred to as germ granules are known to contain germline destined RNAs and associated proteins and are critical to properly localizing those contents to form functional germlines (Strome and Wood 1983). While these themes of sequestration and delivery are common functions of RNA granules, the question still remains – why not use a membrane? After all, membrane delimited organelles can be very effective at both sequestration and delivery of packaged materials.

Phase separation and RNA granule dynamics

Recently, more attention has been paid to the dynamic nature of membraneless organelles and RNA granules in particular. Because these organelles are able to quickly exchange with the cytoplasm and respond to environmental cues, RNA granule dynamics are very dependent on their environments. For example, stress granules assemble within seconds of exposure to toxic stimulants that require the temporary removal of mRNAs

from the translational pool (Anderson and Kedersha 2006). In eggs, germ granules assemble specifically in the germ plasm, a specialized area of the cytoplasm that is partitioned to the nascent germline during the first embryonic cleavages (Voronina, Seydoux et al. 2011). Although these structures have been recognized as effective cellular strategies to dynamically sequester and localize certain components, the molecular mechanisms dictating those dynamic behaviors are, in many cases, not well understood.

One insight into the mechanisms governing the dynamic behavior of RNA granules comes from the observation that many RNA granules behave in a way that is consistent with a liquid (Brangwynne, Eckmann et al. 2009, Li, Banjade et al. 2012, Hyman, Weber et al. 2014, Wang, Smith et al. 2014, Kroschwald, Maharana et al. 2015, Patel, Lee et al. 2015). Liquid-liquid phase separation (LLPS) refers the phenomenon of a pool of particles being able to passively transition from a soluble phase to a condensed phase and for those liquid-liquid phase separated compartments to maintain an equilibrium with the surrounding soluble pool (Brangwynne, Eckmann et al. 2009). Several dynamic behaviors of RNA granules can be explained using this LLPS framework, including their quick assembly and disassembly. As previously mentioned, RNA granules freely exchange with the surrounding cytoplasm at their interface. In addition to having exchange with the surrounding cytoplasm, the components of RNA granules also are known to quickly diffuse and exchange within the granule (Brangwynne, Eckmann et al. 2009, Buchan and Parker 2009, Jain, Wheeler et al. 2016). Both of these behaviors are expected for conventional liquids. Judging by fluorescence microscopy, most RNA granules have a roughly spherical shape, as would also be expected in a liquid due to surface tension and have been observed to fuse when coming

in contact with one another and then to relax back to a spherical shape as would also be expected of liquid droplets. (Brangwynne, Eckmann et al. 2009). Under this framework, the assembly and disassembly of these granules would be viewed as condensation and dissolution of the granule components. These would be passive processes driven by the local concentration of the constituent proteins. Indeed, many RNA granules form more readily when the local concentration of protein is high and disperse when the local concentration is lower (Anderson and Kedersha 2006, Brangwynne, Eckmann et al. 2009).

Considering this framework, several questions remain about how the dynamics of RNA granules are regulated by the cell. If LLPS occurs spontaneously as in the case of oil droplets forming in water, how does the cell keep such a tight temporal and spatial control over their formation? Is regulating the formation of RNA granules simply a matter of regulating the local concentration of their constituent proteins and RNAs? LLPS is hypothesized to occur due to transient low-affinity interactions constantly breaking and reforming between the constituent molecules resulting in fast internal molecular rearrangements (Decker, Teixeira et al. 2007, Reijns, Alexander et al. 2008, Brangwynne, Eckmann et al. 2009, Han, Kato et al. 2012, Kato, Han et al. 2012, Elbaum-Garfinkle, Kim et al. 2015, Nott, Petsalaki et al. 2015). Another proposed mechanism of regulating the formation of liquid-liquid phase separations is through post-translational modification of the residues responsible for those interactions (Wang, Smith et al. 2014). In addition to the question of how the cell regulates a liquid-liquid phase separated compartment is the question of whether all RNA granules fit within this framework or if LLPS explains only a subset of special cases. For example, it is unclear how the low-

affinity interactions thought to drive LLPS could result in specific recruitment of components to RNA granules. It has been suggested that more specific multivalent interactions among scaffolding proteins are essential for initial phase separation and less specific low-affinity interactions with those scaffolding molecules contribute to recruitment of non-essential client proteins (Banani, Rice et al. 2016). It is possible that the phase separation of essential scaffolding proteins does not fit within the LLPS framework.

Phase separation and human health

The study of this phenomenon and a greater understanding of the regulation of phase separation in cells have wide reaching implications in disease. In many neurological diseases such as ALS and Parkinson's, irreversible phase separation results from the misregulation of RNA granule dynamics (Patel, Lee et al. 2015, Rice and Rosen 2017). Uncovering the mechanisms that safely regulate the formation and disassembly of these phase separated compartments will be key in determining how to prevent the irreversible phase separation that is seen in these diseases.

C. elegans P granules as a model to study RNA granule regulation

Our lab focuses on using *C. elegans* germ granules to study RNA granule regulation. The germ (P) granules of *C. elegans* are an excellent model to study the mechanisms that regulate granule assembly (Updike and Strome 2010). For most of development, P granules are stable perinuclear structures, but in the transition from oocyte-to-embryo, P granules detach from the nucleus and become highly dynamic (Pitt, Schisa et al. 2000, Wang, Smith et al. 2014). As the oocyte is ovulated in the spermatheca, P granules disassemble and release their components in the cytoplasm.

After fertilization, P granule proteins reassemble into dynamic granules that undergo repeated cycles of assembly and disassembly in synchrony with cell division. Live imaging in the 1-cell zygote has revealed that these cycles are spatially patterned along the anterior-posterior axis of the embryo: granule assembly is favored in the posterior and granule disassembly is favored in the anterior (Brangwynne, Eckmann et al. 2009, Gallo, Wang et al. 2010). By the first mitosis, P granules are found exclusively in the posterior cytoplasm together with other germ plasm components. As a result, P granules are segregated to the posterior germline blastomere P_1 and excluded from the anterior somatic blastomere AB.

Because P granules are known to rapidly disassemble only on the anterior side of the cell and reassemble on the posterior side at a very stereotypical time in the cell cycle, they are an excellent subject to study in order to understand how the cell tightly regulates RNA granule formation and disassembly temporally and spatially. Here we attempt to determine both the critical regulators of P granule dynamics in the early *C. elegans* embryo and to understand mechanism by which those players regulate granule dynamics.

P granule asymmetry is under the control of the PAR polarity network which divides the zygote into distinct anterior and posterior domains (Motegi and Seydoux 2013). The PAR-1 kinase is enriched in the posterior cytoplasm and restricts the RNA-binding protein MEX-5 (and its redundant homolog MEX-6) to the anterior cytoplasm (Griffin, Odde et al. 2011). MEX-5 and MEX-6 in turn restrict P granules to the posterior (Schubert, Lin et al. 2000, Gallo, Wang et al. 2010). In *mex-5 mex-6* double mutants, P granule still undergo cycles of assembly and disassembly but these are no longer patterned along the anterior-posterior axis, and small granules remain throughout the

cytoplasm (Gallo, Wang et al. 2010). An attractive hypothesis is that MEX-5 blocks phase separation of P granule components in the anterior cytoplasm (Brangwynne, Eckmann et al. 2009, Lee, Brangwynne et al. 2013). The mechanism of MEX-5 action and the critical P granule component(s) regulated by MEX-5, however, are not known.

P granule assembly in zygotes requires several P granule proteins, including the RNA-binding protein PGL-1 (and its redundant paralog PGL-3). PGL-1 and PGL-3 are RGG domain proteins that self-associate and recruit other RNA-binding proteins to the granules, including the GLH family of RNA helicases (Updike and Strome 2010, Hanazawa, Yonetani et al. 2011). In addition to RNA-binding domains, proteins in RNA granules often contain prion-like, low complexity, or intrinsically-disordered regions (IDRs) (Courchaine, Lu et al. 2016). P granules contain the intrinsically-disordered protein MEG-3 (and its redundant paralog MEG-4) (Hanazawa, Yonetani et al. 2011, Wang, Smith et al. 2014). MEG-3 and MEG-4 are redundant, serine-rich proteins that bind to PGL-1 *in vitro* and are essential for P granule assembly in embryos. In zygotes lacking *meg-3* and *meg-4*, PGL-1 and GLH-2 form transient assemblies that do not segregate asymmetrically and are not maintained in later stages (Wang, Smith et al. 2014). Phosphorylation of MEG-3 by the DYRK kinase MBK-2 promotes granule disassembly in zygotes, but the mechanism that favors disassembly in the anterior cytoplasm is not known (Wang, Smith et al. 2014).

In addition to understanding the players regulating P granule dynamics, we also attempt to determine whether P granules behave entirely as liquids. P granules, like all RNA granules, have multiple components, and previous work suggests that those components are not homogenously distributed throughout the granule (Wang, Smith et al.

2014). This non-homogenous mixing seems inconsistent with a model in which all components of a P granule undergo LLPS. Furthermore, while IDRs such as those found in MEG-3 spontaneously de-mix from the aqueous solvent to form liquid droplets, they have also been shown to form non-liquid hydrogels (Li, Banjade et al. 2012, Weber and Brangwynne 2012, Elbaum-Garfinkle, Kim et al. 2015, Guo and Shorter 2015, Lin, Protter et al. 2015, Nott, Petsalaki et al. 2015). Like RNA granules *in vivo*, proteins in both LLPS droplets and hydrogels exchange with the solvent (Kato, Han et al. 2012, Li, Banjade et al. 2012, Elbaum-Garfinkle, Kim et al. 2015, Lin, Protter et al. 2015). These findings have suggested that both LLPS and reversible gelation may drive the assembly and dynamics of RNA granules *in vivo* (Guo and Shorter 2015). Lastly, a subset of stress granule proteins have been identified as being incorporated into stable stress granule cores that do not exhibit the same liquid behaviors as the overall stress granule (Jain et al 2016). While the function or relevance of these stress granule cores is unclear, all of these points illustrate the possibility that RNA granules, which are composed of multiple components, may also be composed of multiple phases.

Thesis Aims

My work in Geraldine Seydoux's lab is focused on the following aims regarding the regulation of P granule disassembly:

1. Determining the mechanism by which MEX-5 is required for asymmetric P granule disassembly in the early zygote.
2. Determine which, if any, components of P granules are the critical targets of P granule regulators.

3. Determine the nature of P granule phase separation. More specifically, whether the different components of P granules differ in their phase or whether all can be explained inside of the LLPS framework.

Chapter 1

Spatial patterning of P granules by RNA-induced phase separation of the intrinsically-disordered protein MEG-3

This chapter is an edited version of the manuscript "Spatial patterning of P granules by RNA-induced phase separation of the intrinsically-disordered protein MEG-3" by J smith, D Calidas, H Schmidt, T Lu, D Rasoloson, and G Seydoux published in eLife volume 5 :e21337 DOI: 10.7554/eLife.213377.

1.1 Summary

RNA granules are non-membrane bound cellular compartments that contain RNA and RNA binding proteins. The molecular mechanisms that regulate the spatial distribution of RNA granules in cells are poorly understood. During polarization of the *C. elegans* zygote, germline RNA granules, called P granules, assemble preferentially in the posterior cytoplasm. In this study we present evidence that P granule asymmetry depends on RNA-induced phase separation of the granule scaffold MEG-3. MEG-3 is an intrinsically disordered protein that binds and phase separates with RNA *in vitro*. We show that *in vivo*, MEG-3, but not PGL-1/3, are essential for granule asymmetry, and that the RNA binding protein MEX-5 localizes MEG-3 in a posterior-rich gradient. MEX-5 is necessary and sufficient to suppress MEG-3 granule formation *in vivo*, and suppresses RNA-induced MEG-3 phase separation *in vitro*. Our findings suggest that MEX-5 interferes with MEG-3's access to RNA, thus locally suppressing MEG-3 phase separation to drive P granule asymmetry. Regulated access to RNA, combined with RNA-induced phase separation of key scaffolding proteins, may be a general mechanism for controlling the formation of RNA granules in space and time.

1.2 Results

Hierarchical regulation of P granule assembly

To determine the genetic hierarchy that controls granule asymmetry, we first compared the distributions of MEX-5, MEG-3, PGL-1 and GLH-1 during the earliest stages of zygote polarization. We monitored MEX-5, MEG-3 and GLH-1 localization using tagged alleles generated by genome editing (Methods, Table S1) and PGL-1 localization using a polyclonal antibody that recognizes PGL-1 (Strome and Wood 1983).

Before polarization, MEX-5, MEG-3, PGL-1 and GLH-1 were all distributed evenly throughout the cytoplasm. MEX-5 appeared mostly diffuse in the cytoplasm with a few foci, whereas MEG-3, PGL-1, and GLH-1 appeared both diffuse and enriched in many small (<1 micron diameter) foci (Figure 1A). During polarization (pronuclear formation and migration), MEX-5 and MEG-3 began to redistribute into opposing cytoplasmic gradients along the long axis of the zygote (anterior-posterior axis) with MEG-3 beginning to form large (~1 micron) granules in the posterior (Figure 1A). Total levels of MEG-3 do not change during this period, consistent with redistribution of existing MEG-3 protein from anterior to posterior (Figure 1B, Figure S1). In contrast to MEX-5 and MEG-3, PGL-1 and GLH-1 remained uniformly distributed during polarization. After polarization (mitosis), all proteins were localized, with MEX-5 in the anterior cytoplasm and MEG-3, PGL-1 and GLH-1 in large granules in the posterior cytoplasm (Figure 1A).

To determine the interdependence of these localizations, we examined the effect of removing MEX-5/6, MEG-3/4 or PGL-1/3 using RNA-mediated interference (RNAi) or genetic mutants (GLH-1 has already been shown to depend on PGL-1/3 for asymmetry (Hanazawa, Yonetani et al. 2011)). In zygotes derived from mothers treated with double-stranded RNA against *mex-5* and *mex-6* (*mex-5/6(RNAi)* zygotes), the MEG-3 gradient did not form and MEG-3 and PGL-1 granules remained uniformly distributed throughout the cytoplasm (Figure 1C, (Gallo, Wang et al. 2010). In *meg-3; meg-4* double mutant embryos, the MEX-5 gradient was unaffected but neither PGL-1 nor PGL-3 granules segregated properly (Wang, Smith et al. 2014, Figure 1C, Figure S1). In *pgl-1(RNAi); pgl-3(bn104)* zygotes, the MEG-3 and MEG-4 gradients were unaffected and MEG-

3/MEG-4 granules formed in the posterior as in wild-type, except that the granules appeared smaller especially in zygotes (Wang, Smith et al. 2014). These analyses suggest that MEX-5 and MEX-6 regulate granule asymmetry by localizing MEG-3 and MEG-4 to the posterior, which in turn are required to localize PGL-1 and PGL-3. PGL-1 and PGL-3 are not required to localize MEG-3 or MEG-4, but contribute to the size of MEG-3/4 granules as reported previously (Wang, Smith et al. 2014).

MEX-5 is necessary and sufficient to suppress MEG-3 granule formation

Using *mex-5* transgenes, Griffin *et al.* 2011 showed that formation of the MEX-5 gradient requires phosphorylation of serine 404 in the C-terminus of MEX-5 by the kinase PAR-1. To determine whether the MEX-5 gradient is required to pattern MEG-3, we mutated serine 404 to alanine (S404A) at the *mex-5* locus using CRISPR/Cas9-mediated genome editing (Paix, Folkmann et al. 2015). We introduced the S404A mutation in two strains: one where the *mex-5* locus had been previously tagged with mCherry to monitor MEX-5 localization, and one where MEG-3 had been previously tagged with GFP to monitor MEG-3 localization (Table S1). As expected, we found that MEX-5(S404A) failed to form a gradient during zygote polarization and remained uniformly distributed (Figure 2A). Using the MEG-3::GFP strain, we found that zygotes derived from mothers homozygous for *mex-5(s404a)* (*mex-5(S404A)* zygotes), MEG-3 did not form a gradient or granules. Instead, MEG-3 remained uniformly distributed in the cytoplasm throughout the 1-cell stage (Figure 2B). We conclude that MEX-5 is sufficient to suppress the formation of MEG-3 granules throughout the cytoplasm.

MEX-5 RNA binding is required to suppress MEG-3 granule assembly

The MEX-5 RNA-binding domain is comprised of two zinc fingers that bind with high affinity to poly-U stretches. Pagano *et al.* 2007 have shown that mutation of a single amino acid in each finger (R247E and K318E) reduces MEX-5 binding affinity for poly-U by 35-fold. Using *mex-5* transgenes, Griffin et al., 2011 showed the finger mutations R247E and K318E also disrupt formation of the MEX-5 gradient *in vivo*. To determine the effect of these mutations on MEG granule assembly, we introduced R247E and K318E (hereafter referred to as ZF-) at the *mex-5* locus by CRISPR/Cas9 genome editing into an OLLAS::MEX-5 tagged line and the MEG-3::GFP line. Like MEX-5(S404A), MEX-5(ZF-) did not form a gradient and was uniformly distributed in zygotes (Figure 2A). In contrast to *mex-5(S404A)* zygotes, however, *mex-5(ZF-)* zygotes assembled posterior MEG-3 granules as in wild-type (data not shown). *mex-5* is partially redundant with its paralog, *mex-6* (Schubert, Lin et al. 2000), which is sufficient to polarize MEG granules in the absence of MEX-5 (Figure S2). Consistent with this redundancy, we found that depletion of *mex-6 by RNAi* in *mex-5(ZF-)* zygotes caused MEG-3 granules to assemble throughout the cytoplasm, as in *mex-5/6(RNAi)* zygotes (Figure 2B). These observations suggest that *mex-5(ZF-)* is a loss-of-function allele. The loss of *mex-5* activity was not due to reduced expression as MEX-5(ZF-) was expressed at the same level as wild-type MEX-5 (Figure S2).

To determine whether high-affinity RNA binding is also required for MEX-5(S404A) ability to suppress MEG-3::GFP granule assembly throughout the cytoplasm, we introduced the S404A mutation by genome editing into *mex-5(ZF-)* hermaphrodites. We found that *mex-5(ZF-,S404A)* zygotes assembled posterior MEG-3::GFP granules, as

is observed in *mex-5(ZF-)* and wild-type zygotes. Depletion of *mex-6* by RNAi in this background yielded zygotes with uniform MEG-3::GFP granules, as expected for a *mex-5/6* loss-of-function phenotype (Figure 2B). We conclude that suppression of MEG-3 granule assembly by MEX-5 depends on MEX-5's ability to bind RNA with high affinity.

MEG-3 binds RNA *in vitro*

Unlike MEX-5, MEG-3 does not have a recognizable RNA-binding domain. MEG-3 contains a long predicted intrinsically-disordered region (IDR) at its N-terminus (aa1-550) followed region with lower predicted disorder (aa550-862) [IUPRED predictions, (Dosztanyi, Csizmok et al. 2005)]. To determine whether MEG-3 binds RNA, we expressed and purified as His-tagged fusions full length MEG-3, MEG-3(aa1-544) (hereafter referred to MEG-3_{IDR}) and MEG-3(aa545-862) (hereafter referred to MEG-3_{Cterm}) (Figure S3). We tested each for binding to poly-U30 RNA using electrophoretic mobility shift assays (EMSA) and fluorescent polarization (FP) assays (Pagano, Farley et al. 2007). EMSA experiments revealed that MEG-3 and MEG-3_{IDR} interact with poly-U30 RNA to form complexes that migrate as a discrete band during electrophoresis (Figure 3A). Using FP, we calculated the apparent dissociation constant ($K_{d,app}$) of MEG-3 for poly-U30 to be ~32 nM, similar to that of MEX-5 ($K_{d,app}$ = ~29 nM) (Pagano, Farley et al. 2007). MEG-3_{IDR} also bound RNA but with ~15-fold lower affinity ($K_{d,app}$ = ~460nM). MEG-3_{Cterm} did not bind RNA significantly by EMSA or in the FP assay ($K_{d,app}$ > 3000 nM) (Figure 3A, Figure S3). We conclude that MEG-3 binds

RNA with high affinity and that this activity resides primarily within the MEG-3 IDR, although high affinity binding also requires the MEG-3 C-terminus.

To begin to explore the specificity of MEG-3 RNA binding, we challenged MEG-3/poly-U30 complexes with increasing concentrations of competitor RNAs and examined their behavior by EMSA. We found that poly-U, and to a lesser extent poly-A, were effective competitors, but not poly-C or poly-G (Figure S3). These observations suggest that MEG-3's affinity for RNA is affected by nucleotide composition.

MEG-3 and MEG-3$_{IDR}$ phase separate *in vitro*

Concentrated (<1 μM) solutions of RNA-binding proteins containing IDRs spontaneously phase separate when switched from high to low salt (150 mM NaCl) (Elbaum-Garfinkle, Kim et al. 2015, Lin, Protter et al. 2015, Nott, Petsalaki et al. 2015). We were not able to maintain high concentrations of MEG-3 or MEG-3$_{IDR}$ in solution in the presence of high salt (Methods). Therefore to examine the phase separation properties of MEG-3, we used concentrated (100-320 μM) preparations maintained in 6M urea, diluted these into aqueous buffer (150 mM NaCl) and used light microscopy to immediately observe the mixture (Method). We found that MEG-3 and MEG-3$_{IDR}$ readily formed phase-separated condensates within 10 min at room temperature. Control proteins (BSA and MBP) subjected to the same treatment did not phase separate (data not shown). MEG-3 condensates were observed across a range of protein concentrations (0.5 μM to 5 μM) and became larger and more abundant with increasing protein concentration (Figure S4). MEG-3 and MEG-3$_{IDR}$ behaved similarly to each other, except that in the low concentration range (< 5 μM), MEG-3 formed more condensates than MEG-3$_{IDR}$, and in

the high concentration range (> 5 μM) MEG-3_{IDR} tended to form larger condensates (Figure S4).

RNA can stimulate the phase transition of IDR proteins that bind RNA (Guo and Shorter 2015). To determine the effect of RNA on MEG-3 phase separation, we added poly-U30 RNA to the phase separation buffer before diluting in MEG-3. We found that 0.1 μM poly-U30 was sufficient to increase the number of visible condensates especially at low MEG-3 protein concentrations (<1 μM) (Figure 4A, Figure S4). Higher concentrations of RNA increased the number of MEG-3 condensates even further. For a given concentration of poly-U30, MEG-3 formed more condensates than MEG-3_{IDR} (Figure 4A, Figure S4). Addition of sub-stochiometric amounts of fluorescently tagged poly-U30 confirmed that the RNA phase separates with MEG-3 (Figure S4). We conclude that MEG-3 and MEG-3_{IDR} have an intrinsic propensity to phase separate that can be stimulated by RNA.

MEX-5 inhibits RNA-induced phase separation

To examine whether MEX-5 can affect MEG-3 phase separation, we purified the MEX-5 RNA-binding domain and C-terminus (aa236-468) as a His fusion (we were not able to obtain soluble full length MEX-5, Methods). We pre-incubated recombinant MEX-5 with poly-U in buffer for 30 minutes before adding MEG-3. We found that MEX-5 strongly inhibited MEG-3 phase separation induced by RNA. Addition of excess RNA (3-fold increase) restored robust phase separation in the presence of MEX-5 (Figure 4B, Figure 4C). Additionally, MEX-5 had no effect on the phase separation of MEG-3 in the absence of RNA (Figure S4). These observations suggest that MEX-5 does not

interfere with MEG-3 phase separation directly, but interferes with the ability of poly-U30 to induce phase separation.

MEG-3_{IDR} forms a MEX-5-dependent gradient *in vivo* and can be stimulated to form granules by excess RNA.

Our *in vitro* experiments indicate that MEG-3_{IDR} is sufficient to promote RNA binding and phase separation, but does so less efficiently than full length MEG-3 at low protein concentrations. To examine the behavior of MEG-3_{IDR} *in vivo*, we deleted the C-terminus of MEG-3 by CRISPR/Cas9 genome editing to generate a *meg-3* allele that only expresses MEG-3_{IDR} (Methods, Table S1). We found that, like full-length MEG-3, MEG-3_{IDR} is a cytoplasmic protein that redistributes into a posterior-rich gradient during polarization of the zygote (Figure 5A). Unlike MEG-3, however, MEG-3_{IDR} did not coalesce into prominent, micron-sized granules in zygotes (Figure 5A). Distinct MEG-3_{IDR} granules were observed starting in the 2-cell stage as MEG-3_{IDR} segregates into the progressively smaller P blastomeres (Figure 5A). In *mex-5/6(RNAi)* zygotes, MEG-3_{IDR} did not form a gradient and did not form granules (Figure 5B). These observations indicate that MEG-3_{IDR} is partially defective in granule formation, while remaining sensitive to MEX-5/6. The loss of *meg-3* activity was not a result of reduced expression as MEG-3_{IDR} was expressed at greater levels than wild-type MEG-3 (Figure S5).

In vitro, the weaker phase separation properties of MEG-3_{IDR} at low protein concentrations can be stimulated by RNA. To determine whether excess RNA could also rescue granule formation by MEG-3_{IDR} in zygotes, we blocked maternal mRNA turnover by depleting LET-711 by RNAi. LET-711 is the scaffolding component of the

CCF/NOT1 deadenylase, the main deadenylase that promotes mRNA turnover in oocytes and early embryos (DeBella, Hayashi et al. 2006, Nousch, Techritz et al. 2013). Depletion of LET-711 has been shown to increases poly-adenylation and to block the turnover of maternal *nos-2* RNA in early embryos (Gallo, Munro et al. 2008, Nousch, Techritz et al. 2013). We found that MEG-3_{IDR} formed numerous micron-sized granules in *let-711(RNAi)* zygotes. The MEG-3_{IDR} granules and cytoplasmic gradient extended further towards the anterior compared to wild-type (Figure 5B). These observations suggest that, as we observed *in vitro*, excess RNA can overcome the inhibitory effects of MEX-5 and boost MEG-3 coalescence *in vivo*.

1.3 Discussion

P granule asymmetry in *C. elegans* zygotes is a text-book example of cytoplasmic partitioning (Strome and Wood 1983). In this study, we present evidence that P granule asymmetry is a direct consequence of an asymmetry in the distribution of the P granule scaffold MEG-3. MEG-3 localizes in a posterior-rich gradient under the control of the RNA-binding protein MEX-5, which localizes in a mirror-image, anterior-rich gradient. Our findings suggest that the MEG-3 gradient arises from an anterior-posterior gradient in RNA availability created by MEX-5. MEX-5 interferes with MEG-3 access to RNA in the anterior, which promotes MEG-3 phase separation in the posterior where MEX-5 concentration is low.

MEG-3 is an RNA-binding protein that is stimulated by RNA to phase separate

MEG-3 contains a long N-terminal IDR but no recognizable RNA-binding domain. We have found that MEG-3 binds RNA (poly-U30) with nanomolar affinity *in vitro* ($K_{d,app}$ = 32 nm). The MEG-3_{IDR} is essential for binding, but on its own binds with lower affinity ($K_{d,app}$ = 460 nm). One possibility is that the MEG-3 IDR extends beyond the region predicted by IUPRED (Dosztanyi, Csizmok et al. 2005). The region immediately C-terminal scores close to the IUPRED cut-off (Wang, Smith et al. 2014), and may contribute to RNA binding. IDRs are over-represented among RNA-binding domains (Varadi, Zsolyomi et al. 2015, Castello, Fischer et al. 2016). Electrostatic interactions between positively-charged amino acids and the negatively-charged RNA backbone are often invoked as a possible mechanism for RNA binding by IDRs (Guo and Shorter 2015, Basu and Bahadur 2016). MEG-3 is rich in basic residues, but shows a strong preference for poly-U over poly-C and poly-G, suggesting that non-charged interactions are also involved.

Several recent studies have demonstrated that RNA-binding proteins containing IDRs phase separate in aqueous solutions (Guo and Shorter 2015). MEG-3 follows this paradigm: MEG-3 readily formed condensates within minutes of dilution from urea to an aqueous buffer (150mM NaCl). MEG-3 phase separation could be stimulated by RNA: addition of poly-U30 to the phase separation buffer increased the number of MEG-3 condensates especially at 1μM and lower protein concentrations. MEG-3_{IDR} behaved similarly to full-length MEG-3, except that MEG-3_{IDR} required higher concentrations of RNA to phase separate at low protein concentrations. Consistent with this *in vitro* behavior, MEG-3_{IDR} did not form large granules in wild-type zygotes, but could be

induced to do so by blocking mRNA deadenylation and turnover (RNAi depletion of the LET-711/NOT1). These observations suggest that the IDR confers on MEG-3 an intrinsic tendency for phase separation that is tunable by RNA. RNA-induced phase separation has also been observed for Whi3, a fungal RNA-binding protein, and for hnRNPA1, a stress granule protein (Lin, Protter et al. 2015, Zhang, Elbaum-Garfinkle et al. 2015). In these proteins, the IDR and RNA-binding domain are distinct and RNA-induced phase separation requires both domains. It will be interesting to determine whether the MEG-3_{IDR} in fact contains separable domains for phase separation and RNA binding.

MEX-5 patterns MEG-3 by limiting access to RNA

MEX-5 has been hypothesized to regulate P granule asymmetry by creating a supersaturation gradient of critical granule component(s) along the anterior-posterior axis of the zygote (Lee, Brangwynne et al. 2013). Our observations suggest that the critical component regulated by MEX-5 is RNA. MEX-5 binds RNA with nanomolar affinity ($K_{d,app}$ = ~29 nM, Pagano et al. 2007) and is 10-fold more abundant than MEG-3 in embryos (Figure S2). In our *in vitro* phase separation assay, the MEX-5 RNA-binding domain was sufficient to inhibit RNA-induced phase separation of MEG-3. Similarly, *in vivo*, uniform MEX-5 was sufficient to inhibit MEG-3 granule assembly throughout the cytoplasm and this activity was disrupted by mutations that lower MEX-5's affinity for RNA. Together, these results support a model where MEX-5 suppresses MEG-3 phase separation by limiting MEG-3's access to RNA. How MEX-5 regulates MEG-3's access to RNA *in vivo* remains to be determined. As suggested by the *in vitro* observations, MEX-5 could compete directly with MEG-3 for RNA binding. Alternatively, MEX-5

could function indirectly by recruiting factors to MEG-3/RNA complexes that reduce MEG-3's affinity for RNA. The MEX-5 gradient arises as a consequence of phosphorylation by the posteriorly-enriched kinase PAR-1, which decreases the size of MEX-5 complexes and increases MEX-5's diffusion rate (Griffin, Odde et al. 2011). One possibility is that phosphorylation by PAR-1 prevents MEX-5 from binding RNA creating a pool of "MEX-5-free" RNA available to phase separate with MEG-3 in the posterior cytoplasm.

MEX-5's high affinity for poly-U stretches, which are present in 91% of *C. elegans* 3' UTRs (Pagano, Farley et al. 2007), suggests that MEX-5 interacts with most mRNAs in zygotes and thus could function as a general "mRNA sink". Consistent with this view, the MEX-5 gradient patterns the distribution of three other RNA-binding proteins that, like MEG-3, form posterior-rich gradients (Wu, Zhang et al. 2015). The observation that blocking mRNA turnover stimulates MEG-3 coalescence into macroscopic granules is consistent with the idea that the mRNA pool accessible to MEG-3 is limiting in zygotes. A limiting mRNA pool has also been suggested to regulate the balance of P bodies and stress granules in cells (Buchan and Parker 2009). We propose that regulated access to mRNAs, combined with RNA-induced phase separation of key scaffolding proteins, may be a general mechanism for controlling the formation of RNA granules in space and time.

MEG-3 and MEG-4 scaffold P granules in zygotes

A recent theoretical study has suggested that MEX-5 patterns P granules by regulating the phase separation of a different P granule protein: PGL-3 (Saha, Weber et al. 2016). This model is based on three *in vitro* observations: 1) PGL-3 binds RNA using a C-terminal RGG domain, 2) RNA-binding via the RGG domain stimulates phase separation of PGL-3 and 3) MEX-5 can interfere with the formation of PGL-3/RNA condensates. Using estimates for the *in vivo* concentrations and diffusion rates of PGL-3, MEX-5 and RNA, Saha et al. built a mathematical model that simulates a competition for RNA between MEX-5 and PGL-3. In the simulation, introduction of the MEX-5 gradient is sufficient to dissolve PGL-3 granules in the anterior cytoplasm. This model, however, is inconsistent with *in vivo* observations. First, Hanazawa et al (2011) have reported that PGL-3 lacking the RGG domain still assembles asymmetric granules in zygotes. Second, in zygotes lacking MEG-3 and MEG-4, PGL-3 does not become polarized in zygotes despite the presence of the MEX-5 gradient (Figure S1). These findings indicate that, contrary to the model proposed by Saha et al. (2016), PGL-3 does not require RNA binding to assemble granules or become asymmetric and does not sense the MEX-5 gradient directly. Our data suggest instead that PGL-3 is recruited to the posterior by the MEGs. PGL-3 binds PGL-1 and PGL-1 binds MEG-3 (Hanazawa, Yonetani et al. 2011, Wang, Smith et al. 2014), raising the possibility that the PGLs are recruited to MEG assemblies by direct protein-protein interactions. We showed previously that MEG-3 overlaps but does not co-localize perfectly with PGL-3 in P granules (Wang, Smith et al. 2014). Formation of stable PGL assemblies in embryos also requires LAF-1, a DEAD-box RNA helicase that phase separates independently of RNA (Elbaum-Garfinkle, Kim et

al. 2015). P granules therefore appear to comprise multiple phases, each with distinct properties and components that have affinity for one another but do not fully mix. We suggest that MEG-3 and MEG-4 form the main RNA-dependent phase of P granules. During polarization, in response to the PAR-1-induced MEX-5 gradient, the MEGs concentrate preferentially in the posterior cytoplasm where they recruit other P granule components to build multi-phasic assemblies.

1.4 Experimental Procedures

CRISPR genome editing - *C. elegans* was cultured according to standard methods at 20^{o}C (Brenner 1974). Genome editing was performed using CRISPR/Cas9 as described in Paix et al., 2015. Alleles used in this study are listed in Supplemental file 1.

RNA mediated Interference (RNAi) - RNAi knock-down experiments were performed by feeding on HT115 bacteria (Timmons and Fire 1998). Feeding constructs were obtained from the Ahringer or Openbiosystems libraries and transformed into HT115 bacteria. pL4440 was used as a negative control empty feeding vector. Bacteria were grown at 37°C in LB + ampicillin (100 µg/mL) for 5 hours, induced with 5 mM IPTG for 45 minutes, plated on NNGM (nematode nutritional growth media) + ampicillin (100 µg/mL) + IPTG (1 mM), and grown overnight at room temperature. Embryos isolated by bleaching from gravid hermaphrodites were added to the RNAi plates and transferred to fresh plates as L4 larvae before examination of their progeny. All RNAi experiments were performed at 20^{o}C.

Protein Expression and Purification - All purifications were performed using an AKTA pure FPLC protein purification system (GE Healthcare).

Purification of MEG-3 and MEG-3$_{IDR}$: MEG-3 (aa1-862), MEG-3$_{\text{IDR}}$ (aa1-544) fused to an N-terminal 6XHis tag in pET28a were expressed in Rosetta (DE3) cells at 16°C in LB + ampicillin (100 µg/mL) to an OD600 of ~0.4 and induced with 0.4 mM isopropyl β-D-1-thiogalactopyranoside at 16° C for 16 hours. Cells were resuspended in Buffer A (20 mM HEPES, 500 mM NaCl, 20 mM Imidazole, 10% (vol/vol) glycerol, 1% Triton-X100, 6M Urea, 6 mM βME, pH7.4) with added protease inhibitors and TCEP, lysed by sonication, spun at 13,000 rpm for 25 minutes, and incubated overnight

at 4C. Lysate was passed over a His Prep FF 16/10 column (GE Healthcare). Bound protein was washed with Buffer B (20 mM HEPES, pH 7.4, 1M NaCl, 25 mM Imidazole, 10% (vol/vol) glycerol, 6M urea, 6 mM βME) and eluted in Buffer C (20 mM HEPES, pH 7.4, 1M NaCl, 250 mM Imidazole, 10% (vol/vol) Glycerol, 6M Urea, 6 mM βME). After each purification, aliquots of the peak elution fraction were run on 4-12% Bis Tris gels, and stained with Simply Blue Safe Stain (ThermoFisher). Proteins were concentrated to a final concentration of 100-320 μM in elution Buffer C. For use in RNA binding assays, proteins were dialyzed into storage buffer B (25 mM Hepes, pH 7.4, 1M NaCl, 6 mM βME, 10% (vol/vol) glycerol) and stored at -80° C.

Purification of MEG-3$_{Cterm}$: MEG-3(545-862) was purified as above and also natively using the same protocol without urea. MEG-3$_{Cterm}$ purified under native conditions was soluble in aqueous buffer even at high concentrations (>1uM) and was used for RNA-binding assays.

Dialysis of MEG-3: MEG-3 that was utilized in RNA binding experiments was step dialyzed out of urea, into 4.5M Urea, 3M Urea, 1.5M Urea, and 0M Urea in MEG-3 Storage Buffer (25mM HEPES, pH 7.4, 1M NaCl, 6 mM βME, 10% Glycerol). The protein was aliquoted and flash frozen in MEG-3 Storage Buffer and stored at -80C.

Purification of MEX-5: MEX-5(aa236-468) was purified as an N-terminal 6xHis:MBP fusion expressed in Rosetta (DE3) competent cells. Cells were grown at 37° C in LB + ampicillin (100μg/mL) to an OD600 of ~0.4, before induction with 0.2 mM isopropyl β-D-1-thiogalactopyranoside and 100 μM zinc acetate at 16° C for 16 hours. Cells were resuspended in lysis buffer (20 mM Tris-HCl, pH 8.3, 200 mM NaCl, 20 mM imidazole, 10% (vol/vol) glycerol, 1 mM TCEP, 100 μM zinc acetate, Roche complete

EDTA-free protease inhibitor tablet), lysed by sonication and pelleted at 10,000 rcf for 15 minutes. The supernatant was passed over a HisTrap HP column (GE Healthcare) and washed with wash buffer (20 mM Tris-HCl, pH8.3, 800 mM NaCl, 20 mM imidazole, 10% (vol/vol) glycerol, 100 μM zinc acetate,1 mM TCEP). Column was eluted using elution buffer (20 mM HEPES, pH 8.3, 500 mM NaCl, 250 mM imidazole, 10% (vol/vol) glycerol, 100 μM zinc acetate). Elution fractions were pooled and run over a HiTrap Heparin HP column (GE Healthcare). Column was then washed in wash buffer B (20 mM Hepes, pH 8.4, 200 mM NaCl) and eluted using a gradient of wash buffer B and elution buffer B (20 mM Hepes, pH 8.4, 1.5 M NaCl, 100 μM zinc acetate). Elutions were pooled and dialyzed into storage buffer as in Pagano et al., 2007 (20 mM Tris, pH 8.3, 20 mM NaCl, 100 μM zinc acetate, 10% (vol/vol) glycerol). Protein concentration was determined by measuring absorbance at 280 nm as in Pagano et al., 2007 and stored at -80°C.

Immunostaining - Adult worms were placed into M9 salt solution on epoxy autoclavable slides (thermo-fisher) and squashed with a coverslip to extrude embryos. Slides were frozen by laying on pre-chilled aluminum blocks for 20 minutes (chilled using dry ice). Embryos were permeabilized by freeze-cracking (removal of coverslips from slides) followed by incubation in methanol at -20°C for >15 minutes, and in acetone (pre-chilled at -20^{o}C) at room temperature for 10 minutes. Slides were blocked in PBS-Tween (0.1%) BSA (0.5%) for 15 minutes x 2, and incubated with 50 ul primary antibody overnight at 4°C in a humid chamber. Antibody dilutions (in PBST/BSA): K76 (1:10, DSHB, RRID:AB_531836), Rat α OLLAS-L2 (1:200, Novus Biological, RRID:

AB_1625980), mouse α FLAG (1:500, Sigma, RRID:AB_439685). Secondary antibodies were applied for 2 hours at room temperature.

Confocal Microscopy - Fluorescence microscopy was performed using a Zeiss Axio Imager with a Yokogawa spinning-disc confocal scanner. Images were taken and stored using Slidebook v 6.0 software (Intelligent Imaging Innovations) using a 63x objective. For live imaging, embryos were dissected from adult hermaphrodites in M9 salt solution and mounted onto 3% agarose pads. All embryo images are z stack maximum projections using a z step size of 1 μm, spanning the entire width of the embryo.

Quantification of MEG-3::GFP fluorescence from confocal images - Equally normalized time-lapse images were quantified using Slidebook v 6.0. Average fluorescence intensity relative to area of anterior (60%) and posterior (40%) of zygote were quantified and average fluorescence intensity relative to area of background (outside of zygote) was subtracted from each of these values. For each time-point, anterior and posterior fluorescence were expressed as fractions of total fluorescence and then normalized to T_0 (14 minutes prior to mitosis). Final values represent average of three embryos. Error bars show standard deviation of the mean.

Electrophoretic Mobility Shift Assay (EMSA) - EMSA were carried out as described in Pagano et al. 2007. Reactions consisted of 50 nM 3' Fluorescein-labeled RNA oligonucleotides (Dharmacon -GE Lifesciences) incubated with protein for 2 hours or more at room temperature or for 30 minute followed by 2 hour incubation with unlabeled competitor. Samples were run on 1% agarose gel in 1x TAE. Gels were scanned immediately using typhoon FLA-9500 with blue laser at 473 nm.

Fluorescence Polarization Assay - Equilibration reactions were performed using same protocol as for EMSAs. Reactions were transferred to 384 well microplates (Greiner Bio-One). The apparent fluorescence polarization was determined using a Clariostar monochromator microplate reader with fluorescein-sensitive filters and polarizers. Polarization values were normalized relative to saturation polarization value. For each experiment, values of three reads were averaged. Average values and standard errors from at least three technical replicates were calculated and plotted against each protein concentration. These data were fit to a quadratic equation (equation 1, where b is the base polarization, m is the maximum polarization, R is the labeled nucleic acid concentration, and P is the total protein concentration) as in (Pagano, Clingman et al. 2011), to calculate the apparent dissociation constant. The reported values are the dissociation constants calculated using the polarization values averaged from all technical replicates. The reported errors are standard error values calculated from the dissociation constant of each individual technical replicate.

Equation 1

$$\phi = b + (m - b) \times \left[\frac{R + P + K_{d,app} - \sqrt{\left(R + P + K_{d,app}\right)^2 - (4RP)}}{2R} \right]$$

Phase Separation Assay - His::tagged MEG-3 fusions were quickly diluted out of urea into condensation Buffer (25mM HEPES, pH7.4, NaCl adjusted to a final concentration of 150mM) in the presence and absence of poly-U30 RNA. Dilutions were performed by adding buffer to protein in low-binding siliconized Eppendorf tubes and mixing briefly by pipetting. The reaction was either spun at 3000 rpm for 2 minutes or transferred directly into 35mm glass bottom dish (Cat. No. P35G-1.5-14-C MatTek Corp) for imaging. Phase separation assays with MEX-5 were performed by pre-incubating 3.5μM 6xHis::MBP::MEX-5 protein (dialyzed into condensation buffer) with condensation buffer and poly-U30 RNA for 30 minutes before diluting in MEG-3. Differential interference contrast (DIC) images were obtained on an Olympus inverted microscope, using a 100X objective. Images were taken and stored using Slidebook v 4.0 and 5.0. All images are a single focal plane focused on the slide surface. For each phase separation experiment, we took three separate images of an 80 x 80 micron field and counted the condensates using Image J64. To recognize condensates, background was subtracted from each image using a rolling ball radius of 10 pixels, a pixel brightness threshold was set to 15-255. Remaining pixels were smoothed 3 times and size and number of objects greater than 0.032 μm^2 were quantified. Quantifications were manually verified for each image used. At least 3 technical replicates were quantified for each condition. Average number of condensates and S.E.M were calculated using all technical replicates.

Western Blots - Western blots were performed by running worm lysates on 7% Tris Acetate SDS PAGE precast gels (Bio-Rad). Protein was transferred to nitrocellulose membrane which was pre-blocked in 5% Milk diluted in PBS-Tween (0.1%) for 5

minutes (3 times). Membrane was then incubated with Primary antibody for at least 18 hours at 4° C or 2 hours at room temperature. Membranes were washed and blocked in 5% milk for 5 minutes (3 times) and incubated with secondary HRP conjugated antibody for 45 minutes at room temperature. Membranes were washed in 5% milk for 5 minutes (2 times) and PBST for 5 minutes (1 time). Membranes were then exposed to ECL substrate for 1 minute and then exposed to film. Primary antibody dilutions (in 5% Milk PBST): Rat α OLLAS-L2 (1:1000, Novus Biological), Mouse α Tubulin (1:1000, Sigma).

Technical v Biological Replicates - All *in vivo* biological replicates refer to experiments performed on independently isolated hermaphrodites (in the case of mutants, this refers to separate strains isolated from independent editing events) or independently treated hermaphrodites (in the case of RNAi, this refers to wild-type worms exposed to independent RNAi treatments). *In vitro* biological replicates refer to experiments performed with independently purified protein preps. All *in vivo* technical replicates refer to observations in the same strain from separate zygotes. In vitro technical replicates refer to separate experiments performed using the same purified protein preps.

Acknowledgements

We thank Erik Griffin for discussions, the CGC (USA) for strains, the Berger lab (JHU) for reagents and use of their microplate reader, Alex Paix for the *glh(ax3064)* allele, and the JHMI microscope facility for instruction. Research in the Seydoux lab is supported by R01 HD37047 from the National Institute of Health. G. Seydoux is an Investigator of the Howard Hughes Medical Institute.

1.5 Figures

Figure 1 – Localization of P granule proteins during zygote polarization

A. Photomicrographs of live wild-type (mCherry::MEX-5 and GLH-1::eGFP) or fixed *meg-4* zygotes (MEG::3 OLLAS and PGL-1) at three different stages: before polarization (pronuclear formation), during polarization (pronuclear migration) and after polarization (mitosis). *meg-4(ax3052)* zygotes were co-immunostained for MEG-3::OLLAS (anti-OLLAS, Novus Biological), and PGL-1 (K76, DSHB). *meg*-4 is required redundantly with *meg-3* for P granule assembly, and each is sufficient to support localized granule assembly (Wang, Smith et al. 2014). In this and subsequent figures, dashed lines outline each embryo, embryos are oriented with anterior to the left and posterior to the right and are ~50 μM long. At least three embryos were examined per genotype shown.

B. MEG-3::GFP levels in anterior and posterior halves of the zygote during polarization. Values represent average fluorescence intensity over time (relative to initial levels) in the anterior (red) and posterior (blue). Averages come from values measured from 3 different embryos. Error bars represent standard deviation of the mean.

C. Photomicrographs of fixed zygotes after polarization immunostained for OLLAS, PGL-1, or FLAG. *mex-5/6* zygotes were derived from wild-type hermaphrodites treated with *mex-5* and *mex-6* RNAi. *meg-3/4* zygotes were derived from *meg-3(ax3055); meg-4(ax3052)* hermaphrodites. *pgl-1/3* zygotes were derived from *pgl-3(bn104)* hermaphrodites treated with *pgl-1* RNAi (see Figure 1—figure supplement 1 for additional examples of *pgl-1(RNAi);pgl-3(bn104)* zygotes also stained for PGL-1 to verify loss of PGL-1).

Figure 2 - MEX-5 is necessary and sufficient to disassemble MEG-3 granules *in vivo*

A. Photomicrographs of mCherry tagged live zygotes [wild-type and *mex-5(S404A)*] or fixed zygotes expressing MEX-5 tagged with an OLLAS epitope [*mex-5(ZF-);mex-6(RNAi)*] at pronuclear meeting to show MEX-5 localization. Wild-type MEX-5 is in an anterior-rich gradient, whereas MEX-5(S404A) and MEX-5(ZF-) are uniformly distributed. Numbers indicate number of zygotes exhibiting phenotype shown / total number of zygotes examined.

B. Photomicrographs of live embryos expressing MEG-3::GFP. Genotypes at the *mex-5* locus are as indicated. Numbers indicate the numbers of zygotes examined as in A. In 1/10 *mex-5(ZF-, S404A); mex-6(RNAi)* zygotes, MEG-3 granules were asymmetric possibly due to incomplete depletion of MEX-6 by RNAi.

Figure 3 – MEG-3 Binds RNA *in vitro*

A. Binding of MEG-3 to poly-uridine 30 (poly-U30) is shown by electrophoretic mobility shift assay (EMSA) using fluorescein-labeled poly-U. EMSAs are shown for (top to bottom) full length MEG-3, MEG-3_{IDR}, and MEG-3_{Cterm}. Unbound poly-U30 is denoted by an asterisk (*). For each image shown, $n \geq 3$ technical replicates.

B. Fluorescence Polarization of poly-U30 by MEG-3. Fluorescence polarization values normalized relative to saturation are shown for full length MEG-3 (green), MEG-3_{IDR} (black), and MEG-3_{Cterm} (red). Values represent averages of ≥ 3 technical replicates. A fit of the polarization as function of protein concentration is plotted and used to calculate the given $K_{d,app}$. Error bars report S.E.M. Expanded graphs are shown in Figure 3—figure supplement 1.

Figure 4 – Stimulation of MEG-3 phase separation by RNA

A. Bar graph showing the number of condensates formed by 0.5 μM MEG-3 or MEG-3_{IDR} in the presence of increasing poly-U30. Values represent averages from 3 technical replicates. Error bars indicate S.E.M.

B. Photomicrographs of phase separation assay showing condensate formation of 5 μM full length MEG-3 incubated with poly-U RNA and/or MEX-5 as indicated.

C. Violin plots showing condensate size and number for each experiment represented in B The height of the plot shows the area of condensates in μm^2. The width of the plot correlates to the proportion of condensates of that size. Numbers inside each violin plot are the total number of condensates pooled from three technical replicates for each condition. An additional control is shown in Figure 4—figure supplement 2.

Figure 5 – Coalescence of MEG-3_{IDR} can be stimulated by blocking mRNA turnover *in vivo*

A. Photomicrographs of fixed embryos expressing MEG-3_{IDR} tagged with OLLAS epitope. First row are zygotes (one-cell stage) and second row are later stage embryos as indicated.

B. Photomicrographs of fixed zygotes expressing MEG-3_{IDR} tagged with OLLAS epitope. Genotypes are indicated above each embryo (left to right: wild-type, *mex-5/6(RNAi)*, and *let-711*(*RNAi)*). Numbers indicate number of zygotes exhibiting phenotype shown / total number of zygotes examined. In 1/8 *let-711*(*RNAi)* zygotes, MEG-3_{IDR} formed granules but these were smaller and confined to the posterior half of the zygote, possibly due to incomplete depletion of *let-711*.

Figure S1 – MEG-3 localizes before PGL-1 and does not require PGL-1 or PGL-3 to assemble granules.

A. Photomicrographs of live MEG-3::GFP in zygotes at three different stages: before polarization (pronuclear formation), during polarization (pronuclear migration) and after polarization (mitosis). These and similar images taken from 3 zygotes at 14 time points were used to quantify MEG-3::GFP fluorescence levels over time as shown in Figure 1B.

B. Photomicrographs of fixed wild-type and *meg-3/4* zygotes after polarization immunostained for PGL-3. *meg-3/4* zygotes were derived from *meg-3(ax3055); meg-4(ax3052)* hermaphrodites. PGL-3 staining was done using the KT3 antibody (DSHB).

C. Photomicrographs of fixed zygotes stained with anti-FLAG (top) and K76 anti-PGL-1 (bottom) to show MEG-4 localization at the 1-cell (left) and 4-cell (right) stages. *pgl-1/3* zygotes were derived from *pgl-3(bn104); meg-4(ax2080$^{FLAG\ tag}$)* hermaphrodites treated with *pgl-1* RNAi.

Figure S2 – Expression of MEX-5, and MEX-5(ZF-), MEG-3, and MEG-3$_{IDR}$

A. MEX-5 functions redundantly with MEX-6 to localize MEG-3: Photomicrographs of live wild-type and *mex-5(RNAi)* zygotes co-expressing mCherry:MEX-5 and MEG-3::GFP. Loss of mCherry fluorescence in the *mex-4(RNAi)* zygotes was used to confirm efficient loss of mCherry::MEX-5. Numbers indicate number of zygotes exhibiting phenotype shown / total number of zygotes examined.

B. Western blot of embryo lysates co-blotted with α OLLAS and α tubulin (loading control). Expected sizes for protein-epitope fusions are indicated on the right by a < symbol. N2 lysate is a control lysate expressing no tagged proteins, all others are lysates from embryos expressing tagged proteins as indicated.

C. Bar graph showing relative expression of MEG-3 and MEX-5. Western blot in figure S2A was quantified using Image J. MEX-5 is 10X more abundant than MEG-3.

Figure S3 – MEG-3 RNA binding

A. Coomassie stained gel showing His-tagged MEG-3 proteins. Expected sizes are indicated on the right. Each lane is from a separate gel.

B. RNA-RNA competition EMSA. 300nM MEG-3 (300 nM) was incubated with 50nM poly-U30 and increasing amounts of unlabeled 30-mer RNAs as indicated to the left of each panel. The first lane of each gel contains only labeled poly-U RNA. The last lane of each gel contains poly-U RNA and the highest concentration of unlabeled competitor RNA (5000 nM). The unbound poly-U RNA is denoted by an asterisk (*). Double asterisks (**) in the poly-G assay denote a band that arises due to an interaction between poly-G and poly-U (independent of MEG-3). For each image shown, n = 2 technical replicates.

C. Fluorescence Polarization of polyuridine by MEG-3 (expanded from Figure 3). Fluorescence polarization values normalized relative to saturation are shown for full length MEG-3 (top, green), MEG-3_{IDR} (middle, black), and MEG-3_{Cterm} (bottom, red). Values represent averages of ≥ 3 technical replicates. A fit of the polarization as function of protein concentration is plotted and used to calculate the given $K_{d,app}$. Error bars report S.E.M.

Figure S4 – Phase Separation assay titration

A. Phase separation assay titration. DIC images of MEG-3 solutions in the presence of increasing concentrations of protein and RNA. MEG-3 was diluted into phase separation buffer (25mM HEPES, pH7.4, NaCl adjusted to a final concentration of 150mM) at room temperature. The solution was transferred to a glass bottom dish and the dish surface was photographed using an inverted DIC microscope 10 minutes after the initial dilution (room temperature).

B. Phase Separation Assay Controls. Same as above except 3' fluorescein labeled poly-U RNA was included in the buffer. DIC images (left) show the MEG-3 condensates and fluorescence images (488 channel) show the 3' fluorescein labeled poly-U RNA concentrated in the condensates.

C. Violin plots showing condensate size and number comparing MEG-3 alone and MEG-3 + MEX-5 (Additional data). As in Figure 4C, the height of the plot shows the area of condensates in μm^2. The width of the plot correlates to the proportion of condensates of that size. Numbers inside each violin plot are the total number of condensates pooled from three technical replicates for each condition. Data for the MEG-3 alone sample are the same as in Figure 4C and shown here only for reference.

Figure S5 – MEG-3$_{IDR}$ *in vivo*

Western blot of mixed-stage embryo lysates co-blotted with α OLLAS and α tubulin. Expected sizes for protein-epitope fusions are indicated on the right by a < symbol. Dashed line indicates a break in the original gel. Genotype is indicated on the bottom. The MEG-3$_{IDR}$ is present at higher level than MEG-3, likely due to the fact that unlike MEG-3, MEG-3$_{IDR}$ persists longer in somatic cells (see Figure 5 and data not shown). The significance of this difference is not known. n = 3 technical replicates.

Table S1 – Strains used in this study

All strains were generated in this study by genome editing or crossing. No transgenic lines were used. Independent edits displayed the same phenotypes. The *mex-5(S404A)* lines could not be maintained due to semi-dominant maternal-effect sterility (91.6%) and recessive maternal-effect lethality (100%).

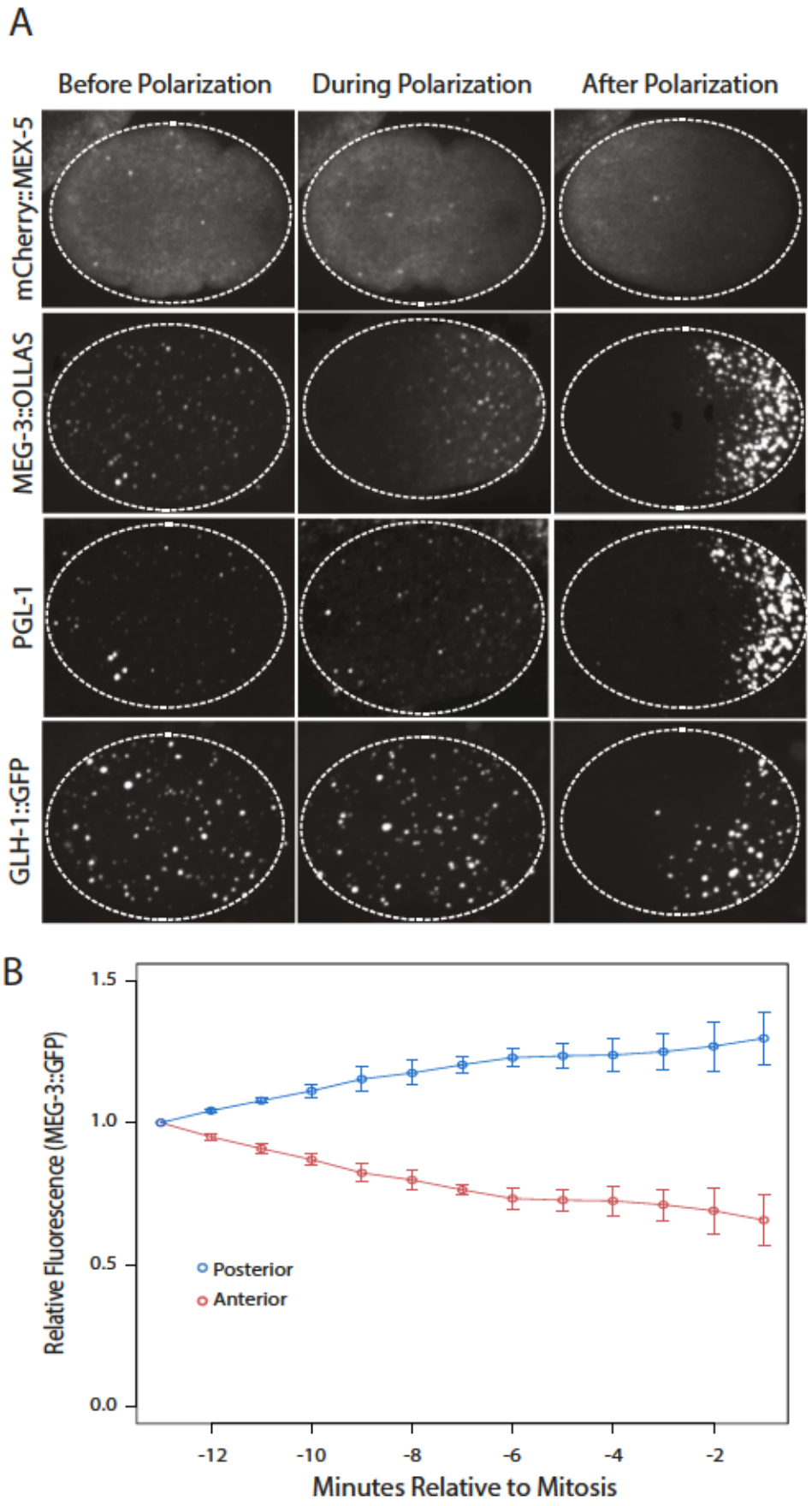
A
Before Polarization
During Polarization
After Polarization
mCherry::MEX-5
MEG-3::OLLAS
PGL-1
GLH-1::GFP
B
Relative Fluorescence (MEG-3::GFP)
1.5
1.0
0.5
0.0
Posterior
Anterior
-12
-10
-8
-6
-4
-2
Minutes Relative to Mitosis
C
WT
pgl-1/3
mex-5/6
meg-3/4
MEG-4::3xFLAG
MEG-3::OLLAS
PGL-1

Figure 1

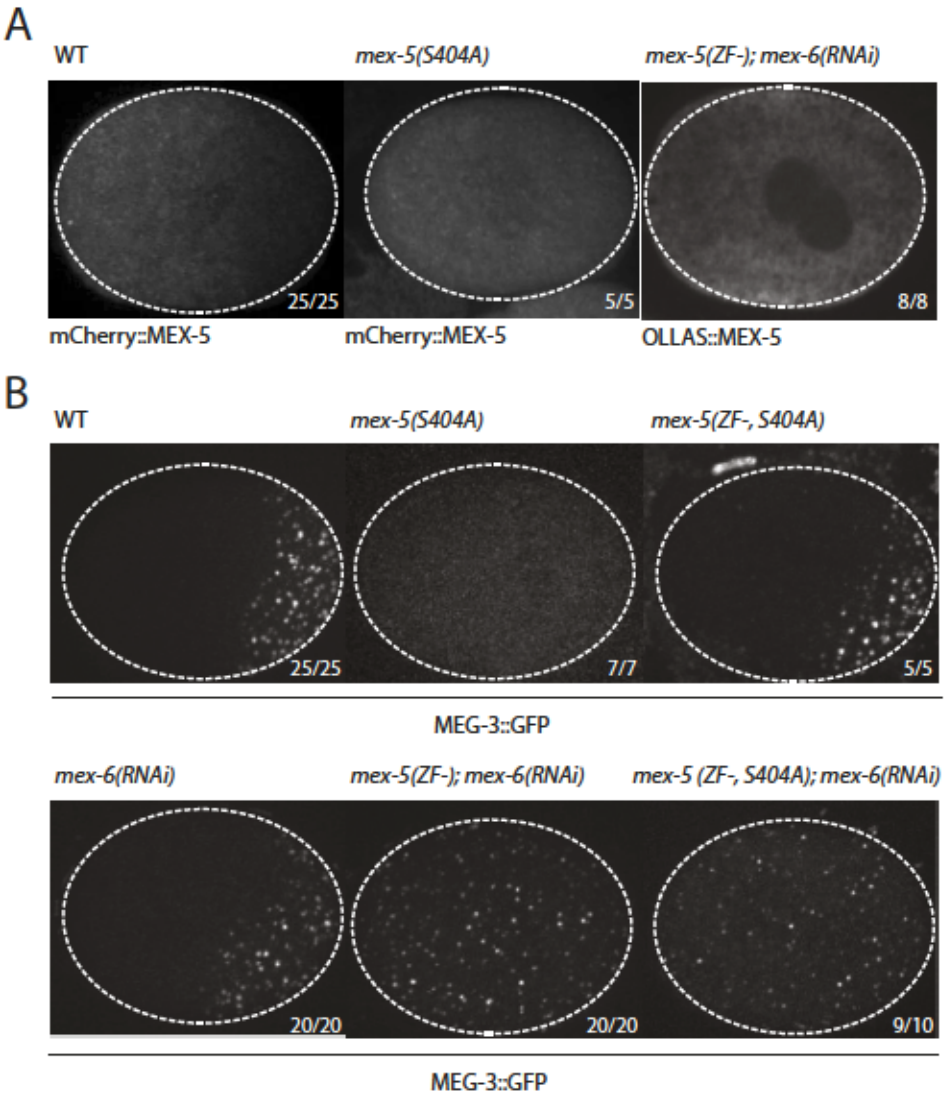
A
WT
mex-5(S404A)
mex-5(ZF-); mex-6(RNAi)
25/25
5/5
8/8
mCherry::MEX-5
mCherry::MEX-5
OLLAS::MEX-5
B
WT
mex-5(S404A)
mex-5(ZF-, S404A)
25/25
7/7
5/5
MEG-3::GFP
mex-6(RNAi)
mex-5(ZF-); mex-6(RNAi)
mex-5 (ZF-, S404A); mex-6(RNAi)
20/20
20/20
9/10
MEG-3::GFP

Figure 2

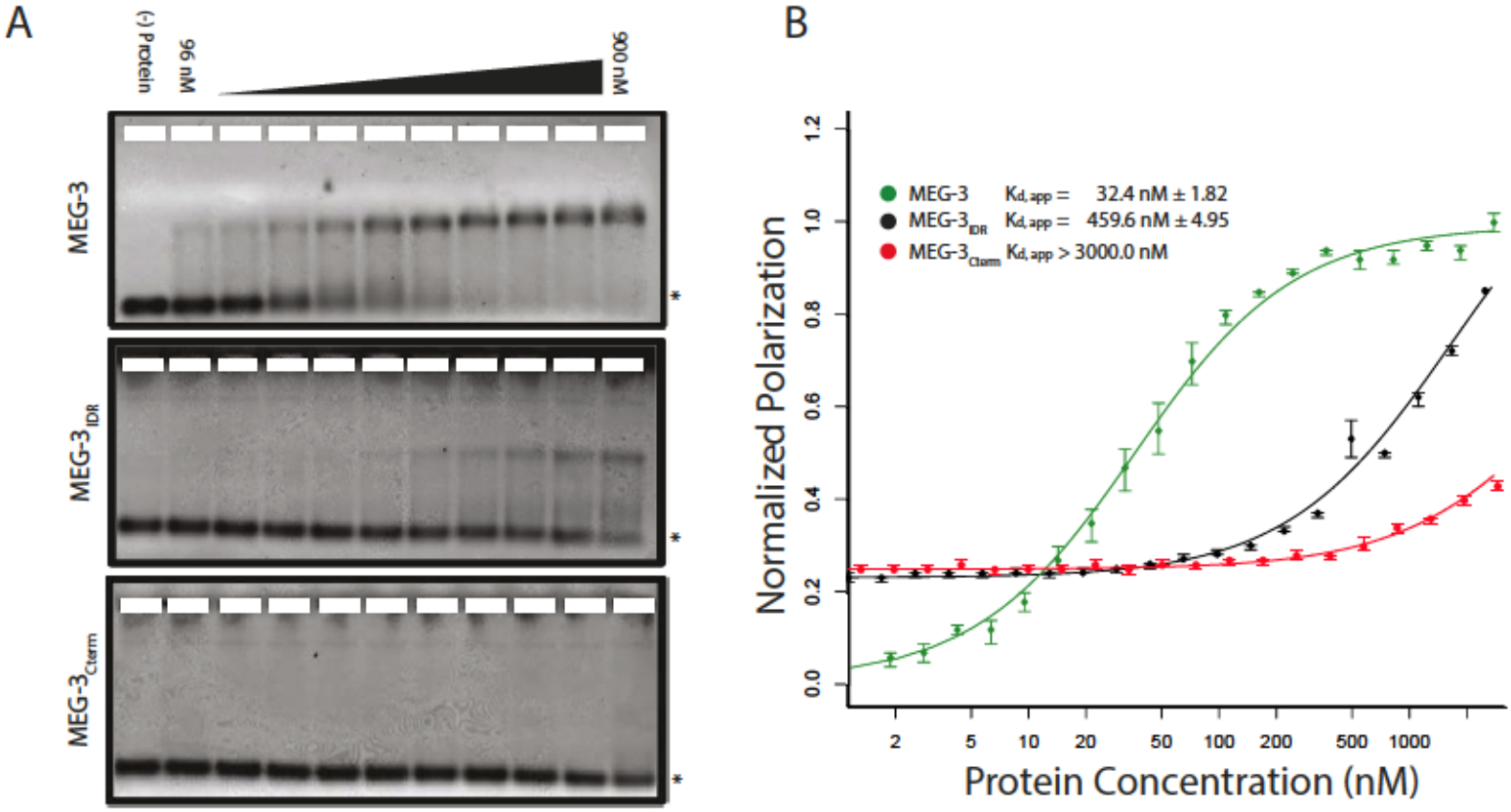
A
(-) Protein
96 nM
900 nM
MEG-3
MEG-3IDR
MEG-3Cterm
*
*
*
B
MEG-3 Kd,app = 32.4 nM ± 1.82
MEG-3IDR Kd,app = 459.6 nM ± 4.95
MEG-3Cterm Kd,app > 3000.0 nM
Normalized Polarization
0.0
0.2
0.4
0.6
0.8
1.0
1.2
2
5
10
20
50
100
200
500
1000
Protein Concentration (nM)

Figure 3

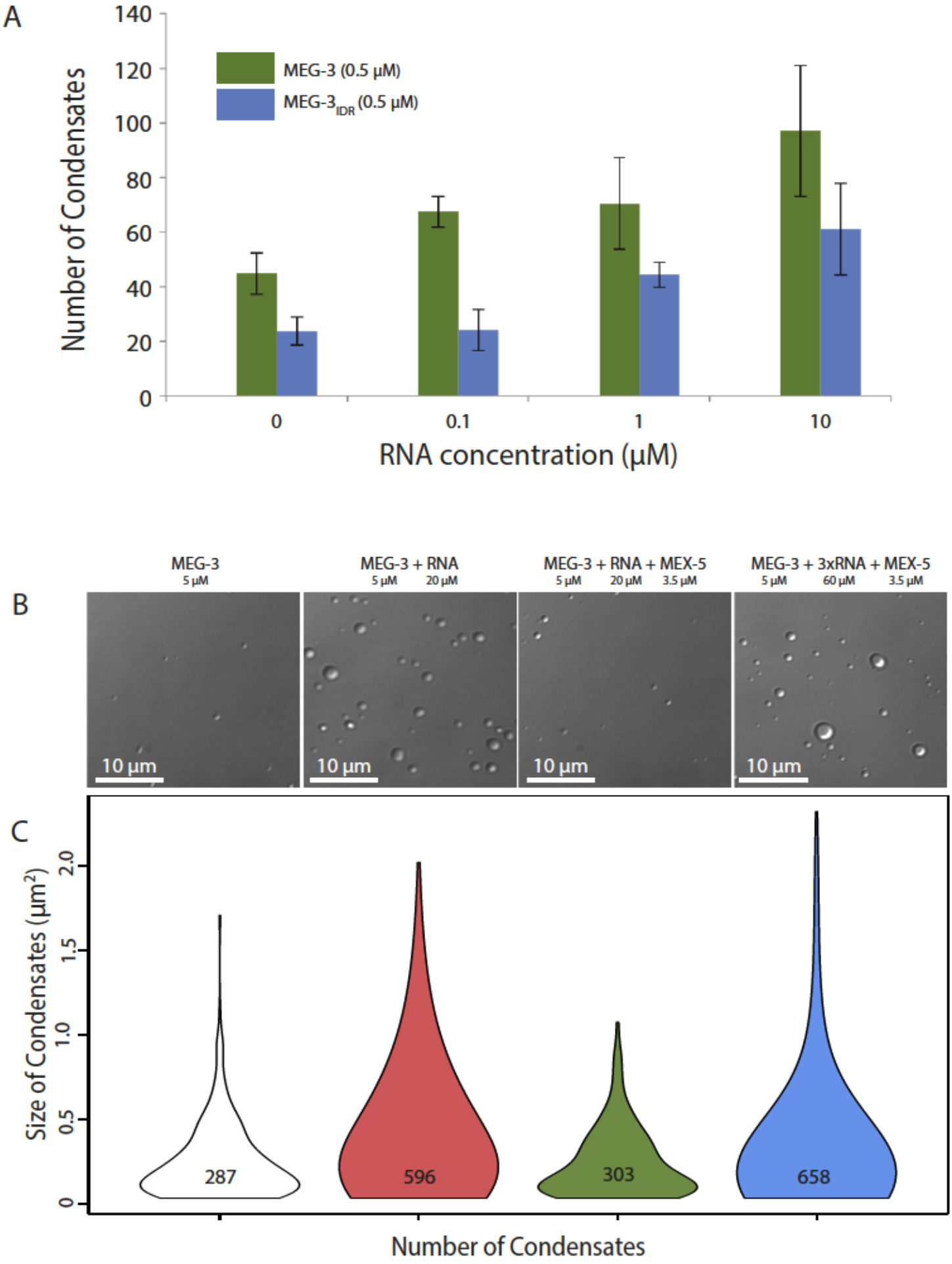
A
140
120
100
80
60
40
20
0
Number of Condensates
MEG-3 (0.5 μM)
MEG-3IDR (0.5 μM)
0
0.1
1
10
RNA concentration (μM)
B
MEG-3
5 μM
MEG-3 + RNA
5 μM
20 μM
MEG-3 + RNA + MEX-5
5 μM
20 μM
3.5 μM
MEG-3 + 3xRNA + MEX-5
5 μM
60 μM
3.5 μM
10 μm
10 μm
10 μm
10 μm
C
Size of Condensates (μm2)
0
0.5
1.0
1.5
2.0
287
596
303
658
Number of Condensates

Figure 4

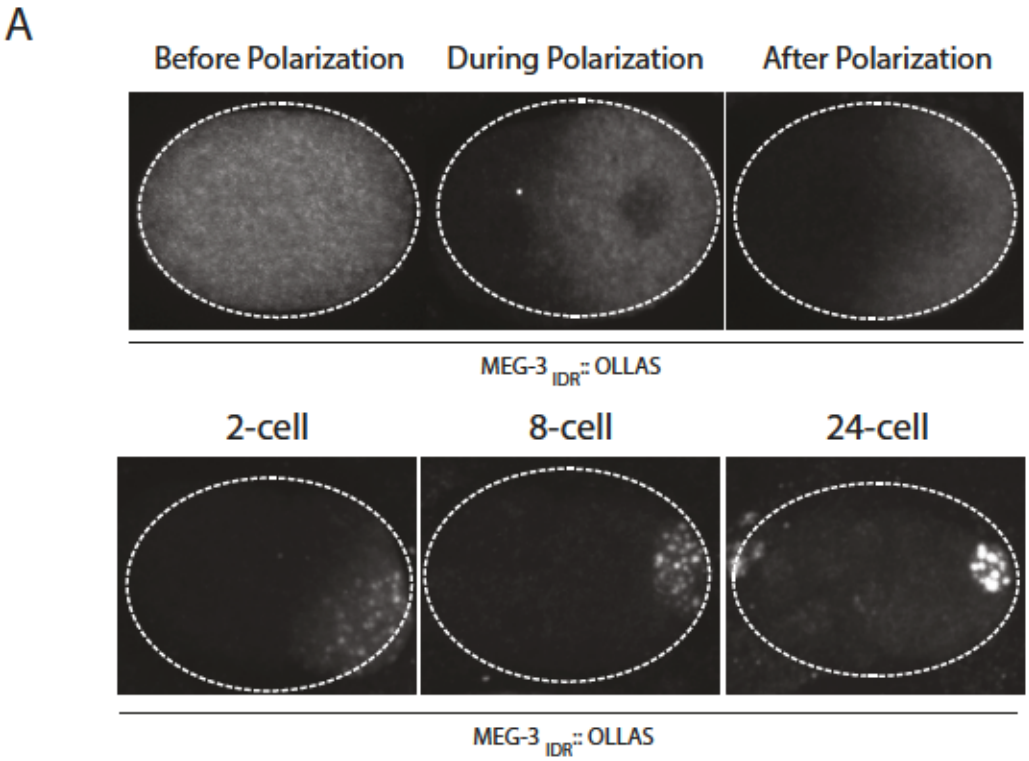
A
Before Polarization
During Polarization
After Polarization
MEG-3 IDR:: OLLAS
2-cell
8-cell
24-cell
MEG-3 IDR:: OLLAS
B
WT
mex-5/6(RNAi)
let-711(RNAi)
7/7
10/10
4/5
MEG-3 IDR:: OLLAS

Figure 5

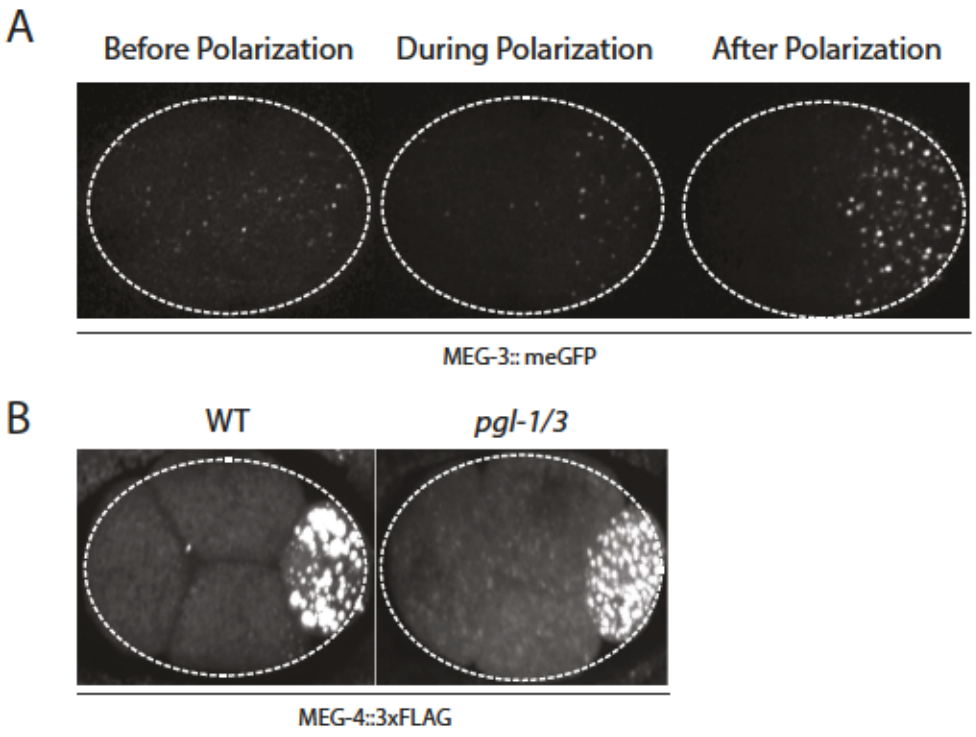
A
Before Polarization
During Polarization
After Polarization
MEG-3:: meGFP
B
WT
pgl-1/3
MEG-4::3xFLAG

Figure S1

A

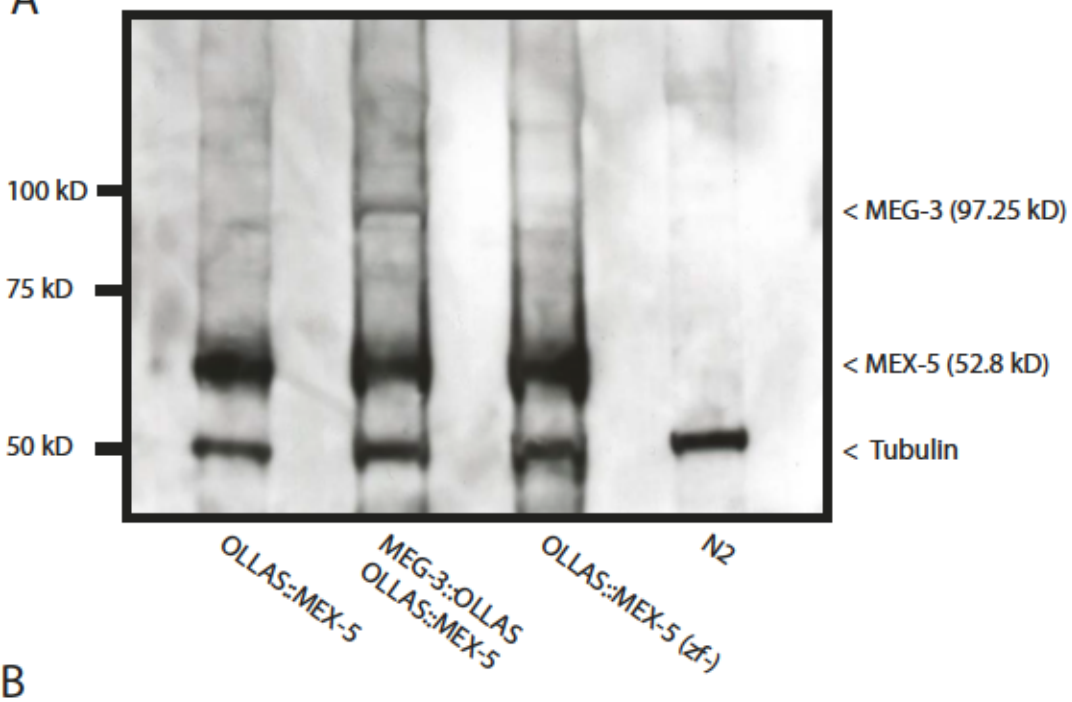
100 kD
75 kD
50 kD
< MEG-3 (97.25 kD)
< MEX-5 (52.8 kD)
< Tubulin
OLLAS::MEX-5
MEG-3::OLLAS
OLLAS::MEX-5
OLLAS::MEX-5 (zf-)
N2

B

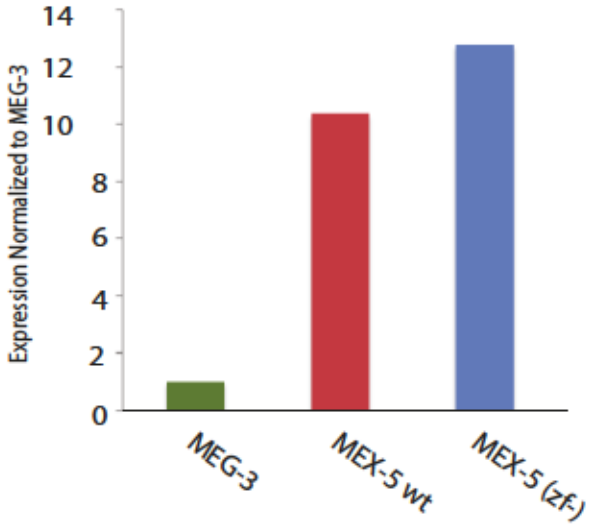
Expression Normalized to MEG-3
14
12
10
8
6
4
2
0
MEG-3
MEX-5 wt
MEX-5 (zf-)

Figure S2

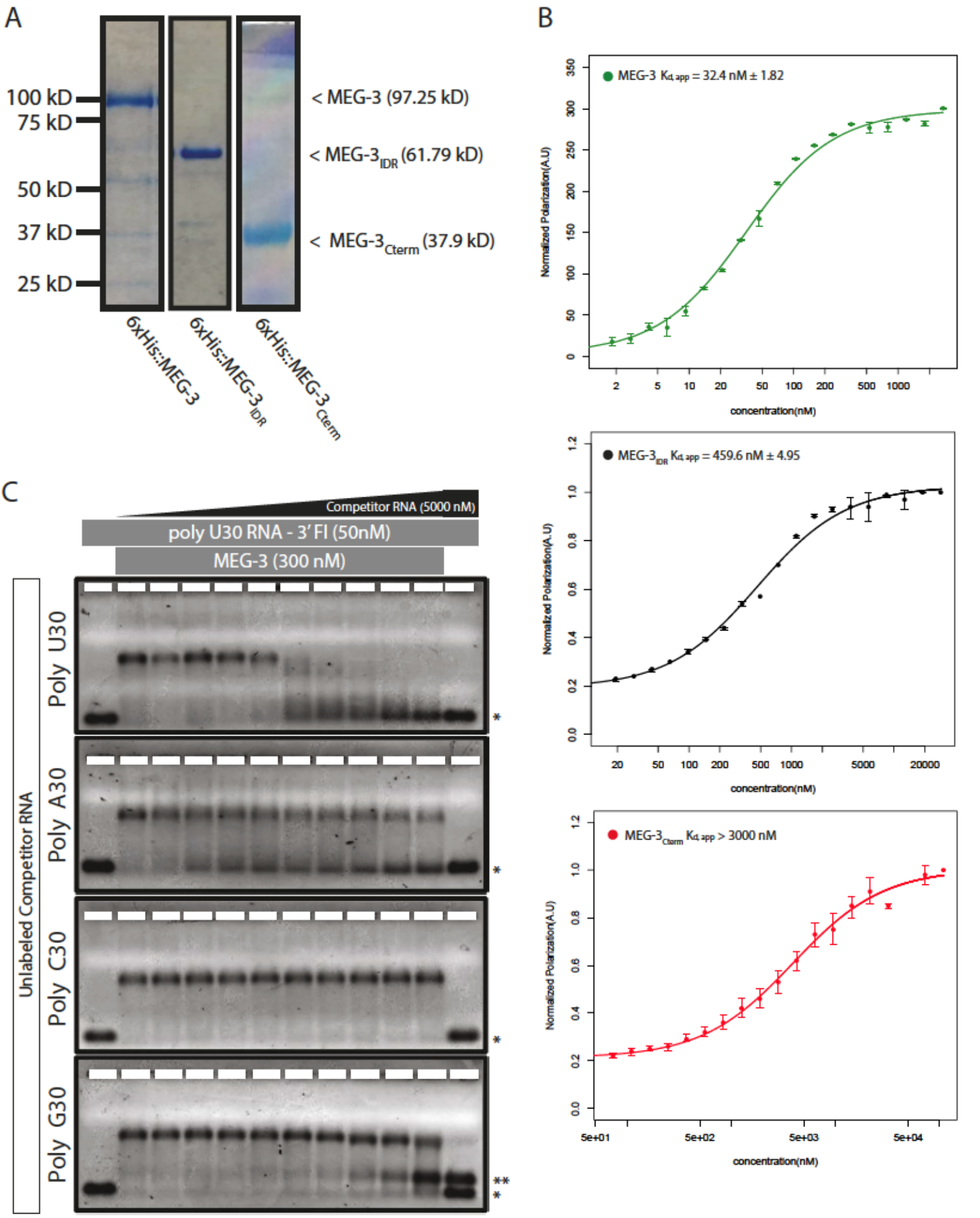
A
100 kD
75 kD
50 kD
37 kD
25 kD
< MEG-3 (97.25 kD)
< MEG-3IDR (61.79 kD)
< MEG-3Cterm (37.9 kD)
6xHis::MEG-3
6xHis::MEG-3IDR
6xHis::MEG-3Cterm
B
MEG-3 Kd,app = 32.4 nM ± 1.82
Normalized Polarization(A.U)
concentration(nM)
MEG-3IDR Kd,app = 459.6 nM ± 4.95
Normalized Polarization(A.U)
concentration(nM)
MEG-3Cterm Kd,app > 3000 nM
Normalized Polarization(A.U)
concentration(nM)
C
Competitor RNA (5000 nM)
poly U30 RNA - 3' FI (50nM)
MEG-3 (300 nM)
Unlabeled Competitor RNA
Poly U30
Poly A30
Poly C30
Poly G30

Figure S3

A

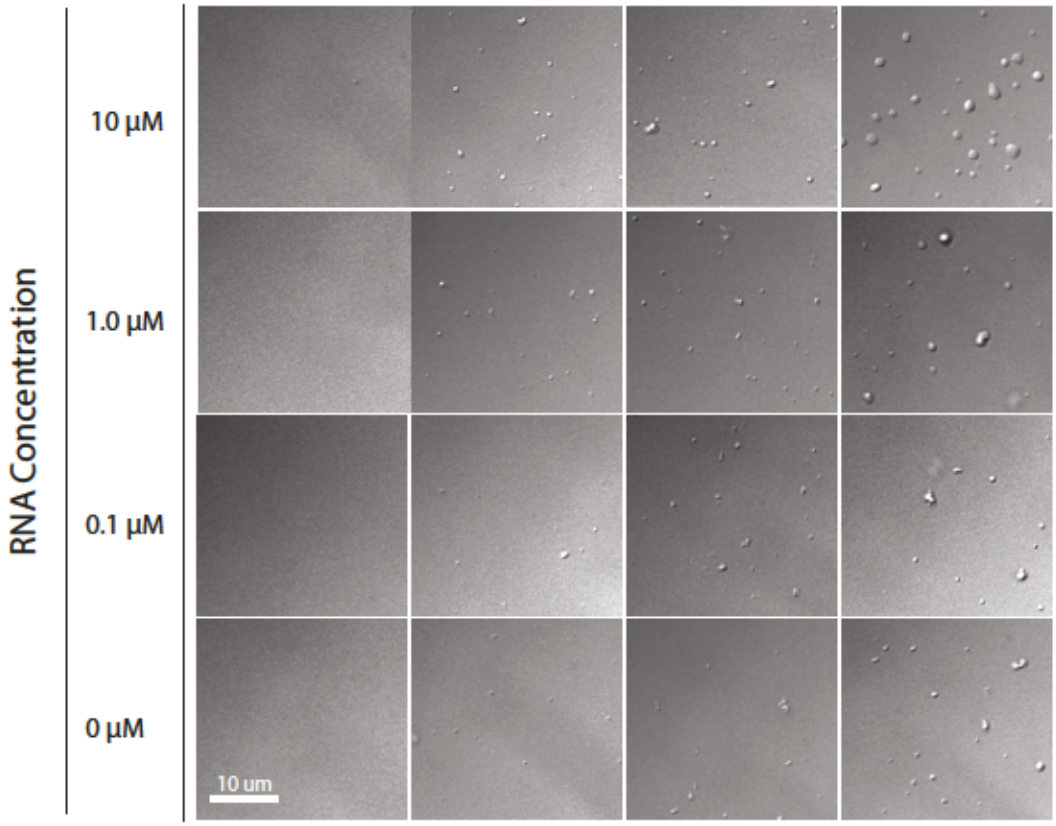
RNA Concentration
10 µM
1.0 µM
0.1 µM
0 µM
10 um
0.1 µM
0.5 µM
1.0 µM
5.0 µM
MEG-3 Concentration

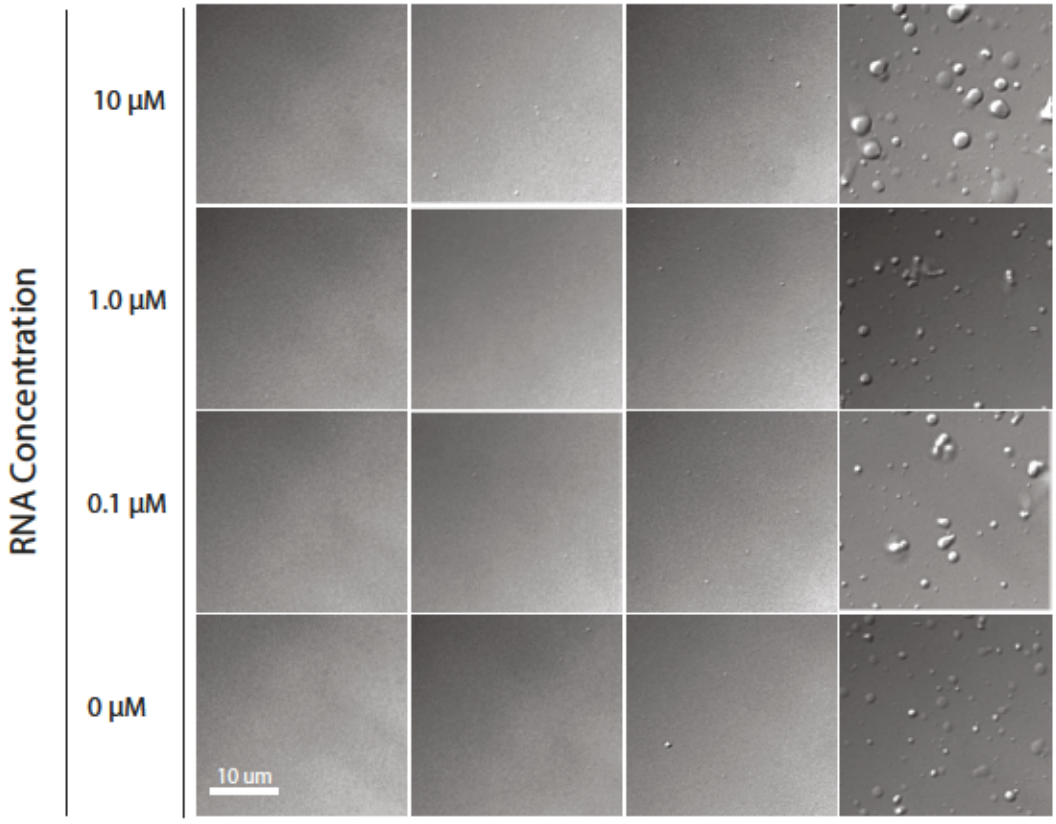
RNA Concentration
10 µM
1.0 µM
0.1 µM
0 µM
10 um
0.1 µM
0.5 µM
1.0 µM
5.0 µM
MEG-3IDR Concentration

Figure S4

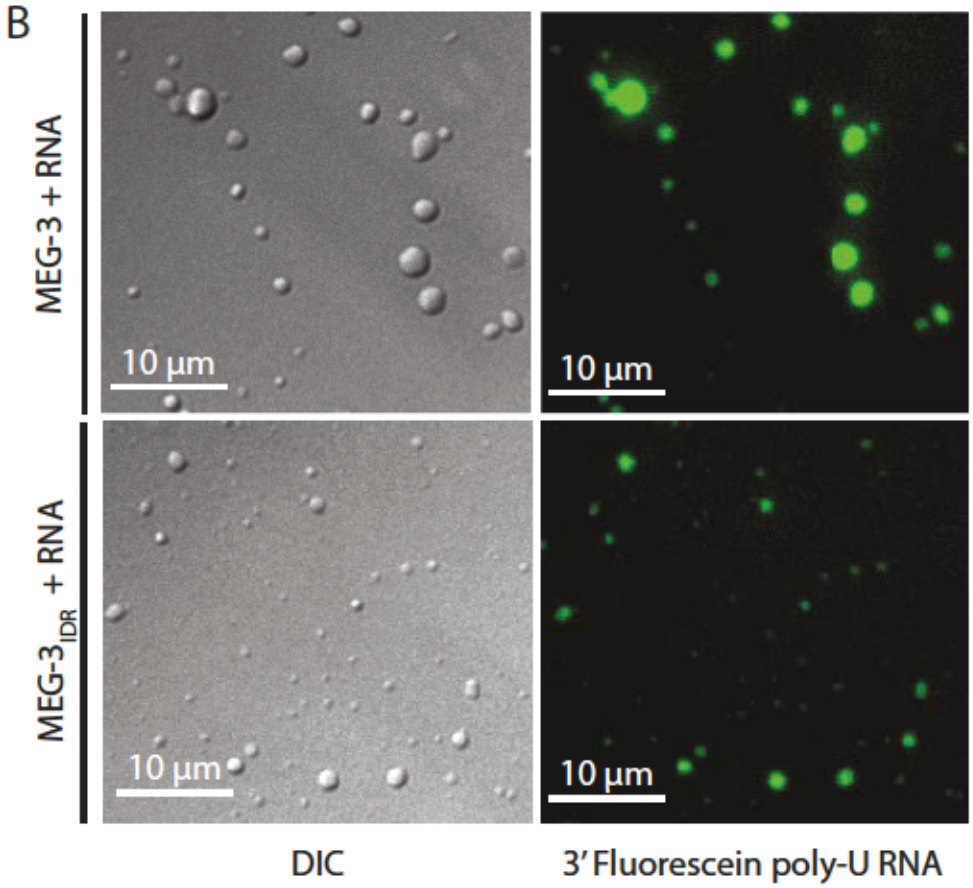
B
MEG-3 + RNA
MEG-3IDR + RNA
10 µm
10 µm
10 µm
10 µm
DIC
3' Fluorescein poly-U RNA

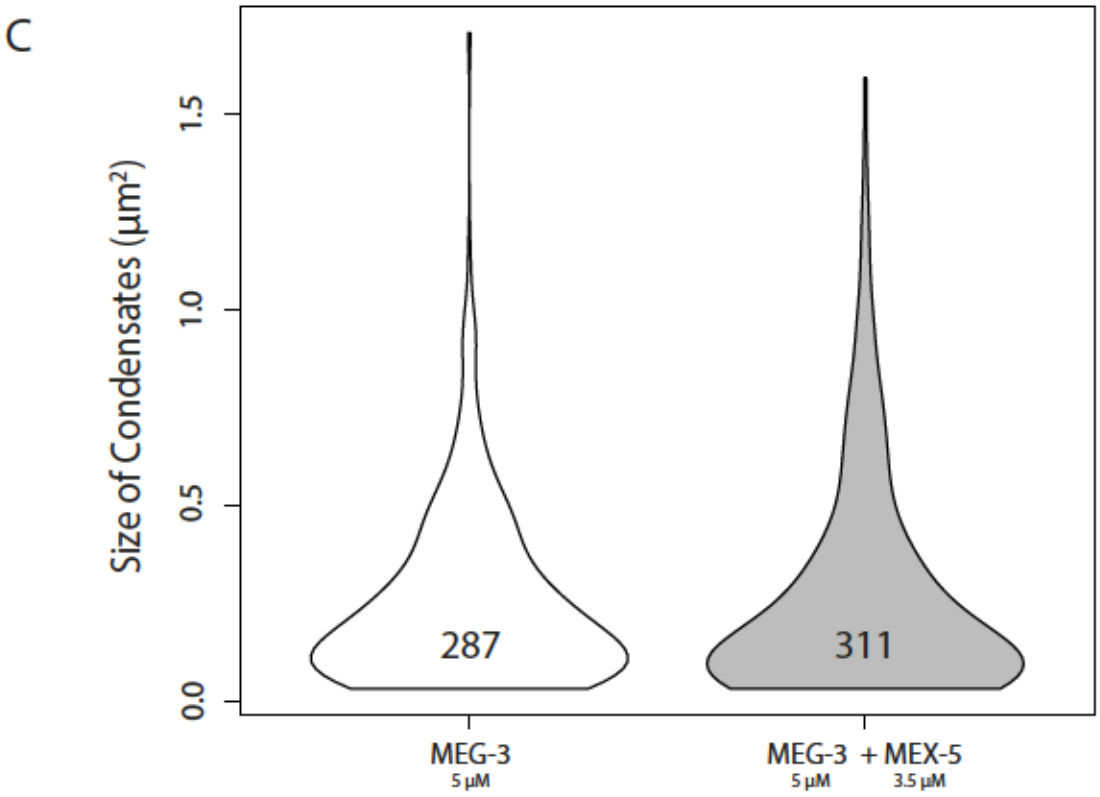
C
Size of Condensates (µm²)
0.0
0.5
1.0
1.5
287
311
MEG-3
5 µM
MEG-3 + MEX-5
5 µM
3.5 µM

Figure S4

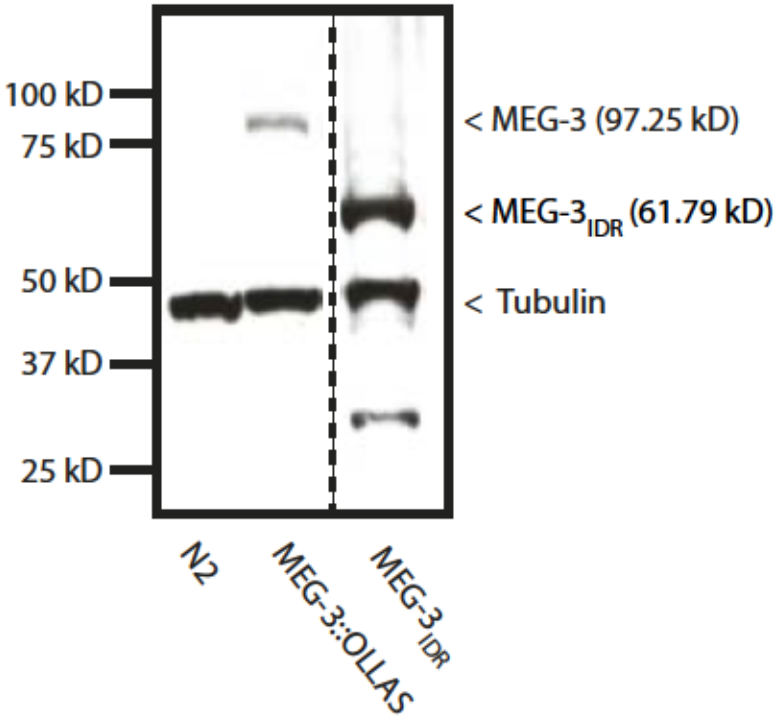
100 kD
75 kD
50 kD
37 kD
25 kD
< MEG-3 (97.25 kD)
< MEG-3IDR (61.79 kD)
< Tubulin
N2
MEG-3::OLLAS
MEG-3IDR

Figure S5

Strain	Genotype	Description	Method	Derived from	Guide RNA sequence	Repair Template(s)	Notes
JH3374	*meg-3(ax3051); meg-4(ax2080)*	MEG-3::OLLAS; MEG-4::3xFLAG	CRISPR/Cas9	JH3247[*meg-4(ax2080)*]	tcagtacaatcattgatctc	cggaaatcggatcctatcaaatacttgaatgtaaaacgggattggctggaatctatttttgatccaccccagagatcaatccggattcgccaacgagctc ggaccacgtctcatgggaaagtgattgtaccaatttatatctattacttgtagactatattgtatgttattcttgttcattaaccctttat	
JH3477	*meg-3(ax3051); meg-4(ax3052)*	MEG-3::OLLAS; *meg-4* deletion	CRISPR/Cas9	JH3374	tctgcccaggaacttgtaac, ggagtttggcagatcacatg	gttgcaggtatgagttcttcaaagctttcctcatgtgggaagtttgtccagagcagagg aacgggtagttttctattgttatcaggactgctgc	
JH3422	*meg-3(ax3056); meg-4(ax2080)*	MEG-3IDR::OLLAS; MEG-4::3xFLAG	CRISPR/Cas9	JH3247[*meg-4(ax2080)*]	tggagttgggatgattgacg, tcagtacaatcattgatctc	ggaacaatgtggatgtaaagagaacaccttcctgtccggattcgccaacgagctcggaccacgtctcatgggaaagagagatcaatgattgtacca attatatctattacttg	
JH3479	*meg-3(ax3056); meg-4(ax3052)*	MEG-3IDR::OLLAS; *meg-4* deletion	CRISPR/Cas9	JH3422	same as JH3477	same as JH3477	
JH3503	*meg-3(ax3054)*	MEG-3::meGFP	CRISPR/Cas9	N2	gaagtctgcagagaagacgg	PCR using primers gcaacgcctttaacagtatttcctcctacggcccccgtgagtaaaggagaagaac; gtttgcaagttgcggcggaagtctgcagagaagaccttgtacagctcgtccatgc on pap835	
JH3475	*meg-3(ax3055); meg-4(ax3052)*	*meg-3* delete; *meg-4* delete	CRISPR/Cas9	JH3477	tcctcaaaaccttacccaag, tcgagtttggcagaccgctt	gcaggtatgagttcctcaaaaccttacccaagggcaggatgtcagccagaggagggaatcctaattgtaccaatttatatctattacttgtagactatatt g	
JH3499	*mex-5(ax3057)*	MEK-5(ZF-):OLLAS	CRISPR/Cas9	JH3190[*mex-5(ax2043)*]	(r274) actacaagactcgtctttgc, (k318) gtacaagacaaagctgtgca	(r274e) gattcccaatttccagaaactgacagtcaacaaccaccaaattataaaacagagctctgcatgatgcacgcatctggaatcaaaccatgtg, (k318e) ctccggctcgctatccgaacaacaagtacaagacgagctctgtaaaaatttcgctcgtggaggaactggatttctgcccgtatg	2 independent edits
JH3500	*mex-5(ax3058); meg-3(ax3054)*	MEX-5(ZF-); MEG-3::meGFP	CRISPR/Cas9	JH3503	same as JH3499	same as JH3499	2 independent edits
JH3501	*mex-5(ax3059); meg-3(ax3054)*	MEK-5(ZF-,S404A); MEG-3::meGFP	CRISPR/Cas9	JH3500	gaucgcgaccagcauuggag	ctgatgtctttttctcaattacataatttttcagcgcaatgatgtgtctttccaatgccgggcgcgatcttcaagccggaggtgattacaatcaacc	2 independent edits
JH3296	*mex-5(ax3050)*	mCherry::MEX-5	CRISPR/Cas9	N2	ggcaucaaauagugucucgu, aauagugucucgucggccgg	PCR using primers gataatcaattgaatgtttcagacagagaatggtctcaaagggtgaagaagataacatggc; ggctgggttgtcgtaggtgacactgatcctcccgcggaggacacactatttgatgccgctttcttatacaattcatccatgccacctgtcgag on pCFJ90	
N/A	*mex-5(s404a) - no allele designated*	mCherry::MEX-5(S404A)	CRISPR/Cas9	JH3296	same as JH3501	same as JH3501	3 independent edits
N/A	*mex-5(s404a) - no allele designated*	MEX-5(S404A); MEG-3::meGFP	CRISPR/Cas9	JH3503	same as JH3501	same as JH3501	5 independent edits
JH3348	*mex-5(ax3050); glh-1(ax3064)*	mCherry::MEX-5 ; GLH-1::eGFP	Cross	JH3296 x JH3333[*glh-1(ax3064)*]			
JH3502	*mex-5(ax2043); meg-3(ax3051); meg-4(ax2080)*	MEG-3::OLLAS; OLLAS::MEX-5	Cross	JH3190[*mex-5(ax2043)*] x JH3374			
JH3288	*pgl-3(bn104); meg-4(ax2080)*	*pgl-3(bn104)*; MEG-4::3xFLAG	Cross	SS608[*pgl-1(bn104)*] x JH3247[*meg-4(ax2080)*]			

Table S1

Chapter 2

Active regulation of stable P granule core dynamics by

DDX family RNA-helicase CGH-1

2.1 Summary

P granules, RNA granules in the *C. elegans* germline, have been proposed to form by liquid-liquid phase separation or LLPS. LLPS is a spontaneous process that allows molecules to exchange passively between a high-concentration phase (P granules) and a low-concentration phase (cytoplasm). To test this hypothesis, we developed methods to extrude P granules from embryos to probe their behavior under a variety of conditions. Here we show that "scaffold" proteins essential for granule assembly (MEGs) behave differently from non-essential "client" proteins (PGL-1). While MEG-3 remains in granules when extruded into a dilute buffer, PGL-1 dissolves from granules immediately. MEG-3 granules are resistant to high salt and EDTA, but dissolve in 1,6 hexanediol, consistent with gel-like phase that is dependent on hydrophobic interactions. Remarkably, addition of ATP in the extrusion buffer causes MEG-3 granules to dissolve while addition of GTP and non-hydrolyzable ATP analogs has little effect. We also show that inactivation of the RNA helicase CGH-1 (DDX6 in humans) reduces MEG-3 granule ATP sensitivity and that embryos lacking CGH-1 exhibit large, non-dynamic MEG-3 granules as measured by FRAP. Together these findings suggest that P granules are scaffolded by a non-liquid, gel-like condensate that is kept dynamic by ATP-driven processes including remodeling by the conserved DDX helicase CGH-1. Formation of solid phases in RNA granules has been described as non-physiological and implicated in a number of neurodegenerative diseases, including ALS and Huntington's disease. Our findings suggest that solid or gel phases are natural components of RNA granules that are kept liquid-like and dynamic by ATP-dependent enzymes.

2.2 Results

MEG-3 but not PGL-3 persist as a stable P granule core when extruded from embryos

To examine the properties of P granules, we extruded the granules from the P cell of live embryos into egg buffer. We monitored the localization of the intrinsically-disordered protein MEG-3 and the RGG RNA-binding protein PGL-3 using a co-labeled strain. This strain expresses an endogenously tagged MEG-3::GFP CRISPR allele (MEG-3::GFP) and a transgenically expressed PGL-3::RFP. Prior to extrusion, both MEG-3::GFP and PGL-3::RFP localize to the P granules. After extrusion, PGL-3::RFP quickly (< 5 seconds) diffused away from granules, whereas MEG-3::GFP persisted in the granules (Figure 1A). An endogenously tagged CRISPR allele of the PGL-3 homologue, PGL-1, was also examined. We found that like PGL-3, PGL-1::GFP also quickly diffused away from extruded granules (Figure S1). The persistence of MEG-3::GFP on extruded granules was especially interesting because previous work had identified MEG-3 as being a critical scaffold for recruitment of other P granule components (Wang, Smith et al. 2014, Smith, Calidas et al. 2016). This result indicated that while some P granule components such as PGL-3 and PGL-1 may behave as in a liquid phase, the critical scaffolding component of P granules does not exhibit liquid behavior.

To further investigate the nature of the stable MEG-3 assemblies, we extruded MEG-3::GFP labeled P granules into a variety of buffers. MEG-3::GFP asssemblies were resistant to high salt (1M NaCl) suggesting that their stability was not dependent solely on electrostatic interactions. MEG-3 granules, however, were sensitive to SDS (0.5%) and 1,6 hexanediol (but not 2,5 hexanediol) (5%) suggesting that stable protein-

protein interactions and hydrophobic interactions may contribute to their stability (Figure 1B).

ATP acts as an energy source to drive active disassembly of *ex vivo* granules

The chemical properties of hydrotropes are also thought to limit or reverse phase separation of RNA granules. Hydrotropes are amphiphiles containing both a hydrophobic and charged regions (Patel, Malinovska et al. 2017). Adenosine triphosphate (ATP) has been hypothesized to act as a biologically relevant hydrotrope to prevent or limit phase separation in cells (Patel, Malinovska et al. 2017). To determine whether MEG-3 assemblies were sensitive to physiological levels of ATP, we extruded MEG-3::GFP labeled P granules into 5 mM ATP coordinated with Mg^{2+} ions (ATP*Mg). We found that MEG-3 granules extruded into 5 mM ATP*Mg dissolved within 60 seconds (Figure 2A, Figure 2B, Figure 2C). In contrast, ADP, AMP, ADPnP, and GTP had no effect on MEG-3 assemblies (Figure 2D). Because ADPnP and GTP are expected to be equally effective hydrotropes as ATP, and ADP and AMP are expected to have similar, but less pronounced effects (Patel, Malinovska et al. 2017), we reasoned that ATP may not be acting as a hydrotrope here, but as a source of energy for an ATP-consuming enzyme, .

Active ATP dependent processes have been known to play a role in determining the dynamics and viscosities of other phase separated cellular compartments such as the nucleolus (Brangwynne, Mitchison et al. 2011). In order to further test this hypothesis we also added EDTA to the extrusion buffer to chelate away Mg^{2+} ions. While the chemical identity of ATP as a hydrotrope does not require that it be coordinated with Mg^{2+} (Patel, Malinovska et al. 2017), ATP is not useful as a substrate to enzymes without Mg^{2+} available. We found that addition of EDTA almost entirely ablated the effects of

ATP*Mg on granule disassembly, supporting a model in which ATP acts as an energy source to drive granule disassembly (Figure 2D).

The ATPase activity of DDX RNA helicase CGH-1 contributes to P granule dynamics *ex vivo*

To identify potential ATPases responsible for the ATP dependent disassembly of extruded granules, we first extruded MEG-3 labeled granules into buffers containing potent ATPase chemical inhibitors. RNA granule dynamics have been shown to be regulated by a variety of protein kinases and chaperones (Anderson and Kedersha 2002, Wippich, Bodenmiller et al. 2013, Wang, Smith et al. 2014, Alberti, Mateju et al. 2017). We found that staurosporine, a potent and general protein kinase inhibitor, and 17-AAG, a potent inhibitor of the abundant chaperone HSP90, had no effect on the ATP dependent disassembly of extruded granules compared to a vehicle only control. We conclude that kinases and HSP90 are unlikely to be the primary ATPases responsible for driving granule disassembly (Figure 2D).

It has become increasingly apparent that RNA helicases also play a role in remodeling RNA granules and regulating their dynamics (Buchan and Parker 2009, Hubstenberger, Noble et al. 2013, Hubstenberger, Cameron et al. 2015, Jain, Wheeler et al. 2016, Mugler, Hondele et al. 2016). P granules, specifically are known to contain several DEAD-box helicases including GLHs, LAF-1, and CGH-1, the *C. elegans* homologs of the VASA, DDX3, and DDX6 helicases respectively. (Updike and Strome 2010, Elbaum-Garfinkle, Kim et al. 2015). To investigate the role of these RNA helicases in the ATP-dependent disassembly of extruded granules, we first reasoned that an ATPase responsible for granule disassembly should remain stably associated with P

granules even after extrusion. We found that both GLH-1 and LAF-1 quickly diffused away from granules extruded into egg buffer. In contrast, CGH-1 remained stably associated with P granules after extrusion (Figure S1). CGH-1 (DDX6 in humans) is a well conserved RNA Helicase known to play a roll in regulating the dynamics of P bodies (PBs) in both worms and yeast (Dutta, Zheng et al. 2011, Hubstenberger, Noble et al. 2013, Hubstenberger, Cameron et al. 2015, Mugler, Hondele et al. 2016) and was identified as a stable component of stress granules in mammalian cells (Jain, Wheeler et al. 2016). Indeed the ATPase activity of the yeast homologue Dhh 1 has been shown to be required for disassembly of PBs in *S. cerevisiae* (Mugler, Hondele et al. 2016) and to maintain the dynamic state of PBs in *C. elegans* (Hubstenberger, Noble et al. 2013).

Using a temperature sensitive mutant in the ATP binding domain of CGH-1, we found that, at non-permissive temperature (25°C), *cgh-1(ts)* mutants formed large (>1μm) P granules both in the posterior cell and the anterior cell (Figure 2E, Figure S2). We also observed that *ex vivo* ATP-driven disassembly of granules was reduced in *cgh-1(ts) mutants*, consistent with a model in which the helicase activity of CGH-1 contributes to P granule disassembly (Figure 2E, Figure 2F). We also found that depletion of the CGH-1 activator, NOT1 (LET-711 in worms) by RNAi resulted in large P granules reminiscent of the *cgh-1(ts)* phenotype. We also found that, similar to our *cgh-1(ts)* mutant, depletion of LET-711 lead to a reduction in the effects of ATP driven disassembly of extruded MEG-3 granules (Figure S2).

The ATPase activity of the DDX RNA helicase CGH-1 contributes to P granule dynamics *in vivo*

To determine whether CGH-1 plays a role in P granule dynamics *in vivo*, we monitored the fluorescence recovery after photobleaching (FRAP) of the MEG-3::GFP in P granules. Embryos expressing MEG-3::GFP in either a wild-type or *cgh-1(ts)* mutant background were mounted onto agarose pads and imaged. MEG-3::GFP labeled granules were photobleached and allowed to recover for 90 seconds, imaging at 1 second time points. We found that in wild-type embryos, MEG-3 was able to recover to a similar degree as PGL-3 on a similar timescale (seconds), indicating that both the MEG-3 and PGL-3 components of P granules dynamically exchange with the cytoplasm. However, in *cgh-1(ts)* cells shifted to non-permissive temperature, MEG-3 recovery to P granules was almost entirely ablated, indicating that there was no longer exchange between the P granule and the cytoplasm and that the dynamic behavior of MEG-3 *in vivo* is dependent on CGH-1 helicase activity.

Consistent with a model in which ATP driven processes promote P granule dynamics, we were also able to show that reducing the cellular concentration of ATP by increasing the temperature of embryos to 28°C (Neves, Busso et al. 2015), caused the formation of large, non-dynamic MEG-3 granules (as determined by FRAP). As expected, these large, non-dynamic granules, unlike those seen in the *cgh-1(ts)* remained sensitive to ATP upon extrusion. Interestingly, at 28°C, we also observed PGL-3 becoming more dynamic and dissolving off of granules in vivo – consistent with its status as a liquid (Figure S2).

2.3 Discussion

There has become a growing body of evidence supporting a view of RNA granules as liquid-liquid phase separations. These conclusions are primarily based on the observation of single components of RNA granules. Here we present evidence that RNA granules, which by their nature are heterogeneous organelles composed of many different proteins, contain both liquid and non-liquid phases. RNA granules are dynamic however and here we present evidence that, while the liquid components of granules may be passively dynamic, the dynamics of the non-liquid components are driven by ATP dependent processes. Our findings support a model in which P granules contain a non-liquid MEG-3 scaffold whose dynamics are driven, at least in part, by the DDX RNA helicase CGH-1.

MEG-3 is a stable granule component whose disassembly is driven by ATP

We found that MEG-3 is retained on P granules extruded into a dilute environment. This is not a conventional liquid behavior as conventional liquids retain a dynamic equilibrium with the surrounding soluble pool and would be expected to dissolve in a dilute environment (like the PGLs). Additionally, we found that stable MEG-3 granules were resistant to a high salt environment (1M NaCl). Transient electrostatic interactions are hypothesized to drive liquid-liquid phase separation and this resistance to high salt conditions is consistent with a non-liquid phase.

We found both that disassembly from the extruded granule was driven by addition of ATP and that cellular availability of ATP contributes to granule dynamics *in vivo*. Although ATP has been shown to have chemical properties that lead to dissolution of phase separations, our data is not consistent with ATP acting as a hydrotrope. Neither

ADPnP nor GTP showed any effect on extruded MEG-3 granules and ATP chelated of its Mg^{2+} by EDTA also showed little effect. While ADPnP and GTP are both equally effective hydrotropes to ATP and the coordination of ATP's phosphates by Mg^{2+} ions is not essential to its role as a hydrotrope, all of these species would be useless to an ATPase. These pieces of evidence point to ATP being used as an energy source.

One attractive aspect of the theory that ATP in the millimolar range acts as a hydrotrope is that it potentially explains the very high cellular concentration of ATP. Presumably, ATP would need to be maintained at such a high concentration in order to prevent spontaneous and aberrant phase separation in the very protenacious cell. We also find that ATP seems to only drive granule disassembly in this millimolar range (>3-5 mM). However, this requirement for a high concentration of ATP is consistent with the low affinity of many helicases (Linder and Jankowsky 2011, Gao, Putnam et al. 2016).

ATPase activity of the DDX RNA helicase CGH-1 drives disassembly and dynamics of MEG-3 granules

Here we, identify CGH-1 as a critical ATPase that stays stably associated with extruded granules and drives their disassembly in an environment containing millimolar levels of ATP. Furthermore, we were able to show that loss of the CGH-1 activator, NOT1, presented similar phenotypes as our *cgh-1(ts)* mutant. Not1 has been shown to be essential for activity of Dhh1 – the yeast homologue of CGH-1, and this result is consistent with a model in which the CGH-1/DDX6 RNA helicase drives granule dynamics. NOT1 is also a subunit of the CCR4 deadenylation complex responsible for turning over mRNA in the cell, and it has previously been shown that depletion of NOT1/LET-711 leads to an increase in the abundance of mRNA which drives P granule

assembly (Gallo, Munro et al. 2008, Smith, Calidas et al. 2016). It is unclear which of these effects is the predominant cause of the large P granule phenotype we see in *let-711* RNAi, but the reduced sensitivity to ATP indicates that NOT1/LET-711 plays a roll in the activation of ATPases responsible for granule disassembly.

To explain all of these findings, we propose a model in which P granules are composed of both liquid and non-liquid components. We propose that MEG-3 is an essential P granule scaffold and a non-liquid component of granules while non-essential client proteins such as PGL-1/3 and the GLHs comprise the liquid phase. We also suggest that, while the liquid and non-liquid components of the granules share similar dynamics as evidenced by their similar recovery in our FRAP experiments, the dynamics of the non-liquid component are the result of remodeling by ATP-dependent enzymes including the DDX RNA-helicase CGH-1.

2.4 Experimental Procedures

Chemicals Used – Adenosine 5'-triphosphate disodium salt hydrate – ATP (A2383, Sigma), Adenosine 5'-diphosphate sodium salt - ADP (A2754, Sigma), Adenosine 5'-monophosphate disodium - AMP (01930, Sigma), Adenosine 5'-(β,γ-imido)triphosphate lithium salt hydrate – ADPnP (A2647, Sigma), Guanosine 5'-triphosphate sodium salt – GTP (G8877, Sigma), Magnesium Chloride – $MgCl_2$ (M8266, Sigma), Ethylenediaminetetraacetic acid disodium salt dihydrate – EDTA (ED2SS, Sigma), Sodium Chloride – NaCl (S9888, Sigma), 1, 6 Hexanediol (240117, Sigma), 2, 5 Hexanediol (H11904, Sigma), Sodium dodecyl sulfate – SDS (L3771, Sigma), Dimethyl sulfoxide – DMSO (276855, Sigma), Staurosporine (A8192, ApexBio), 17-AAG (KOS953) (A4054, ApexBio), RNAse T1 (1101017, Ambion).

Preparation of ATP analogue Extrusion Buffers – All ATP analogue stock solutions were prepared in egg buffer (59 mM NaCl, 24 mM KCl, 1mM $CaCl_2$, 5mM $MgCl_2$, 13 mM Hepes pH 7.3)

Confocal Microscopy - Fluorescence microscopy was performed using a Zeiss Axio Imager with a Yokogawa spinning-disc confocal scanner. Images were taken using Slidebook v 6.0 software (Intelligent Imaging Innovations). For live imaging of extruded granules, embryos were dissected from adult hermaphrodites in egg buffer salt solution (59 mM NaCl, 24 mM KCl, 1mM $CaCl_2$, 5mM $MgCl_2$, 13 mM Hepes pH 7.3) or egg buffer containing indicated additive and mounted glass slides. P granules were extruded by ablating the eggshell using a 3i Ablate!^{TM} laser system at 532 nm pulse setting with a power level of 155 and 10 cycles. All embryo images are z stack maximum projections using a z step size of 1 μm, spanning the entire width of the embryo. Images were

required using 25 ms exposures in the 488 channel or 50 ms exposures in the 561 channel continuously for 2 minutes at 63x objective.

Quantification of MEG-3::GFP granule disassembly after extrusion from confocal images - Time-lapse images were acquired as explained above and z stack max projections were quantified using Image J64. To recognize granules, background was subtracted from each image using a rolling ball radius of 15 pixels, a pixel brightness threshold was set to 31-255. Remaining pixels were smoothed 1 times and size and number of objects was quantified. Average size of granules was calculated for each time point indicated and used to calculate the ratio of granule size compared to pre-extrusion. Granules present prior to extrusion but completely disassembled after extrusion were quantified as a size of zero.

Fluorescence Recovery after Photobleaching (FRAP) - All FRAP imaging was preformed using a Zeiss LSM 800 GaAsp system. Embryos were dissected from adult hermaphrodites in M9 salt solution and mounted onto 3% agarose on glass slides. Experiments were performed by imaging at 5% laser power in the 488 or 561 channels with a gain of 700 and bleaching was performed using an area slightly larger than the granules (~2.5 μM) using 50% laser power in the 488 and 561 channels (for GFP and RFP respectively). Single slice images were taken every second during a recovery phase of >90 seconds. The mean fluorescence intensity of the area containing the granule was measured at each time point using ImageJ/Fiji. Each time point was normalized to the initial granule fluorescence and the normalized fluorescence recovery was averaged for each time point across granules. Average fluorescence intensity was plotted with ± standard deviation error bars.

Crossing of cgh-1(ts) mutant with MEG-3::GFP strain – Young male *cgh-1(ts)* (DG1701, Table S1) worms were mated with L4 stage hermaphrodite worms expressing MEG-3::GFP. Worms were mated by placing them on a mound of OP50 bacteria at a ratio of 3 males for each L4 hermaphrodite. Worms were moved to a new mound of bacteria every 24 hours for 3 days. F1 Cross progeny were allowed to grow to adulthood and were singled out to lay embryos. F2 progeny were then singled out, allowed to lay embryos, and screened for MEG-3::GFP expression. The progeny from MEG-3::GFP positive F2 hermaphrodites were screened for homozygous MEG-3::GFP expression and for the *cgh-1(ts)* mutation by PCR and sequencing. Two independent lines were obtained using this method (Table S1).

Temperature shifts for cgh-1(ts) mutant – Young adult worms were shifted to agar plates containing OP50 bacteria that had been pre-incubated at 25.8°C. Worms were then incubated at this temperature for 90 minutes using a UVP HB-1000 Hybridizer hybridization incubator. After incubation, embryos were dissected from adults and mounted as explained above.

RNA mediated Interference (RNAi) - RNAi knock-down experiments were performed by feeding on HT115 bacteria (Timmons and Fire 1998). Feeding constructs were obtained from the Ahringer or Openbiosystems libraries and transformed into HT115 bacteria. pL4440 was used as a negative control empty feeding vector. Bacteria were grown at 37°C in LB + ampicillin (100 µg/mL) for 5 hours, induced with 5 mM IPTG for 45 minutes, plated on NNGM (nematode nutritional growth media) + ampicillin (100 µg/mL) + IPTG (1 mM), and grown overnight at room temperature. Embryos isolated by bleaching from gravid hermaphrodites were added to the RNAi plates and

transferred to fresh plates as L4 larvae before examination of their progeny. All RNAi experiments were performed at 20^{o}C.

2.5 Figures

Figure 1 – Stability of extruded MEG-3 granules

A. Fluorescent images of live wild-type embryos expressing MEG-3::GFP and PGL-3::RFP before (left) and after (right) extrusion of P granules. In this and subsequent figures, embryos are oriented with anterior to the left and posterior to the right. Scale bar in bottom right corner is 10 μM long.

B. Quantification of MEG-3 granule dissolution in various extrusion buffers. Dissolution of MEG-3 granules was quantified using granules extruded from MEG-3::GFP expressing embryos as shown in Fig 1A. Dissolution was determined as the ratio of the mean size of granules in an embryo 60 seconds after extrusion to the mean size of granules in an embryo immediately before extrusion (Size After/ Size Before). Each circle in graph represents the ratio of average granule size for a single embryo. Means are indicated along with error bars representing ± SD. X – axis shows the buffer conditions for each group. Decreasing ratios of average granule size reflect increased granule dissolution in indicated buffer.

Figure 2 – ATP drives active MEG-3 granule disassembly

A. Fluorescent images of live wild-type embryos expressing MEG-3::GFP before (left) and after (right) extrusion of P granules into egg buffer (top) or egg buffer containing 5 mM ATP*Mg (bottom). Scale bar is 10 μM long

B. MEG-3 Granule disassembly over time. Fluorescent time-lapse images of wild-type granules labeled with MEG-3::GFP after extrusion into egg buffer (top) or 5 mM ATP*Mg (bottom). Time after extrusion is shown below each image. MEG-3 granules shown are from different images than those presented in Fig 2A. Scale bar is 1 μM long.

C. Quantification of MEG-3 granule disassembly over time at varying concentrations of ATP*Mg. Disassembly of MEG-3 granules was quantified as in Fig 1B using time points immediately before granule extrusion (0s) and then 5 seconds, 60 seconds, and 120 seconds after granule extrusion. Granule disassembly over time was measured in conditions of 0 - 5 mM ATP*Mg in 1 mM increments. X – axis shows time after extrusion in seconds. Each circle represents the mean ratio of average granule size for at least 4 embryos. Error bars represent ± SEM.

D. Quantification of MEG-3 granule disassembly in extrusion buffers containing various ATP analogues and ATPase inhibitors. Disassembly of MEG-3 granules was quantified and represented as in Fig 1B. As in Fig 1B, error bars represent ± SD. X – axis shows the buffer conditions for each group.

E. Fluorescent images of live wild-type (top) and *cgh-1(ts)* mutants (bottom) after shifting to non-permissive temperature. Embryos expressing MEG-3::GFP before (left) and after (right) extrusion of P granules (as in Fig 2A). Scale bar is 10 μM long.

F. Quantification of MEG-3 granule disassembly in wild-type and *cgh-1(ts)* mutants at non-permissive temperatures. Disassembly of MEG-3 granules was quantified and represented as in Fig 1B. Error bars represent ± SD. X – axis indicates the genotype and buffer conditions for each group.

Figure 3 – MEG-3 granule dynamics depend on CGH-1 *in vivo*

A. Fluorescent images of live wild-type embryos expressing MEG-3::GFP before (left) 0 seconds after (middle) and 90 seconds after (right) photobleaching of MEG-3::GFP labeled P granule. Dotted circle indicates location of bleaching and area quantified for recovery. Scale bar is 10 μM long.

B. Enlarged fluorescent images of P granules before (left), 0 seconds after (middle) and 90 seconds after (right) photobleaching. Granules are shown from wild-type embryos co-expressing MEG-3::GFP and PGL-3::RFP (first and second row respectively) at 20°C and from embryos expressing MEG-3::GFP in wild-type and *cgh-1(ts)* mutant backgrounds at non-permissive temperature (third and fourth row respectively). Scale bar is 1 μM long.

C. P granule fluorescence recovery over time. Graph shows quantification of recovery curves for MEG-3::GFP (blue) and PGL-3::RFP (red). Data points are acquired at 1 second intervals starting five seconds before bleaching until 90 seconds after bleaching. Values are calculated as mean granule fluorescence intensity at each time point normalized to initial fluorescence intensity (t = -5 seconds) and plotted as an average of at least 7 granules. Error bars represent mean ± SD.

D. MEG-3 granule fluorescence recovery over time in wild-type (green) and *cgh-1(ts)* mutant background (purple) at non-permissive temperature. Graph shows recovery curves as in Fig 3C. Error bars represent mean ± SD.

Figure S1 – P granule extrusion with various granule markers

A. Fluorescent images of live wild-type embryos expressing (top to bottom) PGL-1::eGFP, GLH-1::RFP, LAF-1::GFP, and CGH-1::GFP before (left) and 60 seconds after (right) extrusion of P granules. Dotted outline indicates cell boundary before and after extrusion. Scale bar is 10 μM long.

Figure S2 – Effects of *let-711* RNAi and ATP depletion by 28°C temperature shift

A. Fluorescent images of live wild-type embryos shifted to 28°C expressing MEG-3::GFP before (left) 0 seconds after (middle) and 90 seconds after (right) photobleaching of MEG-3::GFP labeled P granule. Dotted circle indicates location of bleaching and area quantified for recovery. Scale bar is 10 μM long. Insets depict enlarged fluorescent images of region of interest. Inset scale bar is 1 μM long.

B. Fluorescent images of live wild-type embryos expressing MEG-3::GFP before (left) and 60 seconds after (right) extrusion of P granules in (top to bottom) a wild-type background at 20°C, a wild-type background at 28°C, and in worms treated with *let-711* RNAi. All were extruded into egg buffer containing 5 mM ATP*Mg. Scale bar is 10 μM long.

C. Fluorescent images of live wild-type embryos co-expressing MEG-3::GFP (left) and PGL-3::RFP (right) at 20°C (top) and 28°C (bottom). Scale bar is 10 μM long.

Table S1 – Strains used in this study

All strains used in this study. Independently obtained lines displayed the same phenotypes.

A

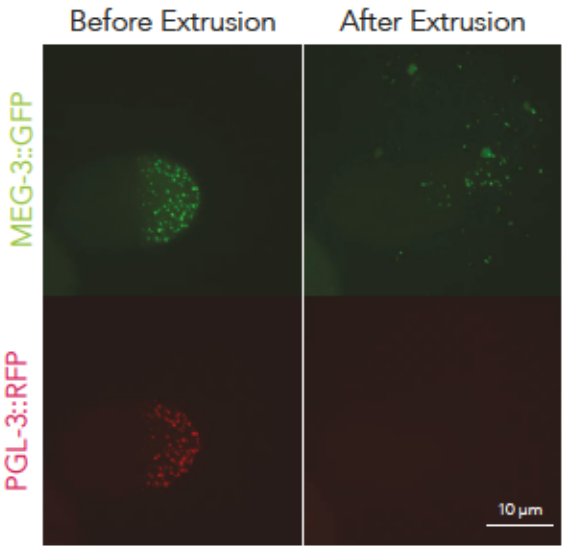
Before Extrusion
After Extrusion
MEG-3::GFP
PGL-3::RFP
10 µm

B

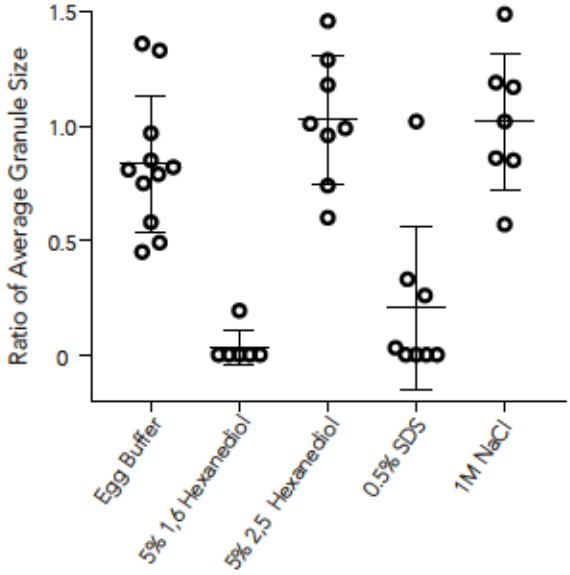
Ratio of Average Granule Size
1.5
1.0
0.5
0
Egg Buffer
5% 1,6 Hexanediol
5% 2,5 Hexanediol
0.5% SDS
1M NaCl

Figure 1

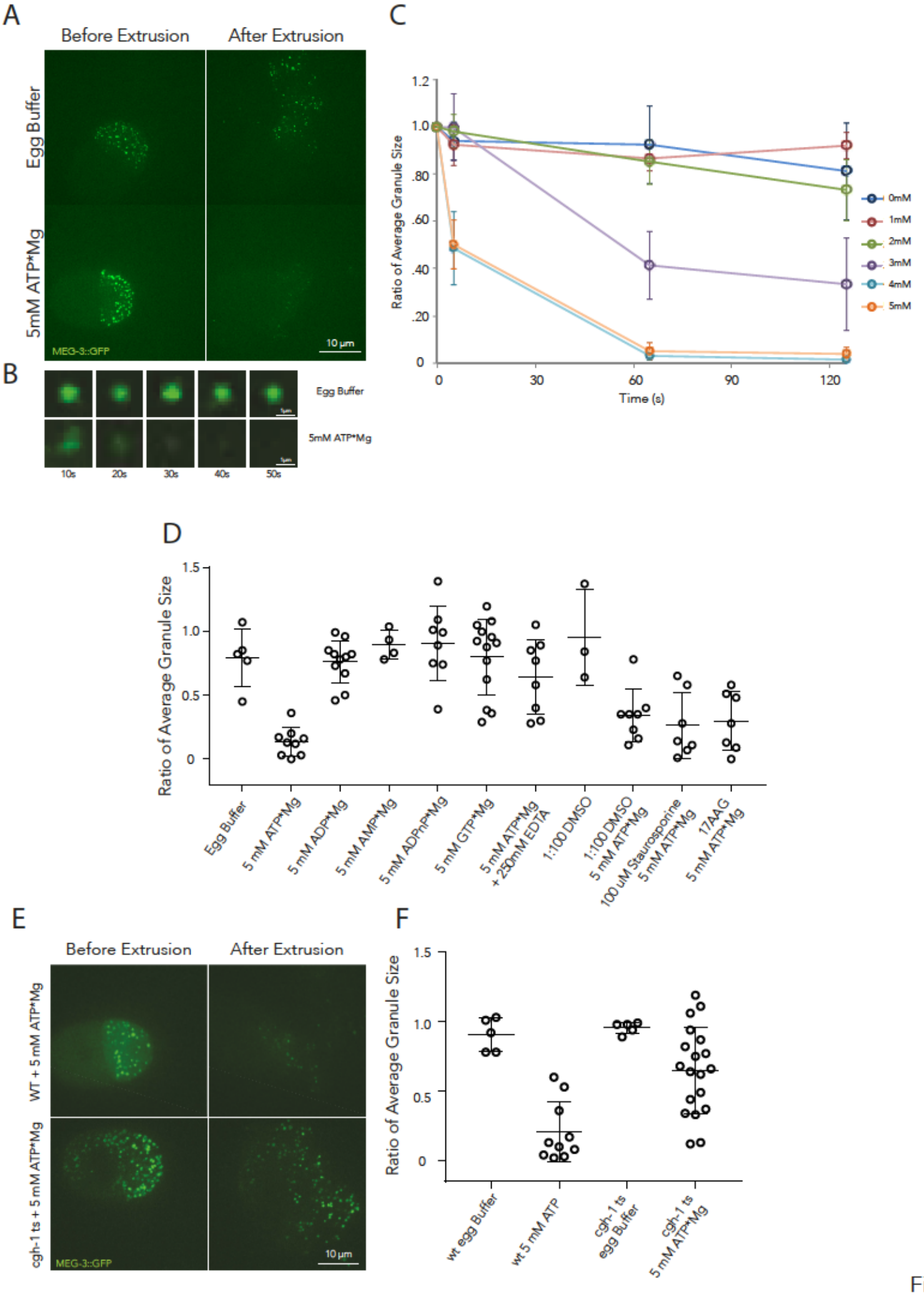
A
Before Extrusion
After Extrusion
Egg Buffer
5mM ATP*Mg
MEG-3::GFP
10 µm
B
Egg Buffer
5mM ATP*Mg
10s
20s
30s
40s
50s
C
Ratio of Average Granule Size
Time (s)
0mM
1mM
2mM
3mM
4mM
5mM
D
Ratio of Average Granule Size
Egg Buffer
5 mM ATP*Mg
5 mM ADP*Mg
5 mM AMP*Mg
5 mM ADPnP*Mg
5 mM GTP*Mg
5 mM ATP*Mg + 250mM EDTA
1:100 DMSO
1:100 DMSO 5 mM ATP*Mg
100 uM Staurosporine 5 mM ATP*Mg
17AAG 5 mM ATP*Mg
E
Before Extrusion
After Extrusion
WT + 5 mM ATP*Mg
cgh-1 ts + 5 mM ATP*Mg
MEG-3::GFP
10 µm
F
Ratio of Average Granule Size
wt egg Buffer
wt 5 mM ATP
cgh-1 ts egg Buffer
cgh-1 ts 5 mM ATP*Mg

Figure 2

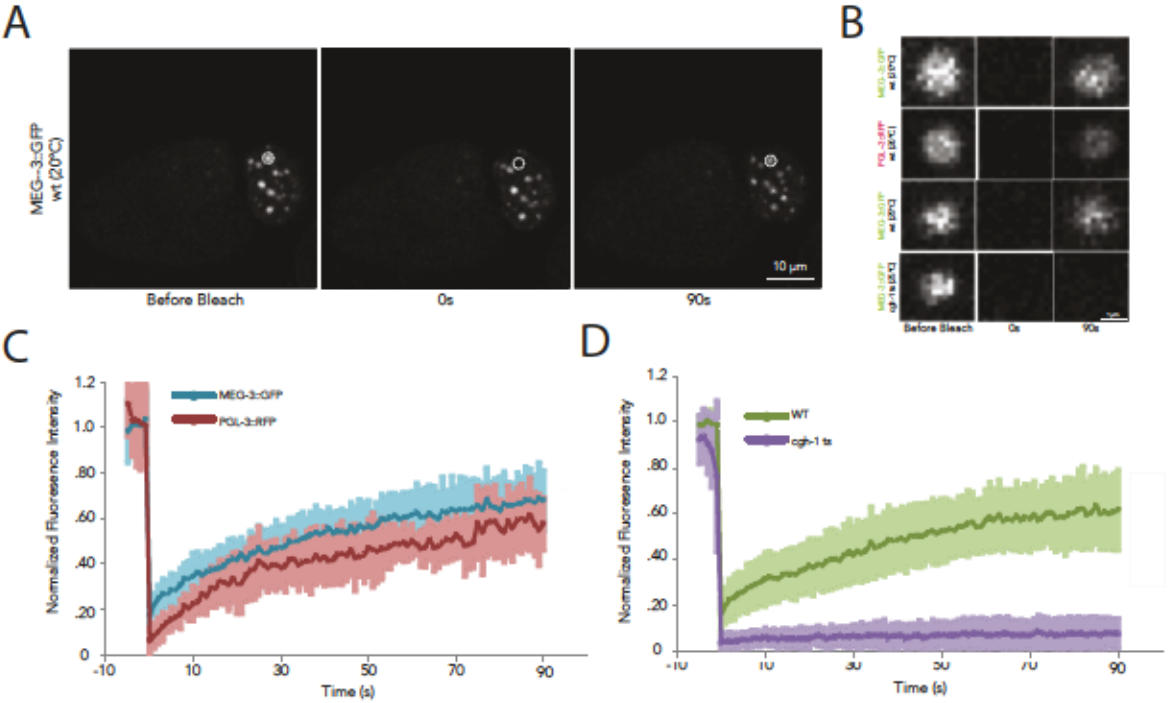
A
MEG-3::GFP
wt (20°C)
Before Bleach
0s
90s
10 µm
B
Before Bleach
0s
90s
C
MEG-3::GFP
POL-3::RFP
Normalized Fluorescence Intensity
Time (s)
D
WT
cgh-1 ts
Normalized Fluorescence Intensity
Time (s)

Figure 3

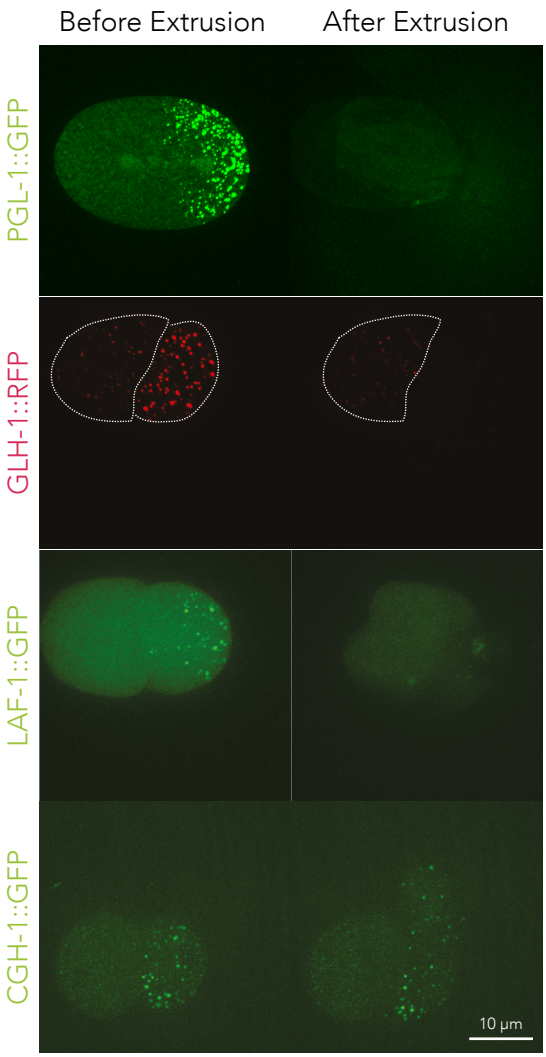
Before Extrusion
After Extrusion
PGL-1::GFP
GLH-1::RFP
LAF-1::GFP
CGH-1::GFP
10 µm

Figure S1

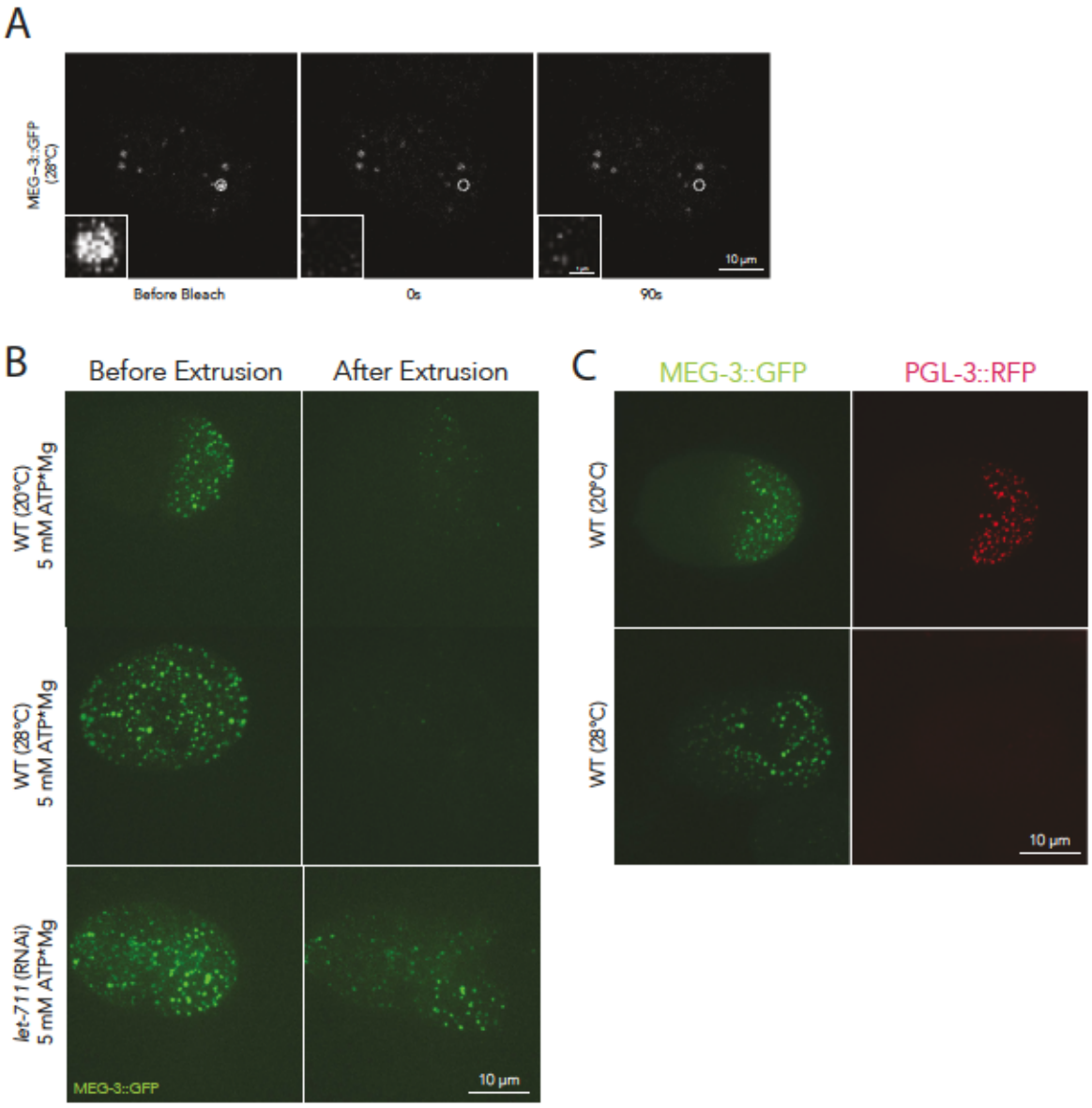
A
MEG-3::GFP (28°C)
Before Bleach
0s
90s
10 µm
B
Before Extrusion
After Extrusion
WT (20°C) 5 mM ATP*Mg
WT (28°C) 5 mM ATP*Mg
let-711 (RNAi) 5 mM ATP*Mg
MEG-3::GFP
10 µm
C
MEG-3::GFP
PGL-3::RFP
WT (20°C)
WT (28°C)
10 µm

Figure S2

Strain	Genotype	Description	Method	Derived from	Citation
JH3503	*meg-3(ax3054)*	MEG-3::meGFP	CRISPR/Cas9	N2	Smith, Calidas et al. 2016
DG1701	*cgh-1(tn691)*	cgh-1 ts	EMS	N2	Yamamoto et al. 2005
JH3544	*meg-3(ax3054); cgh-1(tn691)*	MEG-3::meGFP; *cgh-1 ts*	Cross	JH3503[meg-3(ax3054)] xDG1701[cgh-1(tn691)]	Created for this study
JH3546	*meg-3(ax3054); cgh-1(tn691)*	MEG-3::meGFP; cgh-1 ts	Cross	JH3503[meg-3(ax3054)] xDG1701[cgh-1(tn691)]	Created for this study
JH3019	*meg-3(ax3054); pgl-3(axIS2077)*	MEG-3::meGFP; mCherry::PGL-3	Cross	JH3503[meg-3(ax3054)] xJH2906(pgl-3(axIS2077))	Unpublished
JH4007	*glh-1(ax3009)*	GLH-1::tagRFP	CRISPR/Cas9	N2	Paix et al. 2015
JH1985	*cgh-1(axIs1436)*	CGH-1::GFP	transgene	N2	Unpublished
CPB132	*laf-1(ptnIs077)*	LAF-1::GFP	CRISPR/Cas9	N2	Wei, Elbaum-Garfinkle et al. 2017
JH3269	*pgl-1(x)*	PGL-1::eGFP	CRISPR/Cas9	N2	Unpublished

Table S1

Chapter 3

Conclusions and Final Thoughts

3.1 Summary

In this thesis we show that P granules consist of both a non-liquid and a liquid phase. We show that the liquid phase is comprised of proteins including but not limited to the PGLs, GLHs, and the DDX3 homologue LAF-1. We show that the non-liquid phase contains the intrinsically disordered protein MEG-3. We provide evidence to show that MEG-3 is an intrinsically disordered protein that is capable of binding RNA with nanomolar affinity. We go on to provide evidence both *in vivo* and *in vitro* that binding to RNA enhances MEG-3's ability to phase separate. Finally we provide evidence supporting two mechanisms by which MEG-3's interaction with RNA is manipulated to regulate granule phase separation and dynamics. We show *ex vivo* and *in vivo* that the ATPase activity of the DDX6 RNA helicase homologue – CGH-1 is required to maintain the dynamic nature of these non-liquid MEG-3 granule cores. Additionally, we provide *in vitro* and *in vivo* evidence that the competing RNA binding protein – MEX-5 is necessary and sufficient sequester available mRNA from MEG-3, thus inhibiting its phase separation.

There are several questions that remain concerning the coordination of these methods of regulation and how they fit in to the overall scheme of regulating P granule dynamics. This chapter serves as a discussion of those questions and a contemplation of the best ways to go about addressing them.

1. What regulates the timing of P granule disassembly in the early embryo?
2. What determines whether a P granule component belongs to the liquid or non-liquid phase?
3. Do other ATPases contribute to regulating P granule dynamics?

3.2 What regulates the timing of P granule disassembly in the early embryo?

We found that MEX-5 was sufficient to inhibit the enhanced phase separation of MEG-3 *in vitro*. We also were able to show that MEX-5 ectopically localized to the posterior of the *C. elegans* zygote was sufficient to drive P granule disassembly *in vivo*. There is an interesting discrepancy between these two results in that MEX-5 is not sufficient to reverse MEG-3 phase separation *in vitro*. This indicates that *in vivo*, there exist some permissive factor(s) that allows MEX-5 to drive P granule disassembly in the anterior.

Another interesting point is that in our *mex-5 S404a* mutant, MEX-5 S404A is spread evenly across the cytoplasm as expected and this leads to the ectopic disassembly of P granules in the posterior. However, MEX-5 has this same localization prior to the polarization of the *C. elegans* zygote and at this time MEX-5 is not sufficient to disassemble granules in the anterior or posterior. What controls the "activation" of MEX-5 or permits MEX-5 to steal RNA from MEG-3? It is possible that these permissive factors allow the cell to regulate the timing of P granule disassembly.

There are several interesting candidates for regulators of MEX-5 activity that could be permissive factors for P granule disassembly. MEX-5 is known to be phosphorylated by two kinases – PAR-1, the ser/thr kinase known to phosphorylate MEX-5 primarily at its S404 residue (Griffin, Odde et al. 2011), and PLK-1, the polo-like kinase known to phosphorylate MEX-5 at its T186 residue (Nishi, Rogers et al. 2008). Both of these phosphorylation events are potential mechanisms of regulating either MEX-5 RNA binding activity directly or MEX-5's ability to access the RNA in a

P granule. Preliminary work from both our and Erik Griffin's labs have shown that the T186 phosphorylation site of MEX-5 is required to polarize P granules.

Alternatively, it is possible that the permissive factors that allow MEX-5 to antagonize P granule assembly *in vivo* do not act on MEX-5 but on some substrate of the P granule. One interesting possibility is that the dynamic nature of the non-liquid P granule core is regulated temporally and that only when the core is dynamic is MEX-5 allowed access to its RNA. In such a model, the activity of helicases like CGH-1 would need to be regulated temporally, possibly by post-translational modification or possibly by availability of ATP. However, because CGH-1 is a critical component of several essential cellular processes and ATP is required to power many energy dependent processes in the cell, it is difficult to imagine that either could be globally modified to regulate P granule localization even for a short time.

3.3 What determines whether a P granule component belongs to the liquid or non-liquid phase?

The properties of MEG-3 that drive its non-liquid phase separation are unclear. MEG-3 contains an intrinsically disordered region (IDR). These regions have been shown to undergo non-liquid phase separations into hydrogels (Kato, Han et al. 2012). However, LAF-1 also contains an IDR (Elbaum-Garfinkle, Kim et al. 2015) and yet it does not persist on P granules when extruded. Furthermore, CGH-1, does not contain any IDRs and persists on extruded granules (Figure S1). This means that presence of an IDR is neither necessary nor sufficient to join the non-liquid phase of P granules. Closer study and a more comprehensive list of P granule proteins that are stably associated with extruded granules will be needed to determine their common traits. One exciting method

of building this list made possible by this research is the purification of stable P granule cores . It will be interesting to purify and analyze these stable cores to determine their components. The Parker lab has made similar discoveries using mammalian and yeast stress granules and it would be fascinating to make comparisons between the proteome and transcriptome of *C. elegans* P granules and stress granules. There are numerous lines of inquiry that could come from this. What proteins occupy P granule cores? What RNA, if any, occupies P granule cores? Does the composition of these cores change over the course of the cell cycle or the embryonic stage from which they are isolated? Are different components of the granules regulated by different ATPases? These will all be interesting questions for future lab members to pursue.

3.4 Do other ATPases contribute to regulating P granules?

CGH-1 and its homologues (DDX6 in humans and Dhh1 in yeast) have been identified as components and regulators of RNA granules and their dynamics (Hubstenberger, Noble et al. 2013, Hubstenberger, Cameron et al. 2015, Jain, Wheeler et al. 2016, Mugler, Hondele et al. 2016). While Dhh1 ATPase activity has been shown to regulate its own dynamics in yeast P-bodies (Mugler, Hondele et al. 2016), here we were able to show that CGH-1 regulates the dynamics of a separate P granule protein – MEG-3. Similar results have been seen in P-bodies in *C. elegans* where CGH-1 activity contributes to the dynamics of another PB protein – CAR-1 (Hubstenberger, Noble et al. 2013). However, in the case of P granules, we have shown that CGH-1 regulates the dynamics of a critical scaffolding unit of P granules – exposing the possibility that CGH-1 plays a role in regulating global granule dynamics.

While we do not know the mechanism by which CGH-1/DDX-6 drives granule disassembly, we do know that the association of MEG-3 with RNA drives granule formation (Smith, Calidas et al. 2016). It is therefor, reasonable to envision a model in which CGH-1/DDX6 drives granule dynamics by allowing the constant breaking and reforming of bonds between RNA binding proteins like MEG-3 and their associated RNAs. This breaking and reforming of bonds is a hallmark of LLPS and may lead to the liquid-like dynamic behavior we see in MEG-3. If this is the role that CGH-1/DDX6 plays, it is also reasonable, if not expected, that other RNA helicases would contribute to granule dynamics similarly. In addition to CGH-1, numerous other helicases occupy granules *in vivo*. In our study, we focused on CGH-1/DDX6 because it remained stably associated with extruded granules and thus was a candidate ATPase for the *ex vivo* ATP dependent granule disassembly that we observed. However, LAF-1 (DDX3 in humans), and the GLHs (VASA homologues) are also known RNA helicases involved in regulating P granules. Although they did not stay stably associated with extruded granules, it is very possible that they contribute to granule dynamics when associated *in vivo*. Future mutagenesis combined with FRAP analysis will be an excellent way to determine which other ATPases are involved in regulating granule dynamics.

3.5 Final thoughts

One of the ultimate goals of this research and research like it is to build a thorough understanding of how these phase separated compartments form and remain dynamic. This will allow us to draw parallels between different classes of RNA granules as well as parallels between RNA granules and other membraneless organelles. For example, active, energy dependent remodeling has been proposed as a mechanism for

maintaining the dynamic nature both of stress granules and the nucleolus (Brangwynne, Mitchison et al. 2011, Jain, Wheeler et al. 2016). Beyond that, a greater understanding of the key conserved players and principles regulating phase separation *in vivo* promises a greater understanding of phase separation as it pertains to disease.

Many neurodegenerative disorders present with pathogenic aggregates – the consequence of aberrant phase separation in the cell. We may find that the RNA competition model of regulation that we present here for P granules also regulates phase separation in other systems. It will be interesting to find whether RNA binding proteins like MEX-5 or intrinsically disordered proteins like MEG-3 play a role in disease – potentially due to aberrations in a similar system of regulation. Indeed, the intrinsically disordered domain containing RNA-binding protein FUS is associated with the neurodegenerative disorder ALS and patient-derived mutations in FUS have been linked to ALS (Patel, Lee et al. 2015). Furthermore, it has been noted that many of these neurodegenerative disorders are associated with age and occur in an ATP deprived environment (Rice and Rosen 2017). One explanation for the formation of these pathogenic phase separations that is consistent with the model we propose here is that the loss of ATP associated with age leads to decreased function of the ATP dependent machinery keeping these phase separations dynamic and healthy. It is possible that, *in vivo*, an abundance of ATP is required to drive the machinery that keeps these phase separations in check. Indeed, IDRs, like those contained within MEG-3 have been shown to mature into amyloid like fibers *in vitro* and *in vivo* (Kato, Han et al. 2012, Xiang, Kato et al. 2015). We may find that it is not the specific players that are conserved between organisms, organelles, or diseases. However the roles that they play may be conserved.

Identification – both of these players and these roles should be the focus of future research.

Chapter A

Interactors of the Serine/Threonine Kinase PAR-1

A.1 Summary

One of my previous aims was focused on determining the roles of PAR-1, a serine threonine kinase in polarity establishment and maintenance in the C.elegans early embryo. To do this, we attempted to determine PAR-1 c-terminal interactors and their role in PAR-1 localization and function using a combination of CO-IP, mass spectrometry, and RNAi. Here we show that the highly conserved C-terminal domain of PAR-1 CO-IPs with the coiled-coil domain containing protein SPD-5. We go on to show that SPD-5 is required for proper localization of PAR-1 to centrosomes, but not to the posterior cortex. The uncoupling of these two localizations, which are both dependent on the PAR-1 c-terminus may be key in determining what roll, if any, PAR-1 plays on the centrosome.

A.2 Results

The Conserved PAR-1 C-terminal domain Co-immunopercipitates with the Coiled-Coil domain containing protein – SPD-5

PAR-1 is a ser/thr kinase necessary for polarity maintenance in the early *C. elegans* embryo. During the initial polarization of the embryo, PAR is asymmetrically localized to the posterior cortex of the zygote before the first division and to the cortex of the germline destined cells (p-cells) in later divisions (Figure 1C, Figure 1D) (Guo and Kemphues 1995). PAR-1 contains an N-terminal kinase domain and a highly conserved anionic lipid binding Kinase Associated domain (KA1) in its c-terminus (Figure 1A) (Moravcevic, Mendrola et al. 2010). Although the E3 RING domain containing PAR-2 protein is known to be necessary for PAR-1 localization to the cortex (Motegi, Zonies et al. 2011), we have also observed that PAR-1 localizes to the centrosomes and mitotic

spindle (Figure 1C, Figure 1D). The regulation of PAR-1 localization is not fully understood. Furthermore, because the conserved c-terminal domain of PAR-1 (PAR-1 (CT)), is necessary and sufficient to localize to both the posterior cortex and the centrosomes, PAR-1's roles in these two locations have yet to be uncoupled.

In order to identify other regulators of PAR-1, we performed a CO-IP of a GFP tagged PAR-1 c-terminal truncation. In parallel we performed the same CO-IP on a strain expressing cytoplasmic GFP to determine which proteins interacted with the GFP tag and not PAR-1. We completed 3 replicates of PAR-1 (CT) and GFP CO-IPs. When compared to GFP alone we found 44 proteins that CO-IPed with GFP:PAR-1 CT specifically (defined as being identified in 2 or more of the 3 PAR-1 (CT) CO-IPs and no more than 1 GFP alone CO-IP) (Figure 1B).

In order to determine which of these interactors played a role in regulating PAR-1 localization or PAR-1 function we performed a secondary RNAi screen. To assess the effect on PAR-1 localization, we monitored PAR-1 (CT)::GFP in embryos of worms fed bacteria expressing double stranded RNA targeting the gene of interest. PAR-1 kinase activity is known to be required for proper P granule formation and localization (Griffin, Odde et al. 2011, Smith, Calidas et al. 2016). Therefor, in order to determine if the gene of interest played a role in regulating PAR-1 function independent of its localization, we monitored the P granule marker PGL-1::GFP. This secondary screen showed that many of these genes either had no phenotype, or gross phenotypes in cell division or morphology, but not to PAR-1 localization or function specifically.

One gene found through CO-IP mass spec, *spd-5*, showed a PAR-1 specific phenotype of losing PAR-1 localization to the centrosomes while maintaining PAR-1

localization on the posterior cortex. Additionally, we found that *spd-5* RNAi resulted in P granules that were not properly localized to the posterior cortex but instead appeared stuck in the middle of the cell (Figure 1C).

Gamma tubulin is required for proper localization of PAR-1 to centrosomes

The *spd-5* locus codes for a coiled-coil domain containing protein that sits at the top of the hierarchy of centrosomal development and is responsible for localizing many proteins that are part of the pericentriolar material (PCM) such as PP2A phosphatase subdomains, AIR-1 aurora like kinase, and gamma tubulin (Hannak, Kirkham et al. 2001). Because spd-5 is responsible for the localization of many proteins to the PCM, it is possible that one of these downstream PCM components is more directly responsible for PAR-1 localization to the centrosome.

To check this, we knocked down each of the genes whose protein products are known to localize to the centrosome in a *spd-5* dependent manner. Of the seven genes examined, two resulted in a significantly decreased levels or completely ablated levels of PAR-1 (CT)::GFP localized to the centrosome. These genes were *air-1* kinase and gamma tubulin (Figure 1D).

A.3 Discussion

Here we identified SPD-5 as a potential interactor with the PAR-1 c-terminal domain and showed that depletion of SPD-5 as well as a number of the proteins that SPD-5 recruits to the centrosome results in loss of PAR-1 off of the centrosome. Because AIR-1 kinase is also known to be required for normal gamma tubulin recruitment to the centrosome, it is likely that gamma tubulin is the most downstream of these genes required for PAR-1 localization to the centrosome. The phenotype of specifically lacking

PAR-1 on the centrosome is an intriguing one. Because the same domain that is necessary and sufficient to localize PAR-1 to the centrosome is also necessary and sufficient to localize it to the posterior cortex, using mutagenesis of the PAR-1 locus to determine which phenotypes, if any, are caused by loss of PAR-1 from the centrosome have so far been fruitless. The identification of a genetic pathway specifically required to localize PAR-1 to the centrosome exposes the possibility of identifying PAR-1s function on the centrosome. However, because all of the genes that we know are required to localize PAR-1 specifically to centrosome (SPD-5, AIR-1, and Gamma tubulin) are required for additional cellular processes including cell division, it is difficult to determine which cellular phenotypes are a result of loss of PAR-1 on the centrosome or a direct result of the depletion of the RNAi target. One possible solution to this is to determine whether PAR-1 interacts directly with any of these proteins and determine the residues on PAR-1 necessary for that interaction. If the same residues are not required for PAR-1 localization to the posterior cortex, we may be able to tease apart which phenotypes, if any, are caused by loss of PAR-1 on the centrosome. Additionally, there are a number of feasible optogenetic solutions to this problem of removing PAR-1 and only PAR-1 specifically from the centrosome. However, We have not been able to find one that can cause localized protein turn over on the necessary time scale (seconds or minutes). Because of these technical limitations at the time of taking on this project, we decided to pursue other questions. However, with the advent of CRISPR, it is possible that this question is much more tractable now. It will be interesting to see whether future lab members are able to determine PAR-1's role on the centrosome.

A.4 Experimental Procedures

Worm lysis and GFP IP for Mass Spec Preparation – Mothers were bleached to isolate embryos. Harvested embryos were snap frozen and stored at -80C. Embryos pellets were then ground into powder in liquid nitrogen using motor and pestle. Ground pellets were then resuspended in lysis buffer (8 ml of lysis buffer contained 0.1M PMSF – 320 ul, Complete Mini – EDTA-free, Proteaste Inhibitor tabs – 16, HALT – 400 ul, 1000x LPC – 8ul ,10mg/ml Aprotinin – 8 ul, 20 uM E-64 – 16 ul, 5mM Benzamidine – 40 ul, 1M NaF – 8 ul, Phostop Tab – 4, 1M, DTT – 16 ul, RNaseOUT – 160 ul, and added to 990 ul dH2O). Lysis was performed by sonication at 30% Amplitude for cycles of 15 sec on 45 seconds for 3 min. This program was run 3 times with 2 min rest in between. Samples were then spun down 10 min 13000 x g (rcf). Lysates were then allowed to bind to beads on rotator for 3hr at 4C. 1 Liter of Binding buffer contained HEPES – 11.9, KCl – 22.4, MgCl – 0.1 g, EGTA – 0.4 g, Glycerol – 100 ml, NP40 (Ipegal) - 0.5 ml, dissolved in 800 ml dH2O, and filled to 1L with dH2O and filter sterilized. Lysates with beads were placed on magnetic rack and supernatant was removed. Beads were washed 2x quickly in 1ml binding buffer and then once for 10 min. After this beads were washed in 500 mM KCl and eluted using 8M Ureas incubation for 1 hr at RT. All samples were snap frozen and stored at -80C.

RNA mediated Interference (RNAi) - RNAi knock-down experiments were performed by feeding on HT115 bacteria (Timmons and Fire 1998). Feeding constructs were obtained from the Ahringer or Openbiosystems libraries and transformed into HT115 bacteria. pL4440 was used as a negative control empty feeding vector. Bacteria were grown at 37°C in LB + ampicillin (100 µg/mL) for 5 hours, induced with 5 mM IPTG for 45 minutes, plated on NNGM (nematode nutritional growth media) + ampicillin (100 µg/mL) + IPTG (1 mM), and grown overnight at room temperature. Embryos isolated by bleaching from gravid hermaphrodites were added to the RNAi plates and transferred to fresh plates as L4 larvae before examination of their progeny. All RNAi experiments were performed at 20^{o}C.

A.5 Figures

Figure 1 – Results of PAR-1 CT CO-IP and secondary RNAi screen

A. Schematic of *C. elegans* PAR-1 Ser/Thr Kinase.

B. Venn diagrams displaying the intersections of mass spec data sets. Replicate names are shown with the number of proteins identified in their IP experiments. The number of proteins identified in all three replicates are shown in black for GFP alone IPs and PAR-1 CT IPs in the center of their respective Venn diagrams. The number of proteins identified in two or more c-terminal IPs and no more than one GFP IP are shown in the bottom Venn diagram.

C. Examples from PAR-1 CT-IP secondary RNA screen. Fluorescent images showing PAR-1 (CT)::GFP and PGL-1::GFP phenotypes for three results from the secondary RNAi screen – *ccf-1* (top), *spd-5* (middle), and *rpn-7* (bottom). Cell stage matched images showing wild-type localization are shown to the left of RNAi embryos.

D. PAR-1 localization phenotypes of SPD-5 interactor RNAi. (left to right) GFP:PAR-1 C-terminus (aa 965-1192) localizes to the centrosomes during mitosis in a wild type single cell *C.elegans* zygote . This localization is ablated in *spd-5* rnai background. AIR-1 and Gamma Tubulin, which are both localized to the centrosome by SPD-5 are also necessary for wild type PAR-1 localization.

Table 1 – PAR-1 (CT) IP interactors and secondary RNAi screen results

Table showing (left to right) sequence ID, gene name, number of positive PAR-1 (CT) CO-IP replicates, number of positive GFP alone CO-IP replicates, description of PAR-1 (CT)::GFP localization phenotypes upon RNAi of identified gene, PGL-1::GFP localization phenotypes upon RNAi, observation of supression of par-1 ts mutant embryonic lethal phenotype.

A

C. elegans
PAR-1(aa1192)

B

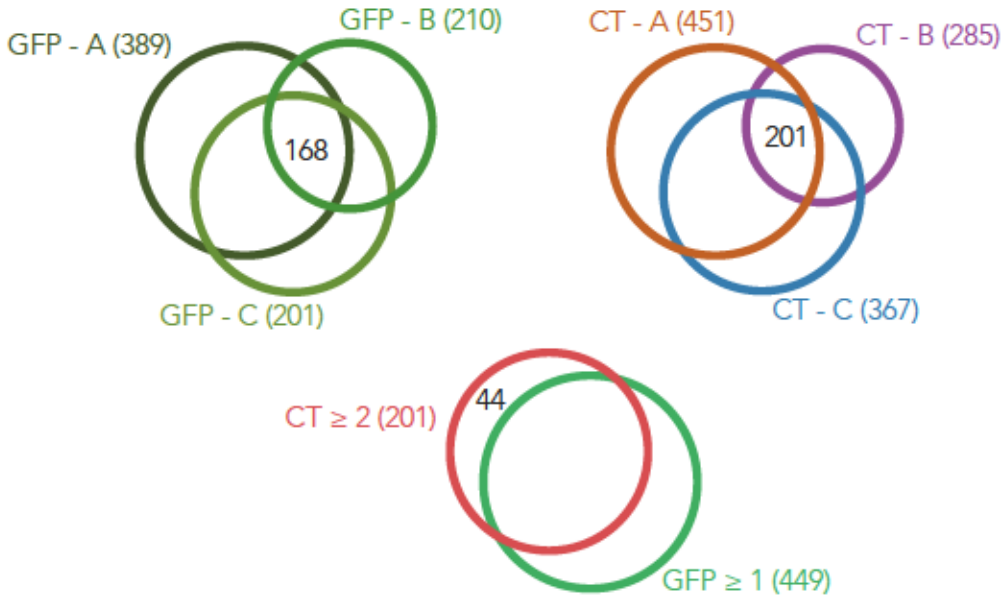

C

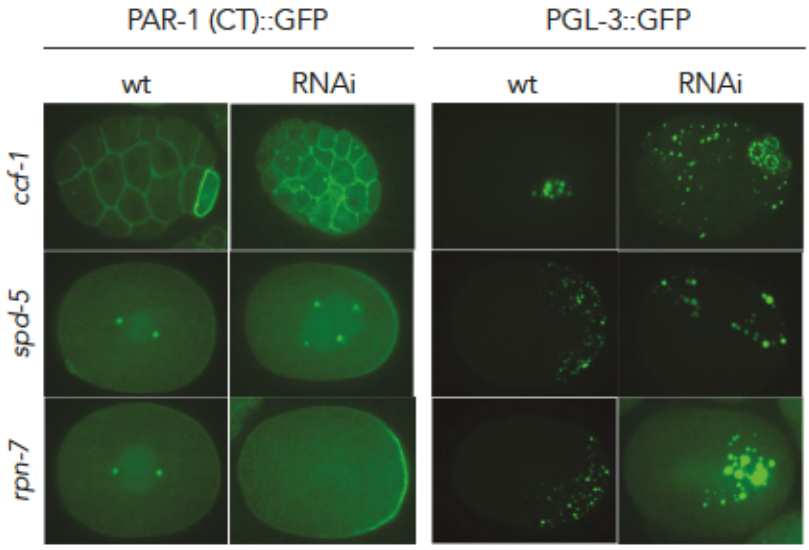

D

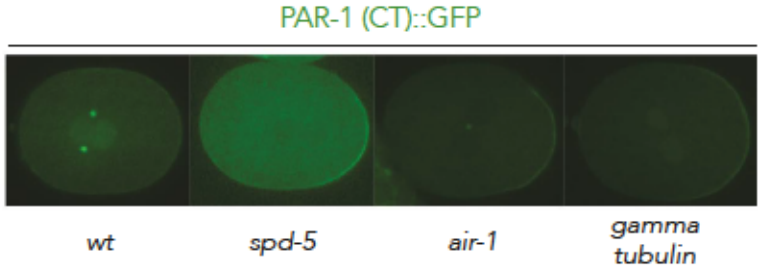

Figure 1

CO-IP Mass Spec / RNAi Screen Results							
	Sequence ID	Gene Name	CT IP	GFP IP	PAR-1 Phenotype	PGL-1 Phenotype	TS Supression
1	F56C9.1	Serine/threonine-protein phosphatase PP1-beta OS=Caenorhabditis elegans GN=gsp-2 PE=2 SV=1	3	1	Slight lower singal from centrosomes 1/10	wt	0
2	Y56A3A.20	CCR4-NOT transcription complex subunit 7 OS=Caenorhabditis elegans GN=ccf-1 PE=2 SV=1	2	0	plieotropic; gross cell defects; no cytoplasmic par-1?; irregular cell division 10/10	mislocalized pgranules in 4 cell, 8 cell, late stage	0
3	F20B6.2	Probable V-type proton ATPase subunit B OS=Caenorhabditis elegans GN=vha-12 PE=1 SV=1	3	1			
4	F43G9.1	Probable isocitrate dehydrogenase [NAD] subunit alpha, mitochondrial OS=Caenorhabditis elegans GN=F43G9.1 PE=1 SV=3	3	1	Increased embryonic nuclear localization (minor) 5/10;	wt	No eggs laid
5	LLC1.3	Dihydrolipoyl dehydrogenase, mitochondrial OS=Caenorhabditis elegans GN=dld-1 PE=2 SV=2	3	1			
6	Y18D10A.5	Glycogen synthase kinase-3 OS=Caenorhabditis elegans GN=gsk-3 PE=1 SV=1	2	0			
7	F49C12.8	26S proteasome non-ATPase regulatory subunit 6 OS=Caenorhabditis elegans GN=rpn-7 PE=3 SV=1	3	1	Random cortical localization in late stages; irregular cell divisions; reduced oocyte nuclear localization 10/10	mislocalized pgranules in 2 cell; multiple Z2/Z3 like cells(up to 6) 10/10	0
8	R06F6.1	Histone RNA hairpin-binding protein OS=Caenorhabditis elegans GN=cdl-1 PE=2 SV=1	2	0	wt	wt	0
9	W01A8.1	Protein MDT-28, isoform a [Caenorhabditis elegans]	2	0	wt	wt	5
10	R03A10.4	Protein NKAT-3, isoform a [Caenorhabditis elegans]	2	0			
11	F10C1.2	Intermediate filament protein ifb-1 OS=Caenorhabditis elegans GN=ifb-1 PE=1 SV=1	3	0	wt	wt	0
12	DY3.2	Protein LMN-1 [Caenorhabditis elegans]	2	0	wt	wt	0
13	F28H1.3	Alanine--tRNA ligase, cytoplasmic OS=Caenorhabditis elegans GN=aars-2 PE=2 SV=1	3	1			
14	K10B3.8	Glyceraldehyde-3-phosphate dehydrogenase 2 OS=Caenorhabditis elegans GN=gpd-2 PE=3 SV=2	2	0	wt	wt	1
15	Y92C3B.2	Splicing factor U2AF 65 kDa subunit OS=Caenorhabditis elegans GN=uaf-1 PE=2 SV=2	3	1	wt	wt	no eggs laid
16	F52E10.5	Intermediate filament protein ifa-3 OS=Caenorhabditis elegans GN=ifa-3 PE=1 SV=1	2	0	wt	wt	0
17	K11D9.2	Protein SCA-1, isoform a [Caenorhabditis elegans]	3	1			0
18	T23G5.1	Ribonucleoside-diphosphate reductase large subunit OS=Caenorhabditis elegans GN=rnr-1 PE=3 SV=1	3	1	100% Emb Lethality; irregular cell divisions; no distinguishable P4 or Z2/Z3	symmetric cleavage	no eggs laid

19	F56A3.4	Spindle-defective protein 5 OS=Caenorhabditis elegans GN=spd-5 PE=1 SV=2	3	1	No Centrosomal PAR-1; No distinguishable P4 or Z2/Z3	no apparent Z2/Z3; mislocalized pgranules in late stages 2/10	
20	M28.5	NHP2-like protein 1 homolog OS=Caenorhabditis elegans GN=M28.5 PE=3 SV=1	2	0			
21	EEED8.1	Maternal effect lethal protein 47 OS=Caenorhabditis elegans GN=mel-47 PE=2 SV=2	2	0	wt	wt	0
22	C05D11.3	Thioredoxin domain-containing protein 9 homolog OS=Caenorhabditis elegans GN=tag-170 PE=4 SV=1	2	0	irregular divisions; no clear Z2/Z3	wt	0
23	D2030.4	NADH dehydrogenase [ubiquinone] 1 beta subcomplex subunit 7 OS=Caenorhabditis elegans GN=D2030.4 PE=3 SV=1	2	0			
24	Y17G7B.5	Protein MCM-6, isoform a [Caenorhabditis elegans]	3	1			
25	F59A2.1	Protein NPP-9, isoform a [Caenorhabditis elegans]	3	1	irregular divisions; no clear Z2/Z3; reduced oocyte nuclear PAR-1	No pgranules in most cells; P cell signal most diffuse cytoplasmic;pgran components seem dissembled in pcells 10/10	0
26	Y17G7B.5 (re	Protein MCM-6, isoform a [Caenorhabditis elegans]	3	1		wt	
27	T22B11.5	Protein OGDH-1 [Caenorhabditis elegans]	3	1	wt	wt	0
28	R06C7.8	Protein BUB-1 [Caenorhabditis elegans]	3	1			
29	R11E3.8	hypothetical protein R11E3.8 - Caenorhabditis elegans	3	1			
30	Y49E10.22	hypothetical protein Y49E10.22 - Caenorhabditis elegans	3	1			
31	F56D2.6	Putative pre-mRNA-splicing factor ATP-dependent RNA helicase F56D2.6 OS=Caenorhabditis elegans GN=F56D2.6 PE=2 SV=1	2	0			
32	F37C12.7	Protein ACS-4 [Caenorhabditis elegans]	3	1		wt	0
33	F22D6.3	Asparagine--tRNA ligase, cytoplasmic OS=Caenorhabditis elegans GN=nrs-1 PE=3 SV=1	3	1			
34	R11A5.4	Protein PCK-2, isoform a [Caenorhabditis elegans]	3	1	wt	wt	0
35	R53.4	Putative ATP synthase subunit f, mitochondrial OS=Caenorhabditis elegans GN=R53.4 PE=3 SV=1	3	1		wt	0
36	Y87G2A.5	Valine--tRNA ligase OS=Caenorhabditis elegans GN=vrs-2 PE=1 SV=1	3	1			
37	Y71F9AL.17	Protein Y71F9AL.17 [Caenorhabditis elegans]	3	1		wt	0
38	W02B12.2	Probable splicing factor, arginine/serine-rich 2 OS=Caenorhabditis elegans GN=rsp-2 PE=3 SV=1	3	1	wt	wt	0
39	F43E2.7	Protein MTCH-1, isoform a [Caenorhabditis elegans]	3	1	wt	wt	0
40	T02G5.9	Lysine--tRNA ligase OS=Caenorhabditis elegans GN=krs-1 PE=2 SV=1	3	1	wt	wt	0

41	F43G6.9	Protein PAT1 homolog 1 OS=Caenorhabditis elegans GN=patr-1 PE=3 SV=2	2	0			
42	T27E9.7	Protein ABCF-2 [Caenorhabditis elegans]	3	1			
43	Y71G10AL.1	Protein Y71G10AL.1, isoform a [Caenorhabditis elegans]	3	1	wt	wt	2
44	F38E11.5	Probable coatomer subunit beta' OS=Caenorhabditis elegans GN=F38E11.5 PE=3 SV=3	3	1	irregular cell division 10/10		0
45	C53A5.1	Protein RIL-1 [Caenorhabditis elegans]	3	1	wt	wt	0
46	T06E4.11	pqn-63 (Mistake - Was supposed to pull Sequence ID T06E4.1 -HCP-2)	N/A	N/A	wt	wt	0
47	W03F9.1	Zinc finger protein ZPR1 homolog OS=Caenorhabditis elegans GN=W03F9.1 PE=3 SV=2	2	0	wt	wt	0
48	T10B5.5	Protein CCT-7, isoform a [Caenorhabditis elegans]	2	0	? (not sure) PAR-1 on ER?	diffuse cytoplasmic signal in addition to normal pgranules 4/10	0
49	D1005.1	Probable ATP-citrate synthase OS=Caenorhabditis elegans GN=D1005.1 PE=2 SV=1	3	1	wt	wt	0
50	F46A9.5	SKR-1 [Caenorhabditis elegans]	2	1			
51	Y56A3A.20 (r	CCR4-NOT transcription complex subunit 7 OS=Caenorhabditis elegans GN=ccf-1 PE=2 SV=1	2	0		perinuclear in 4 cell, 1 cell; mislocalized to cells near p-cell 9/10	
52	VW02B12L.3	Protein EBP-2 [Caenorhabditis elegans]	2	0		wt	1
53	W09C5.2	Protein UNC-59 [Caenorhabditis elegans]	2	0			
54	R07E5.3	Protein SNFC-5 [Caenorhabditis elegans]	2	0		pgranules in multiple cells; diffuse signal 2/10	0
55	Y37D8A.14	Protein CCO-2 [Caenorhabditis elegans]	2	0		wt	1
56	F22F1.1	Protein HIL-3 [Caenorhabditis elegans]	3	1		weak diffuse nuclear signal 2/10	3
57	R10D12.14	Protein SAO-1, isoform a [Caenorhabditis elegans]	2	0		wt	0
58	Y23H5A.3	Protein Y23H5A.3 [Caenorhabditis elegans]	2	0		wt	0
59	T21B10.7	Protein CCT-2 [Caenorhabditis elegans]	2	0		no pgranules 3/10	0
60	Y110A7A.4	thymidylate synthase [Caenorhabditis elegans]	2	0		wt	0
61	F52E10.5	Protein IFA-3 [Caenorhabditis elegans]	2	0		wt	0
62	C28D4.3	Protein GLN-6 [Caenorhabditis elegans]	2	0		wt	0
63	F22B3.4	Protein F22B3.4 [Caenorhabditis elegans]	2	0		mislocalized pgranules at all stages 10/10	0
64	M28.5 (repea	NHP2-like protein 1 homolog OS=Caenorhabditis elegans GN=M28.5 PE=3 SV=1	2	0	Not Screened in PAR-1 yet	wt	1
65	F59B8.2	Protein IDH-1, isoform a [Caenorhabditis elegans]	2	0			
66	Y53G8AR.9	Protein Y53G8AR.9 [Caenorhabditis elegans]	2	0		no apparent p-cell 2/10	2
67	D2045.6	Protein CUL-1 [Caenorhabditis elegans]	2	0		wt	0

68	T28D6.6	Protein T28D6.6, isoform a [Caenorhabditis elegans]	2	0			
69	F46B6.7	Protein ZTF-7 [Caenorhabditis elegans]	2	0			
70	ZK637.5	Protein ASNA-1 [Caenorhabditis elegans]	2	0			
71	Y56A3A.17	Protein NPP-16, isoform b [Caenorhabditis elegans]	2	0		wt	0
72	ZK1320.9	Protein ZK1320.9 [Caenorhabditis elegans]	2	0		wt	0
73	F43G6.9 (rep	Protein PATR-1 [Caenorhabditis elegans]	2	0		wt	0
74	Y105C5B.28	Protein GLN-3, isoform a [Caenorhabditis elegans]	2	0		wt	0
75	Y116A8A.9	Protein MAP-2, isoform a [Caenorhabditis elegans]	2	0			
76	F12F6.6	Protein SEC-24.1 [Caenorhabditis elegans]	2	0			
77	Y38H6C.1	Protein DCT-16, isoform a [Caenorhabditis elegans]	2	0		wt	1
78	T27C4.4	Protein LIN-40, isoform a [Caenorhabditis elegans]	2	0			
79	W06H3.1	Protein IMMT-2 [Caenorhabditis elegans]	2	0		wt	3
80	F52B10.1	Protein NMY-1 [Caenorhabditis elegans]	2	0		wt	1
	T06E4.1	Protein HCP-2 [Caenorhabditis elegans]	3	0			
	Arhinger Library						
A1	C26C6.2	Guanine nucleotide-binding protein G(o) subunit alpha OS=Caenorhabditis elegans GN=goa-1 PE=1 SV=3	2	0	wt	wt	0
A2	F32H2.5	Protein FASN-1 [Caenorhabditis elegans]	3	1	wt		
A3	F08D12.1	Signal recognition particle subunit SRP72 OS=Caenorhabditis elegans GN=F08D12.1 PE=3 SV=2	2	0	wt		0
A4	EEED8.9	Serine/threonine-protein kinase pink-1, mitochondrial OS=Caenorhabditis elegans GN=pink-1 PE=3 SV=2	2	0	wt	wt	0
A5	C44B7.1	hypothetical protein C44B7.10 - Caenorhabditis elegans	2	0			
A6	F32A5.7	Protein LSM-4 [Caenorhabditis elegans]	2	0	wt	wt	0
A7	F13B10.2	Protein RPL-3, isoform a [Caenorhabditis elegans]	3	1	wt		
A8	C50C3.6	Protein PRP-8 [Caenorhabditis elegans]	3	1	wt	p granule gone from oocytes 4/10	0
A9	C50C3.6 (Rep	Protein PRP-8 [Caenorhabditis elegans]	3	1			
A10	C27D11.1	Protein EGL-45 [Caenorhabditis elegans]	3	1	wt	wt	
A11	C02F5.3	Uncharacterized GTP-binding protein C02F5.3 OS=Caenorhabditis elegans GN=C02F5.3 PE=3 SV=2	2	0	wt	wt	0
A12	H34C03.2	Protein H34C03.2 [Caenorhabditis elegans]	3	1			
A13	Y41E3.4	Probable glutamine--tRNA ligase OS=Caenorhabditis elegans GN=ers-1 PE=2 SV=1	3	1	wt	wt	
A14	ZK742.1	Protein XPO-1, isoform a [Caenorhabditis elegans]	3	1	Increased Nuclear Localization in somatic cells; nuclear localization maintained in mature oocytes	diffuse cytoplasmic in later stages; no apparent pcell 5/10	0
A15	K07C5.1	Protein ARX-2 [Caenorhabditis elegans]	2	0			

A16	T14G11.3	Protein IMMT-1 [Caenorhabditis elegans]	2	0		wt	5
A17	F28B3.7	chromosome segregation protein smc1 F28B3.7 [similarity] - Caenorhabditis elegans	2	0		wt	0
A18	T23H2.1	Protein NPP-12 [Caenorhabditis elegans]	2	0			
A19	F25D7.4	Protein F25D7.4 [Caenorhabditis elegans]	2	0		wt	0
A20	F59G1.3	hypothetical protein F59G1.3 - Caenorhabditis elegans	2	0		wt	0
A21	D2085.1	Protein PYR-1 [Caenorhabditis elegans]	2	0		wt	0
A22	F23H11.3	Protein SUCL-2 [Caenorhabditis elegans]	2	0			1
A23	ZK418.9	Protein ZK418.9, isoform a [Caenorhabditis elegans]	2	0		wt	16
A24	T12D8.6	Protein MLC-5 [Caenorhabditis elegans]	2	0			
A25	Y116A8C.35	Protein UAF-2 [Caenorhabditis elegans]	2	0			
A26	K07C5.1 (rep	Protein ARX-2 [Caenorhabditis elegans]	2	0			

Chapter B

Effects of Premature Stop on MEX-5 S404A Expression

B.1 Summary

In attempting to mutate the S404 residue of the RNA binding protein MEX-5 mentioned in Chapter 1, we found that, due to an incomplete/aberrant editing event, one of the worms edited received a frameshift mutation resulting in a premature stop. We went on to find that this additional mutation resulted in a cold-sensitive strain that expressed reduced levels of the MEX-5 protein. We also found that this strain was sensitive to loss of the non-essential homologue *mex-6* and that, at non-permissive temperatures (15°C), increased its expression of this mutant MEX-5 protein.

B.2 Results

We designed CRISPR guide RNAs to mutate the MEX-5 RNA binding protein at its S404 residue. Our goal was to mutate this residue to an alanine to ablate phosphorylation by the serine/threonine kinase PAR-1 (Figure 1A). To do this, we targeted the endogenous locus coding for *mex-5* using two overlapping sgRNAs (Figure 1B, Figure 1C). We also included a repair template that coded for the s404a mutation and mutated the sgRNA sites with silent mutations that also introduced a restriction site for the PstI restriction enzyme. After identifying edited worms by PCR followed by restriction digest, we recognized that one strain obtained in the experiment showed insertion of the restriction site but did not exhibit the high percent sterility of the other strains identified. We sequenced this strain and found that there had been a missense mutation resulting in a frameshift 11 nucleotides downstream of the *s404a* mutation. This frameshift resulted in a region of 27 amino

acids being recoded and terminated in a premature stop codon that truncated the full-length protein by 34 amino acids (Figure 1D).

Because these worms were viable at room temperature, we were able to check the localization and expression of OLLAS tagged MEX-5. We found that in these worms, MEX-5 expression was drastically reduced until the worms were shifted to 15°C. These cold sensitive worms also showed very high levels of maternal effect embryonic sterility at this non-permissive temperature. By performing PCR and restriction digest on singled out worms we were able to identify that this MES phenotype was inherited semi-dominantly (Figure 2A, Figure 2B).

To validate that this mutation did in fact result in a truncation and decrease in protein expression we performed a western blot to OLLAS::MEX-5 in wild-type and our *s404a*□□*frameshift* mutant at permissive and non-permissive temperatures. This confirmed our earlier expectation that MEX-5 was truncated in the mutant resulting in a lower migrating band on the SDS gel and that decreasing the temperature caused an increase in mutant protein expression not seen in wild-type emrbyos (Figure 2C). Lastly, we also saw that this mutant, at permissive temperatures, was sensitive to *mex-6* RNAi – a non-essential homologue of *mex-5* in wild-type worms (Figure 2D).

B.3 Discussion

We earlier hypothesized that sterility in *mex-5(s404a)* mutants is caused by the gain of function to MEX-5 protein. PAR-1 is no longer able to phosphorylate its primary site on MEX-5 and as a result we see that MEX-5 is symmetric across the cytoplasm in the early embryo (Figure 2A). We hypothesize that this causes a depletion of critical germline determinants that MEX-5 is known to be responsible for turning over in the anterior cytoplasm in wild-type embryos. In our *s404a(+1)* *frameshift* mutant, we see a similar phenotype at non-permissive temperatures indicating that this MEX-5 is functional. Interestingly, it is likely that this MEX-5 is an even greater increase in function as it is now also missing its S458 PAR-1 phosphorylation site (Figure 1D).

Although we do not know the reason for the increase in MEX-5 expression at low temperatures, it is possible that the frameshift mutation and premature stop caused by this mis-editing event make the mutant MEX-5 a substrate for nonsense mediated decay (NMD) and that this pathway is inhibited at low temperatures resulting in a partial rescue from that degradation. Regardless of the means of repression of MEX-5 expression, we believe that the decreased levels of MEX-5 make it tolerable and prevent the sterility seen in the clean *mex-5(s404a)* mutant. It would be interesting to determine whether introducing a premature stop is sufficient to lower the expression of any protein in *C. elegans* and whether the cold-sensitivity would allow for the creation of many mutants with tunable protein expression.

B.4 Experimental Procedures

Western Blots - Western blots were performed by running worm lysates on 7% Tris Acetate SDS PAGE precast gels (Bio-Rad). Protein was transferred to nitrocellulose membrane which was pre-blocked in 5% Milk diluted in PBS-Tween (0.1%) for 5 minutes (3 times). Membrane was then incubated with Primary antibody for at least 18 hours at 4° C or 2 hours at room temperature. Membranes were washed and blocked in 5% milk for 5 minutes (3 times) and incubated with secondary HRP conjugated antibody for 45 minutes at room temperature. Membranes were washed in 5% milk for 5 minutes (2 times) and PBST for 5 minutes (1 time). Membranes were then exposed to ECL substrate for 1 minute and then exposed to film. Primary antibody dilutions (in 5% Milk PBST): Rat α OLLAS-L2 (1:1000, Novus Biological), Mouse α Tubulin (1:1000, Sigma).

Immunostaining - Adult worms were placed into M9 salt solution on epoxy autoclavable slides (thermo-fisher) and squashed with a coverslip to extrude embryos. Slides were frozen by laying on pre-chilled aluminum blocks for 20 minutes (chilled using dry ice). Embryos were permeabilized by freeze-cracking (removal of coverslips from slides) followed by incubation in methanol at -20°C for >15 minutes, and in acetone (pre-chilled at -20^{o}C) at room temperature for 10 minutes. Slides were blocked in PBS-Tween (0.1%) BSA (0.5%) for 15 minutes x 2, and incubated with 50 ul primary antibody overnight at 4°C in a humid chamber. Antibody dilutions (in PBST/BSA): K76 (1:10, DSHB, RRID:AB_531836), Rat α OLLAS-L2 (1:200, Novus Biological, RRID: AB_1625980). Secondary antibodies were applied for 2 hours at room temperature.

Confocal Microscopy - Fluorescence microscopy was performed using a Zeiss Axio Imager with a Yokogawa spinning-disc confocal scanner. Images were taken and

stored using Slidebook v 6.0 software (Intelligent Imaging Innovations) using a 63x objective. For live imaging, embryos were dissected from adult hermaphrodites in M9 salt solution and mounted onto 3% agarose pads. All embryo images are z stack maximum projections using a z step size of 1 μm, spanning the entire width of the embryo.

RNA mediated Interference (RNAi) - RNAi knock-down experiments were performed by feeding on HT115 bacteria (Timmons and Fire 1998). Feeding constructs were obtained from the Ahringer or Openbiosystems libraries and transformed into HT115 bacteria. pL4440 was used as a negative control empty feeding vector. Bacteria were grown at 37°C in LB + ampicillin (100 μg/mL) for 5 hours, induced with 5 mM IPTG for 45 minutes, plated on NNGM (nematode nutritional growth media) + ampicillin (100 μg/mL) + IPTG (1 mM), and grown overnight at room temperature. Embryos isolated by bleaching from gravid hermaphrodites were added to the RNAi plates and transferred to fresh plates as L4 larvae before examination of their progeny. All RNAi experiments were performed at 20^{o}C.

B.5 Figures

Figure 1 – Design of MEX-5 S404A editing

A. Schematic of *C. elegans* MEX-5 protein.

B. Schematic of *C. elegans mex-5* coding sequence.

C. Schematic of *C. elegans mex-5* editing region. Intronic sequences are denoted by lower case type. Exons are denoted by upper case type. Mutations are shown as lower case bold type. Guide RNA targeting sequences are outlined in green and red (for guide RNA 1 and 2 respectively). The codon coding for S404 is highlighted in purple. Silent mutations made to guide RNA regions to crease PstI restriction site are shown. Unedited genomic DNA sequence is shown on top and expected edited sequence is shown on bottom.

D. Schematic of *C. elegans* edited MEX-5 S404A + Frameshift amino acid sequence. Amino acid sequence for edited region is shown starting at S404A (purple type). Green region identifies 27 missense amino acids following the frameshift ending n premature stop. Red region identifies 34 amino acids deleted in frameshift mutant relative to wild-type. Wild-type amino acid sequence is shown on top. Mutant amino acid sequence is shown on bottom.

Figure 2 – Design of MEX-5 S404A editing

A. Fluorescent images of OLLAS::MEX-5 and PGL-1 staining in S404A + Frameshift background. Images are shown of embryos stained with anti-OLLAS antibody (left) and K76 anti-PGL-1 antibody (right). Images are shown for (top) wild-type background at permissive temperatures, (middle) *s404a frameshift* mutant at permissive temperature, and (bottom) *s404a + frameshift* mutant at non-permissive temperature (15°C). Blue shows DAPI staining.

B. Restriction Digest and sterility of single *s404a + frameshift* mutants. Each well shows the result of a single worm PCR of s404a mutants followed by restriction digest using the PstI restriction enzyme. Upper band indicates wild-type genotype while lower two bands indicate mutant genotype. Lanes are numbered corresponding to graph below. Graph shows percent sterility coming from the broods of the hermaphrodites PCRed in upper gel. N values reflect total number of brood counted.

C. Western blot comparing expression of *s404a + frameshift* mutant to wild-type at permissive and non permissive temperatures. Labeling on top of gel shows genotype and temperature of worms from which embryos were harvested. 0.1x refers to a 10x dilution lane. Upper band in each lane showed anti-OLLAS staining while lower band indicates anti tubulin staining. In graph below, the signal for each anti OLLAS band was quantified and measured relative to the singal from the corresponding tubulin band to normalize for total protein loaded. Quantification was performed using 0.1x lanes only.

D. Graph showing sensitivity to *mex-6* RNAi. Graphs shows percent embryonic lethality calculated from n > 100 embryos each using N2 wild-type worms (green) and the *s404a + frameshift* mutant (red).

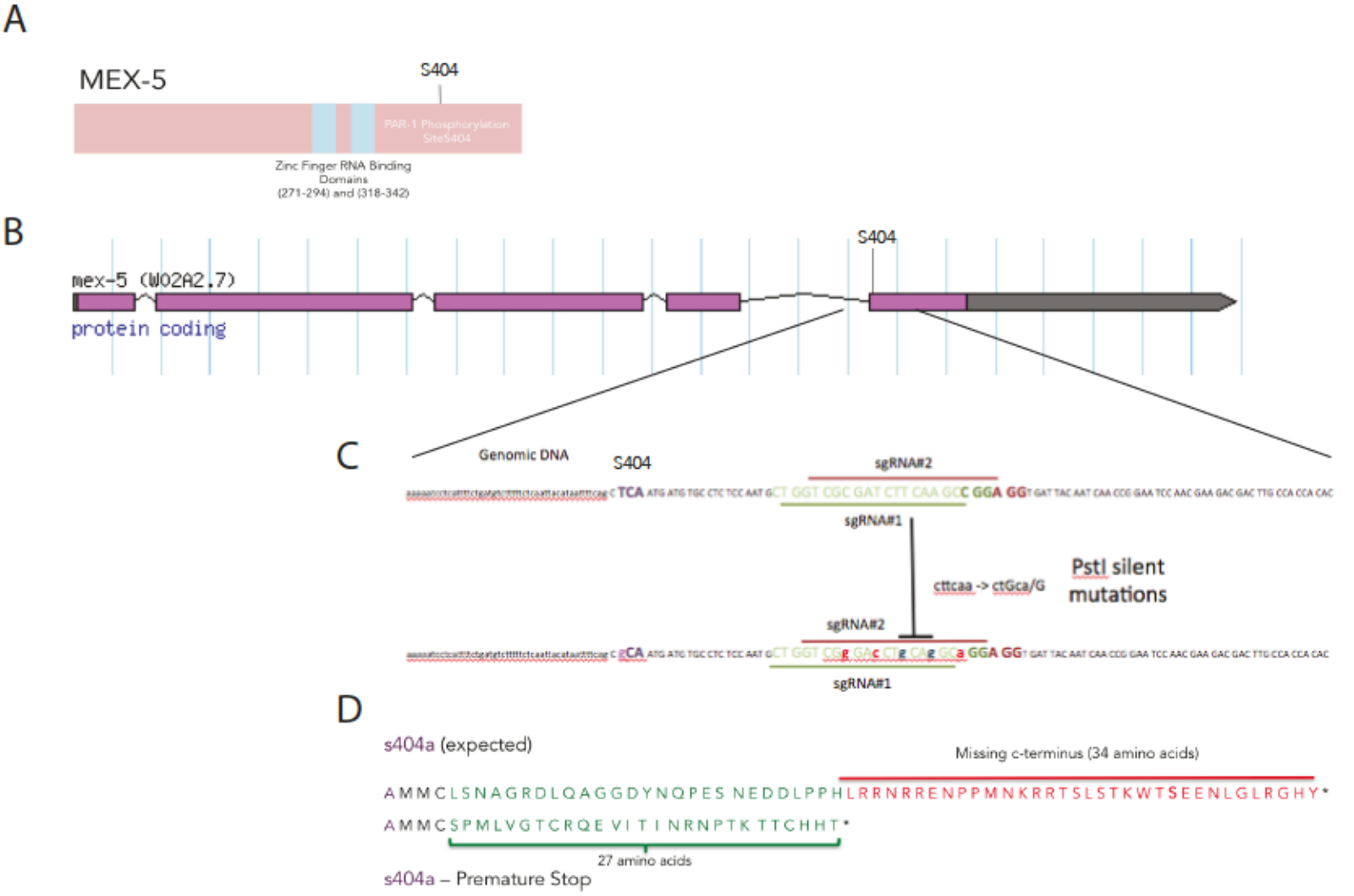
A
MEX-5
S404
PAR-1 Phosphorylation Site S404
Zinc Finger RNA Binding Domains (271-294) and (318-342)
B
S404
mex-5 (W02A2.7)
protein coding
C
Genomic DNA
S404
sgRNA#2
sgRNA#1
cttcaa -> ctGca/G
PstI silent mutations
sgRNA#2
sgRNA#1
D
s404a (expected)
Missing c-terminus (34 amino acids)
AMMCLSNAGRDLQAGGDYNQPES NEDDLPPHLRRNRRENPPMNKRRTSLSTKWTSEENLGLRGHY*
AMMCSPMLVGTCRQE VI T I NRNPTK TTCHHT*
27 amino acids
s404a – Premature Stop

Figure 1

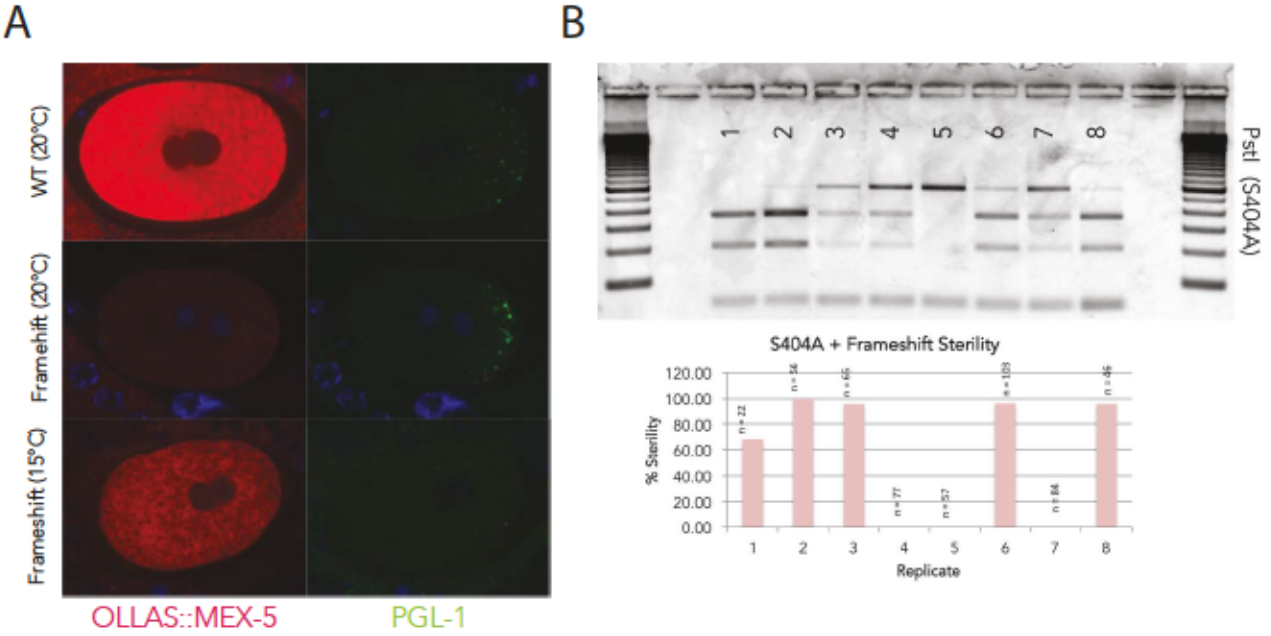
A
WT (20°C)
Frameshift (20°C)
Frameshift (15°C)
OLLAS::MEX-5
PGL-1
B
1
2
3
4
5
6
7
8
PstI (S404A)
S404A + Frameshift Sterility
% Sterility
Replicate
C
N2
OLLAS::MEX-5/N2 (20°C)
OLLAS::MEX-5/N2 (20°C) 0.1x
OLLAS::MEX-5 (20°C)
OLLAS::MEX-5 (20°C) 0.1x
OLLAS::MEX-5 (15°C)
OLLAS::MEX-5 (15°C)
Frameshift (20°C)
Frameshift (20°C) 0.1x
Frameshift (15°C)
Frameshift (15°C) 0.1x
75 kD -
50 kD -
37kD-
OLLAS:Tubulin Ratio 0.1x
OLLAS:Tubulin Ratio
N2 1x
JH3190 (20C)/N2 0.1x
JH3190 (20C)0.1x
JH3190 (15C) 0.1x
FrameShift (20C) 0.1x
FrameShift (15C) 0.1x
D
% Embryonic Lethality
N2
Premature Stop s404a
pL440
mex-6
RNAi Treatment

Figure 2

References

Alberti, S., D. Mateju, L. Mediani and S. Carra (2017). "Granulostasis: Protein Quality Control of RNP Granules." Front Mol Neurosci **10**: 84.

Anderson, P. and N. Kedersha (2002). "Stressful initiations." J Cell Sci **115**(Pt 16): 3227-3234.

Anderson, P. and N. Kedersha (2006). "RNA granules." J Cell Biol **172**(6): 803-808.

Banani, S. F., A. M. Rice, W. B. Peeples, Y. Lin, S. Jain, R. Parker and M. K. Rosen (2016). "Compositional Control of Phase-Separated Cellular Bodies." Cell **166**(3): 651-663.

Basu, S. and R. P. Bahadur (2016). "A structural perspective of RNA recognition by intrinsically disordered proteins." Cell Mol Life Sci.

Brangwynne, C. P., C. R. Eckmann, D. S. Courson, A. Rybarska, C. Hoege, J. Gharakhani, F. Julicher and A. A. Hyman (2009). "Germline P granules are liquid droplets that localize by controlled dissolution/condensation." Science **324**(5935): 1729-1732.

Brangwynne, C. P., T. J. Mitchison and A. A. Hyman (2011). "Active liquid-like behavior of nucleoli determines their size and shape in Xenopus laevis oocytes." Proc Natl Acad Sci U S A **108**(11): 4334-4339.

Brenner, S. (1974). "The genetics of Caenorhabditis elegans." Genetics **77**(1): 71-94.

Buchan, J. R. and R. Parker (2009). "Eukaryotic stress granules: the ins and outs of translation." Mol Cell **36**(6): 932-941.

Buchan, J. R., J. H. Yoon and R. Parker (2011). "Stress-specific composition, assembly and kinetics of stress granules in Saccharomyces cerevisiae." J Cell Sci **124**(Pt 2): 228-239.

Castello, A., B. Fischer, C. K. Frese, R. Horos, A. M. Alleaume, S. Foehr, T. Curk, J. Krijgsveld and M. W. Hentze (2016). "Comprehensive Identification of RNA-Binding Domains in Human Cells." Mol Cell **63**(4): 696-710.

Courchaine, E. M., A. Lu and K. M. Neugebauer (2016). "Droplet organelles?" EMBO J **35**(15): 1603-1612.

DeBella, L. R., A. Hayashi and L. S. Rose (2006). "LET-711, the Caenorhabditis elegans NOT1 ortholog, is required for spindle positioning and regulation of microtubule length in embryos." Mol Biol Cell **17**(11): 4911-4924.

Decker, C. J., D. Teixeira and R. Parker (2007). "Edc3p and a glutamine/asparagine-rich domain of Lsm4p function in processing body assembly in Saccharomyces cerevisiae." J Cell Biol **179**(3): 437-449.

Dosztanyi, Z., V. Csizmok, P. Tompa and I. Simon (2005). "IUPred: web server for the prediction of intrinsically unstructured regions of proteins based on estimated energy content." Bioinformatics **21**(16): 3433-3434.

Dutta, A., S. Zheng, D. Jain, C. E. Cameron and J. C. Reese (2011). "Intermolecular interactions within the abundant DEAD-box protein Dhh1 regulate its activity in vivo." J Biol Chem **286**(31): 27454-27470.

Elbaum-Garfinkle, S., Y. Kim, K. Szczepaniak, C. C. Chen, C. R. Eckmann, S. Myong and C. P. Brangwynne (2015). "The disordered P granule protein LAF-1 drives phase separation into droplets with tunable viscosity and dynamics." Proc Natl Acad Sci U S A **112**(23): 7189-7194.

Gallo, C. M., E. Munro, D. Rasoloson, C. Merritt and G. Seydoux (2008). "Processing bodies and germ granules are distinct RNA granules that interact in *C.elegans* embryos." Dev Biol **323**(1): 76-87.

Gallo, C. M., J. T. Wang, F. Motegi and G. Seydoux (2010). "Cytoplasmic partitioning of P granule components is not required to specify the germline in *C.elegans*." Science **330**(6011): 1685-1689.

Gao, Z., A. A. Putnam, H. A. Bowers, U. P. Guenther, X. Ye, A. Kindsfather, A. K. Hilliker and E. Jankowsky (2016). "Coupling between the DEAD-box RNA helicases Ded1p and eIF4A." Elife **5**.

Griffin, E. E., D. J. Odde and G. Seydoux (2011). "Regulation of the MEX-5 gradient by a spatially segregated kinase/phosphatase cycle." Cell **146**(6): 955-968.

Guo, L. and J. Shorter (2015). "It's Raining Liquids: RNA Tunes Viscoelasticity and Dynamics of Membraneless Organelles." Mol Cell **60**(2): 189-192.

Guo, S. and K. J. Kemphues (1995). "par-1, a gene required for establishing polarity in *C.elegans* embryos, encodes a putative Ser/Thr kinase that is asymmetrically distributed." Cell **81**(4): 611-620.

Han, T. W., M. Kato, S. Xie, L. C. Wu, H. Mirzaei, J. Pei, M. Chen, Y. Xie, J. Allen, G. Xiao and S. L. McKnight (2012). "Cell-free formation of RNA granules: bound RNAs identify features and components of cellular assemblies." Cell **149**(4): 768-779.

Hanazawa, M., M. Yonetani and A. Sugimoto (2011). "PGL proteins self associate and bind RNPs to mediate germ granule assembly in *C.elegans*." J Cell Biol **192**(6): 929-937.

Hannak, E., M. Kirkham, A. A. Hyman and K. Oegema (2001). "Aurora-A kinase is required for centrosome maturation in Caenorhabditis elegans." J Cell Biol **155**(7): 1109-1116.

Hubstenberger, A., C. Cameron, S. L. Noble, S. Keenan and T. C. Evans (2015). "Modifiers of solid RNP granules control normal RNP dynamics and mRNA activity in early development." J Cell Biol **211**(3): 703-716.

Hubstenberger, A., S. L. Noble, C. Cameron and T. C. Evans (2013). "Translation repressors, an RNA helicase, and developmental cues control RNP phase transitions during early development." Dev Cell **27**(2): 161-173.

Hyman, A. A., C. A. Weber and F. Julicher (2014). "Liquid-liquid phase separation in biology." Annu Rev Cell Dev Biol **30**: 39-58.

Jain, S., J. R. Wheeler, R. W. Walters, A. Agrawal, A. Barsic and R. Parker (2016). "ATPase-Modulated Stress Granules Contain a Diverse Proteome and Substructure." Cell **164**(3): 487-498.

Kato, M., T. W. Han, S. Xie, K. Shi, X. Du, L. C. Wu, H. Mirzaei, E. J. Goldsmith, J. Longgood, J. Pei, N. V. Grishin, D. E. Frantz, J. W. Schneider, S. Chen, L. Li, M. R. Sawaya, D. Eisenberg, R. Tycko and S. L. McKnight (2012). "Cell-free formation of RNA granules: low complexity sequence domains form dynamic fibers within hydrogels." Cell **149**(4): 753-767.

Kedersha, N. L., M. Gupta, W. Li, I. Miller and P. Anderson (1999). "RNA-binding proteins TIA-1 and TIAR link the phosphorylation of eIF-2 alpha to the assembly of mammalian stress granules." J Cell Biol **147**(7): 1431-1442.

Knowles, R. B., J. H. Sabry, M. E. Martone, T. J. Deerinck, M. H. Ellisman, G. J. Bassell and K. S. Kosik (1996). "Translocation of RNA granules in living neurons." J Neurosci **16**(24): 7812-7820.

Kroschwald, S., S. Maharana, D. Mateju, L. Malinovska, E. Nuske, I. Poser, D. Richter and S. Alberti (2015). "Promiscuous interactions and protein disaggregases determine the material state of stress-inducible RNP granules." Elife **4**: e06807.

Lee, C. F., C. P. Brangwynne, J. Gharakhani, A. A. Hyman and F. Julicher (2013). "Spatial organization of the cell cytoplasm by position-dependent phase separation." Phys Rev Lett **111**(8): 088101.

Li, P., S. Banjade, H. C. Cheng, S. Kim, B. Chen, L. Guo, M. Llaguno, J. V. Hollingsworth, D. S. King, S. F. Banani, P. S. Russo, Q. X. Jiang, B. T. Nixon and M. K. Rosen (2012). "Phase transitions in the assembly of multivalent signalling proteins." Nature **483**(7389): 336-340.

Lin, Y., D. S. Protter, M. K. Rosen and R. Parker (2015). "Formation and Maturation of Phase-Separated Liquid Droplets by RNA-Binding Proteins." Mol Cell **60**(2): 208-219.

Linder, P. and E. Jankowsky (2011). "From unwinding to clamping - the DEAD box RNA helicase family." Nat Rev Mol Cell Biol **12**(8): 505-516.

Moravcevic, K., J. M. Mendrola, K. R. Schmitz, Y. H. Wang, D. Slochower, P. A. Janmey and M. A. Lemmon (2010). "Kinase associated-1 domains drive MARK/PAR1 kinases to membrane targets by binding acidic phospholipids." Cell **143**(6): 966-977.

Motegi, F. and G. Seydoux (2013). "The PAR network: redundancy and robustness in a symmetry-breaking system." Philos Trans R Soc Lond B Biol Sci **368**(1629): 20130010.

Motegi, F., S. Zonies, Y. Hao, A. A. Cuenca, E. Griffin and G. Seydoux (2011). "Microtubules induce self-organization of polarized PAR domains in Caenorhabditis elegans zygotes." Nat Cell Biol **13**(11): 1361-1367.

Mugler, C. F., M. Hondele, S. Heinrich, R. Sachdev, P. Vallotton, A. Y. Koek, L. Y. Chan and K. Weis (2016). "ATPase activity of the DEAD-box protein Dhh1 controls processing body formation." Elife **5**.

Neves, A., C. Busso and P. Gonczy (2015). "Cellular hallmarks reveal restricted aerobic metabolism at thermal limits." Elife **4**: e04810.

Nishi, Y., E. Rogers, S. M. Robertson and R. Lin (2008). "Polo kinases regulate *C.* *elegans* embryonic polarity via binding to DYRK2-primed MEX-5 and MEX-6." Development **135**(4): 687-697.

Nott, T. J., E. Petsalaki, P. Farber, D. Jervis, E. Fussner, A. Plochowietz, T. D. Craggs, D. P. Bazett-Jones, T. Pawson, J. D. Forman-Kay and A. J. Baldwin (2015). "Phase transition of a disordered nuage protein generates environmentally responsive membraneless organelles." Mol Cell **57**(5): 936-947.

Nousch, M., N. Techritz, D. Hampel, S. Millonigg and C. R. Eckmann (2013). "The Ccr4-Not deadenylase complex constitutes the main poly(A) removal activity in *C.* *elegans*." J Cell Sci **126**(Pt 18): 4274-4285.

Pagano, J. M., C. C. Clingman and S. P. Ryder (2011). "Quantitative approaches to monitor protein-nucleic acid interactions using fluorescent probes." RNA **17**(1): 14-20.

Pagano, J. M., B. M. Farley, L. M. McCoig and S. P. Ryder (2007). "Molecular basis of RNA recognition by the embryonic polarity determinant MEX-5." J Biol Chem **282**(12): 8883-8894.

Paix, A., A. Folkmann, D. Rasoloson and G. Seydoux (2015). "High Efficiency, Homology-Directed Genome Editing in Caenorhabditis elegans Using CRISPR-Cas9 Ribonucleoprotein Complexes." Genetics **201**(1): 47-54.

Patel, A., H. O. Lee, L. Jawerth, S. Maharana, M. Jahnel, M. Y. Hein, S. Stoynov, J. Mahamid, S. Saha, T. M. Franzmann, A. Pozniakovski, I. Poser, N. Maghelli, L. A. Royer, M. Weigert, E. W. Myers, S. Grill, D. Drechsel, A. A. Hyman and S. Alberti (2015). "A Liquid-to-Solid Phase Transition of the ALS Protein FUS Accelerated by Disease Mutation." Cell **162**(5): 1066-1077.

Patel, A., L. Malinovska, S. Saha, J. Wang, S. Alberti, Y. Krishnan and A. A. Hyman (2017). "ATP as a biological hydrotrope." Science **356**(6339): 753-756.

Pitt, J. N., J. A. Schisa and J. R. Priess (2000). "P granules in the germ cells of Caenorhabditis elegans adults are associated with clusters of nuclear pores and contain RNA." Dev Biol **219**(2): 315-333.

Reijns, M. A., R. D. Alexander, M. P. Spiller and J. D. Beggs (2008). "A role for Q/N-rich aggregation-prone regions in P-body localization." J Cell Sci **121**(Pt 15): 2463-2472.

Rice, A. M. and M. K. Rosen (2017). "ATP controls the crowd." Science **356**(6339): 701-702.

Saha, S., Christoph A. Weber, M. Nousch, O. Adame-Arana, C. Hoege, Marco Y. Hein, E. Osborne-Nishimura, J. Mahamid, M. Jahnel, L. Jawerth, A. Pozniakovski, Christian R. Eckmann, F. Jülicher and Anthony A. Hyman (2016). "Polar Positioning of Phase-Separated Liquid Compartments in Cells Regulated by an mRNA Competition Mechanism." Cell.

Schubert, C. M., R. Lin, C. J. de Vries, R. H. Plasterk and J. R. Priess (2000). "MEX-5 and MEX-6 function to establish soma/germline asymmetry in early *C. elegans* embryos." Mol Cell **5**(4): 671-682.

Smith, J., D. Calidas, H. Schmidt, T. Lu, D. Rasoloson and G. Seydoux (2016). "Spatial patterning of P granules by RNA-induced phase separation of the intrinsically-disordered protein MEG-3." Elife **5**.

Strome, S. and W. B. Wood (1983). "Generation of asymmetry and segregation of germ-line granules in early *C. elegans* embryos." Cell **35**(1): 15-25.

Timmons, L. and A. Fire (1998). "Specific interference by ingested dsRNA." Nature **395**(6705): 854.

Updike, D. and S. Strome (2010). "P granule assembly and function in Caenorhabditis elegans germ cells." J Androl **31**(1): 53-60.

Varadi, M., F. Zsolyomi, M. Guharoy and P. Tompa (2015). "Functional Advantages of Conserved Intrinsic Disorder in RNA-Binding Proteins." PLoS One **10**(10): e0139731.

Voronina, E., G. Seydoux, P. Sassone-Corsi and I. Nagamori (2011). "RNA granules in germ cells." Cold Spring Harb Perspect Biol **3**(12).

Wang, J. T., J. Smith, B. C. Chen, H. Schmidt, D. Rasoloson, A. Paix, B. G. Lambrus, D. Calidas, E. Betzig and G. Seydoux (2014). "Regulation of RNA granule dynamics by phosphorylation of serine-rich, intrinsically disordered proteins in *C. elegans*." Elife **3**: e04591.

Weber, S. C. and C. P. Brangwynne (2012). "Getting RNA and protein in phase." Cell **149**(6): 1188-1191.

Wippich, F., B. Bodenmiller, M. G. Trajkovska, S. Wanka, R. Aebersold and L. Pelkmans (2013). "Dual specificity kinase DYRK3 couples stress granule condensation/dissolution to mTORC1 signaling." Cell **152**(4): 791-805.

Wu, Y., H. Zhang and E. E. Griffin (2015). "Coupling between cytoplasmic concentration gradients through local control of protein mobility in the Caenorhabditis elegans zygote." Mol Biol Cell **26**(17): 2963-2970.

Xiang, S., M. Kato, L. C. Wu, Y. Lin, M. Ding, Y. Zhang, Y. Yu and S. L. McKnight (2015). "The LC Domain of hnRNPA2 Adopts Similar Conformations in Hydrogel Polymers, Liquid-like Droplets, and Nuclei." Cell **163**(4): 829-839.

Zhang, H., S. Elbaum-Garfinkle, E. M. Langdon, N. Taylor, P. Occhipinti, A. A. Bridges, C. P. Brangwynne and A. S. Gladfelter (2015). "RNA Controls PolyQ Protein Phase Transitions." Mol Cell **60**(2): 220-230.

CURRICULUM VITAE

Education

Institution and Location	Degree	Start Date	End Date	Field of Study
Georgia Inst. Of Technology	B.S.	08/2008	06/2011	Biology
Johns Hopkins School of Medicine	PhD	08/2011		Biochemistry Cellular and Molecular Biology

Publications

Smith, J., Calidas, D., Schmidt, H., Lu, T., Rasoloson, D., Seydoux, G. (2016). Spatial patterning of P granules by RNA-induced phase separation of the intrinsically-disordered protein MEG-3. *eLife, 5*. doi:10.7554/elife.21337

Wang, J. T., **Smith, J**., Chen, B.-C., Schmidt, H., Rasoloson, D., Paix, A., Seydoux, G. (2014). Regulation of RNA granule dynamics by phosphorylation of serine-rich, intrinsically-disordered proteins in *C. elegans*. eLife 2014;10.7554/eLife.04591

Paix, A., Wang, Y., Smith, H. E., Lee, C.-Y. S., Calidas, D., Lu, T., **Smith, J**., Schmidt, H., Krause, M., Seydoux, G. (2014). Scalable and Versatile Genome Editing Using Linear DNAs with Micro-Homology to Cas9 Sites in Caenorhabditis elegans. *Genetics*, 198, 1347-1356

Positions and Employment

2012 Tutor for Organic Mechanisms in Biology graduate course at JHSOM
2010-2011 Head Teaching Assistant of Introductory and Honors Biology at GIT
2009-2010 Teaching Assistant of Introductory Biology at GIT

Academic and Professional Honors

2017 Inaugural Michael DiMaio, M.D., Research Prize
2017 3-Minute Thesis (3MT) Competition Winner (3rd place and Audience Favorite)
2016 2016 Biotech & Healthcare Case Competition Team Leader
2014 64th Lindau Nobel Laureate Meeting Young Researcher
2014 Molecular Biology Genomics Departmental Journal Club Award
2011 Presidential Honors Award: Highest Graduating GPA in School of Biology
2011 Graduated with Highest Honors – Georgia Inst. Technology
2008 GA Tech Alumni Scholarship
2008 Alpha Phi Alpha Scholarship

Research Presentations

Talk - International RNA Granule Symposium (2017)
Poster - HHMI Scientific Meeting (Janelia Research Campus) (2017)
Talk - American Society for Cell Biology – ASCB (2016)

Poster - American Society for Cell Biology – ASCB (2016)
Poster - Cold Spring Harbor Meeting (2014)
Poster - Annual Biomedical Research Conference for Minority Students (2013)
Poster - *C.elegans* Development, Cell Biology, and Gene Expression Meeting (2012)
Poster - American Aging Association 40th Annual Meeting (2011)